The ΛCDM Effective Field Theory of Large Scale Structure

Theodore Steele

Supervisor: Dr. Tobias Baldauf

Department of Applied Mathematics and Theoretical Physics
University of Cambridge

This dissertation is submitted for the degree of
Doctor of Philosophy

Wolfson College

September 2021

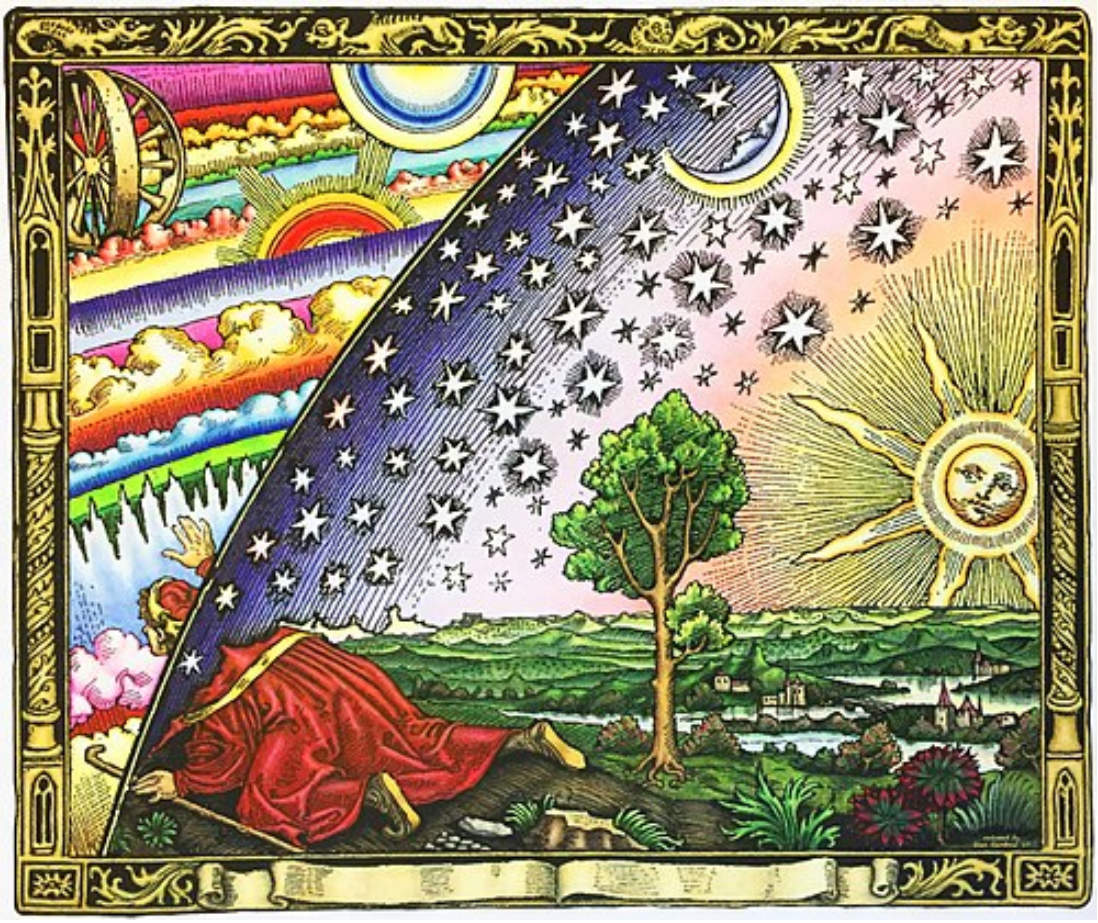

I declare that the work presented in this thesis constitutes original research conducted in the Department of Applied Mathematics and Theoretical Physics at the University of Cambridge and not previously submitted for assessment for any qualification. The research is my own and has previously been published in two research papers, both of which are cited in the text where appropriate. Credit has consistently been given to those responsible for work that was not my own and the original work in the thesis is clearly labelled to separate it from the reviews of the past work of other researchers.

I would like to acknowledge the assistance of Dr Tobias Baldauf, without whose support and supervision this thesis would not have been possible, and the technical assistance of Dr Kacper Kornet, who kept our computational resources working efficiently throughout the project. I would also like to acknowledge the assistance of Dr James Fergusson, who has served as my advisor for the duration of this project and has offered assistance throughout, including frequently reviewing and critiquing this thesis as it was being written.

Image credit: a copy of the Flammarion Engraving (1888) colourised by Houston Physicist in 2017.

THE Large Scale Structure (LSS) of the Universe, that being the large scale distribution of dark and baryonic matter and of the halos and galaxies they form, promises to be a source of unprecedented amounts of information in the near future, with hundreds of millions of galaxies being mapped by various surveys.

Analytic models of LSS begin by treating an ensemble of dark matter particles as a fluid and solving this fluid's equations of motion using a power series in the density field, which is physically interpreted as a perturbative expansion around a linear solution describing idealised, large scale dynamics. Until the past decade, these perturbative methods took the form of what is called Standard Perturbation Theory (SPT) which extends its perturbative description of LSS down to all scales, even beyond those at which the fluid description of dark matter stops being an accurate model. While SPT could not describe the physics of these small scales, it was assumed that small scale effects would not affect the models ability to describe larger scale dynamics. However, this was shown to be incorrect when it was found that SPT was not a convergent perturbation theory and did not accurately describe observations, facts which were attributed to small scale dynamics causing feedback on larger scales which, due to being incompatible with SPT, are referred to as non-perturbative effects. This problem was solved with the development of the Effective Field Theory of Large Scale Structure (EFTofLSS), a variant of SPT which introduces a cutoff, a minimum scale below which the model makes no attempt at describing reality, and a series of terms which correct the large scale calculations for the effects of smaller scale, sub-cutoff physics; these terms are referred to as counterterms.

In this thesis we develop the EFTofLSS, specifically studying the one-loop bispectrum and one-loop trispectrum while testing the commonly used EdS approximation, that being the simplified version of SPT which treates higher order density fields as though we lived in a matter dominated universe for mathematical simplicity. We show that when studying higher order correlators, it is important to use the full ΛCDM growth factors for the dark matter density fields. We also use the method of perturbation theory on the grid to constrain the EFTofLSS counterterms for the first time, leading to drastic improvements in the precision of our results when compared to previous studies which rely upon more conventional methodologies. We also show that it is important to account for the effects of finite time stepping and the rounding of numbers between time steps in the simulations, such that our model contains corrective terms for simulation imprecisions.

Finally, we discuss how the research presented in this thesis will impact near future LSS surveys and propose a number of possible future projects which could build upon this research.

Contents

List of Figures

1

Introduction

In a letter to the the Reverend Dr Richard Bentley in 1692, Newton proposed that an even distribution of gravitating matter in a finite space would convene into one spherical mass, but that an even distribution of gravitating matter in an infinite space *would never convene into one mass; but some of it would convene into one mass and some of it into another, so as to make an infinite number of great masses, scattered at great distances from one to another throughout all that infinite space. And thus might the sun and fixed stars be formed, supposing the matter were of a lucid nature*.

Since then, we have discovered that the Universe contains not only the visible, baryonic matter, which Newton was familiar with, but also dark matter, which does not interact electromagnetically, as well as relativistic particles and light which we call radiation and an unknown source of gravitational motion which we model through a mathematical object called the cosmological constant*. Indeed, at the present time, Newton's lucid matter constitutes only about one tenth of all the gravitating matter in the Universe, with dark matter constituting approximately one third, and the cosmological constant dominating cosmic dynamics, with radiation making a small but not insignificant contribution.

The multifaceted dynamics introduced by these mutually interacting constituents of the gravitational universe were not accounted for in Newton's ideas, but the principle he expressed in 1692 holds true. The cosmological constant describes a substance which is causing everything in the Universe to become increasingly separated, such that the Universe as a whole is usually described as expanding. This creates an effectively infinite volume, as

*Understanding the physical origins of the cosmic dynamics described by the cosmological constant is one of the primary concerns of modern cosmology, with a significant amount of effort being put into models which feature a new form of matter called dark energy which the cosmological constant could be an approximate description of. In this thesis, we treat the cosmological constant as being a mathematical constant of uncertain physical origin and do not concern ourselves with the many hypotheses regarding the physical nature of this source of gravitational force.

this expansion causes certian regions to lose causal contact with one another. Furthermore, given that we have only experienced a finite amount of time since the dawn of the Universe, we live in an era in which our distribution of gravitating matter would not yet have convened into one spherical mass even if the Universe were not expanding; indeed, we can see around us today a myriad of great masses and the many smaller masses that compose them distributed across the sky. The origins of these modern cosmological structures originates in the very early Universe, when it is believed a scalar field called the inflaton caused the Universe to expand by many orders of magnitude before decaying into the particles that exist today; while causing the Universe to expand, the inflaton field is believed to have experienced fluctuations in its energy density due to pair production which led to small inhomogeneities in the resulting matter fields. Immediately after inflation, charged particles and light were coupled in a hot plasma, but as the Universe expanded and cooled, the electrons and protons in the plasma formed neutral atoms in an event called recombination, allowing the light to travel relatively freely through the Universe. During this period, density inhomogeneities were very small compared to the almost homogeneous background they perturbed, and a map of their initial distribution can be estimated from observations of the Cosmic Microwave Background (CMB), the remnant of the light that decoupled from matter during recombination. However, over time, gravitational attraction caused them to increase until the Universe contained within it the galaxies, stars, and people we see around us today, whose densities are many orders of magnitude greater than that of the average density of the relatively homogeneous cosmic background.

For much of the history of science, physics has been dominated by the performing of open ended experiments and the subsequent interpretation of their results. However, in the modern era, our knowledge of how to describe our Universe is detailed enough, and the number of competing hypotheses for describing fundamental phenomenon are numerous enough, that in order to learn anything new we must instead set up precise predictions of how different physical parameters will affect observations and perform experiments and observations to directly rule out as many models as possible. Thus, it is not uncommon to hear the present era describes as the era of precision cosmology. In order to engage in such precision cosmology, we must be able to set up a system by which highly precise predictions can be made for the observable effects of as many competing models as possible; only then will we be able to meaningfully constrain our parameter space of potential descriptions of the present and predictors of the future.

Accurately and precisely modelling the statistical distribution of observables dispersed throughout the sky provides one of the best methods for performing these constraints. This modelling generally consists of creating an analytic system of convolutions describing the

correlations between observables at given locations in the sky and fitting fundamental physics dependent free parameters to the results of simulations; by then comparing these models to observational data, constraints can be placed on the parameter spaces of these fundamental physical models.

Predictions and observations of the CMB have provided a number of significant insights into fundamental physics over the past two decades and continue to do so, while cosmological Large Scale Structure (LSS), the distribution of dark and baryonic matter across the Universe on large scales, promises to provide a new set of observational data which will allow for more precise constraining of gravitational phenomenon such as dark energy and neutrino masses. Some examples of the surveys that will be providing datasets in the coming decade are Euclid [1], an ESA satellite based mission which intends to provide visible and infrared imaging and spectroscopy across a deep volume of space, the Spectro-Photometer for the History of the Universe, Epoch of Reionisation, and Ices Explorer (SPHEREx) [2], a NASA satellite based mission which will spectroscopically probe a smaller volume of space with a higher precision, complementing the Euclid data and allowing cross-correlations between their results. Other examples include the Legacy Survey of Space and Time (LSST) [3], which aims to use a ground based telescope to observe a deep volume of sky in optical and infrared wavelengths, and the Square Kilometre Array (SKA) [4], a more broadly applicable ground based radio telescope which will be used for a variety of high redshift observations which will probe far earlier times than the other surveys mentioned.

Of course, in order for any of these observational datasets to be put to use, an accurate model of LSS must be created to which they can be compared. Thus, the development of an accurate and reliable mathematical model of LSS distribution functions is one of the principal aims of modern cosmology and is the subject of concern for this thesis.

From the early 1980s until the beginning of the last decade, there was a long running attempt to describe LSS in a parameter free approach referred to as Standard Perturbation Theory (SPT) [5–7], which could then be modified with the incorporation of model dependent parameters to study the effects of fields and particles not included in the unmodified ΛCDM model. This system of equations begins with a fluid approximation to the Boltzmann equation describing an ensemble of collisionless particles which represent dark matter. Solutions to these equations are approximated with a power series. However, the results of SPT beyond linear order in its power series are in tension with simulations and observations; this is primarily because the formation of gravitationally collapsed objects such as dark matter halos and baryonic galaxies leads to effects on all scales that cannot be modelled by the simple power series approximation.

To solve this problem, a modified version of SPT, called the Effective Field Theory of Large Scale Structure (EFTofLSS) [8–11], has been developed. Initially proposed in 2010 [8], the EFTofLSS introduces an arbitrarily chosen cutoff Λ beyond which physics is non-perturbative. The coarse grained equations of motion are now Λ-dependent and, through their origins as fluid dynamical equations, contain an effective stress-energy tensor that captures the non-perturbative effects that plague SPT, namely microscopic velocity dispersion and convolutions of small scale density perturbations. The new terms arising from this tensor are called counterterms and account for small scale deviations from the pressureless perfect fluid assumed by SPT, absorbing divergences and the perturbative terms' dependence on Λ. Thus, the new terms introduced by the stress-energy tensor into the EFTofLSS not only allow for the accurate modelling of the large scale effects of the small scale, non-perturbative physics that SPT could not capture, but also ensures that the model will remain cutoff independent.

A lot of attention has been devoted to the EFTofLSS at the level of the power spectrum [9, 10, 12], the two-point correlator and therefore the simplest statistic in LSS, while less attention has been devoted to the bispectrum [13, 14] and trispectrum [15, 16], the tree and four point correlators, respectively. The higher order statistics offer additional information as well as the opportunity to perform consistency checks with the EFTofLSS parameters calculated from the power spectrum and to break degeneracies that arise from the study of a single observable. Further tests of the EFTofLSS bispectrum have also been performed in [17] and their calculations have been pushed to two-loop order in [18]. We improve upon these results by implementing the full ΛCDM time dependence rather than the commonly employed Einstein-de Sitter approximation for cosmological perturbation theory and cancelling cosmic variance through realisation perturbation theory. The ΛCDM growth factors up to third order were derived in [19], but have not been widely used since it was shown that they lead to a subleading correction to the one-loop power spectrum. However, we base our analysis upon the observation that the leading order terms in all higher order correlators contain non-linear density fields and that it is non-linear density fields which encounter corrections when changing growth factor, such that, unlike in the case of the power spectrum, the corrections will be incorporated into the leading order as well as subsequent order perturbative terms, and may therefore lead to corrections of the same order of magnitude as those subsequent order terms. Starting with [20], realisation perturbation theory has been shown to lead to significant improvements over regular perturbation theory in the precision of perturbative results when compared to simulation data for a given number of simulation realisations. However, until the research presented in this thesis was first published, it had not seen use in analysis of the EFTofLSS. We implement these corrections and methods into the EFTofLSS

and analyse their effects on the power spectrum, bispectrum, and trispectrum and discuss the improvement we see in our results.

Both SPT and the EFTofLSS model the dark matter density field of the Universe. In order to model the distribution of observable galaxies, whose distribution correlates with but does not perfectly mimic that of the underlying dark matter field, a phenomenon known as biasing, one must incorporate new biasing parameters into the model and compare them to observations and hydrodynamical simulations which model both dark and baryonic matter aggregation [21]. Recently, the potential of the EFTofLSS to deliver unbiased cosmological constraints has been proven in a blind analysis of a dark matter simulation suite [22] and to perform an analysis of galaxy correlators in the BOSS survey [23, 24]. In this thesis we do not concern ourselves with biasing but focus entirely on developing the dark matter model of the EFTofLSS in ΛCDM cosmology.

The research presented in this thesis makes use a simulation suite previously studied in [14, 12]. It is based on a $\Omega_{\mathrm{m},0} = 0.272$, $\sigma_8 = 0.81$, $n_\mathrm{s} = 0.967$ cosmology with $h = 0.724$. The $N_\mathrm{p} = 1024^3$ particles in a cubic box of dimension $L = 1500h^{-1}$ Mpc are set up at initial redshift $z_\mathrm{i} = 99$ using 2LPT [25] and then evolved to $z = 0$ using Gadget 2 [26]. We are considering 14 realisations of this simulation volume.

This thesis is structured as follows: first, we will review the physics of structure formation and the models of SPT and the EFTofLSS. We will then review the numerical simulations and the technique of gridPT before presenting regularisations of the one-loop power, bi-, and trispectra. We will present in full detail the methods and results used to regularise the spectra in our recent publications [27] and [28].

2

Gravity

THE two forces which play a major role in the formation of cosmological structure are gravity and electromagnetism. Gravity affects both baryonic and dark matter, while electromagnetism appears to only affect baryonic matter. A full study of baryonic structure formation and its feedback effects on dark matter would require both forces to be taken into account; however, in this thesis we restrict ourselves to studying dark matter clustering in isolation, such that gravity is the only force we need to include in our model.

In this chapter, we will briefly review the motivation and formulation of both Newtonian and relativistic models of gravity. These introductions will allow for a clearer understanding of the concepts described later in the thesis.

2.1 | Newtonian Mechanics

During the Great Plague of London in 1665, Isaac Newton retreated to his mother's country estate where he could be comparatively safe from the pestilence. While there, over a period of 18 months, he formulated the basic elements of modern calculus and classical mechanics, including the three Newtonian laws of motion and the law of universal gravitation. These laws are still taught and used in research today, where they form the basis of what is commonly referred to as Newtonian or classical mechanics. While Newton's law of universal gravitation has been surpassed by general relativity as the most accurate model of gravitational fields available to modern physicists, it remains an approximation that requires only minor corrections when describing most astrophysical and cosmological systems. However, it describes mass distributions that are spherical in nature and is non-trivial to generalise to other shapes. An alternative formulation of classical mechanics based upon potential theory and formulated in the 18th century allows classical gravitation to be extended to systems with arbitrary geometries.

2.1.1 | Newton's Laws of Motion

Newton's first law of motion states that an object travelling with a given speed in a given direction will continue to travel with that speed and in that direction unless acted upon by an external force.

Newton's second law states that $F = ma$, that being the quantitative statement that the force required to impart a given amount of acceleration on a given inertial mass is equal to the acceleration imparted weighted by the object's mass.

Newton's third law states that for every action there is an equal and opposite reaction; that meaning, for every force that is applied upon one mass by another, the imposing mass will have an equal force applied upon itself in the opposite direction by the mass upon which it is imposing its force*.

The first two laws express much the same idea; a change in motion, by definition, maps to an applied force. Thus, one could phrase the idea qualitatively as *an object will not experience acceleration without the application of a force* or quantitatively by defining force as being the acceleration combined with an intrinsic property of the object, which we refer to as inertial mass. The third law does not follow directly from the first two in the same way that they follow from each other, but a rephrasing of the second law as $F_1 = -F_2 = m_1 a_1 = m_2 a_2$ for two interacting objects, one with mass m_1, force experienced due to the interaction F_1, and resultant acceleration a_1, and the other with mass m_2, force F_2, and resulting acceleration a_2, would allow for a single law which contains within it the content of all three of the above laws, and in which masses clearly serve as weightings mapping accelerations to applied forces, allowing for the notion that the same force can produce different accelerations in different objects.

2.1.2 | Newton's Law of Universal Gravitation

As with other forces, a classical model of gravity is defined by charges; specifically, we can define two gravitational charges that all particles may be described as having: active gravitational charge, g^{a}, which defines the force that particle will exert on nearby particles, and passive gravitational charge, g^{p}, which defines how strong a force a particle will feel in reaction to another particles gravitation; the force incurred upon a particle by another at a given distance will then be determined by the product of the attracting particles active charge and the attracted particles passive charge.

*Of course, this introduces the notion that which of the two objects is conceptualised as imposing the force upon the other and experiencing the reaction is an arbitrary decision of each observer.

Newtonian gravity begins with the observations that in a three-dimensional universe, gravitational force decreases with distance r as $1/r^2$ due to its expanding spherical dispersion around any gravitating body and that the gravitational force felt towards any spherical gravitating object will be directed towards its centre. As such, the simplest way to model the gravitational force imposed by a spherical object with active gravitational charge g_1^{a} upon an object with passive gravitational charge g_2^{p} separated by a distance r is given by[†]

$$F_{\mathrm{g}}^{\mathrm{N}} = \frac{g_1^{\mathrm{a}} g_2^{\mathrm{p}}}{r^2} \,, \tag{2.1}$$

thus defining the Newtonian gravitational force. By incorporating the requirement that the two objects experience equal and opposite forces, one may see that the active and passive masses of a given object must be proportional to each other; by choosing an appropriate unit for both of them, they can be equated, and will be treated as being a single charge for the remainder of this thesis, $g^{\mathrm{a}} = g^{\mathrm{p}} = g$.

2.1.3 | The Newtonian Potential

Eq. (2.1) works as a classical model of the gravitational force imposed by a spherical mass distribution. However, it does not trivially generalise to non-spherical distributions, limiting its utility. While most large, rotating celestial bodies are roughly spherical, many asteroids and other bodies are not, and a model of Newtonian gravity which can be applied easily to such irregularly shaped masses needs an alternative formulation.

In 1813, Poisson generalised the Laplace equation to sourced potentials[‡] by proposing that[§]

$$\partial^j \partial_j \phi(x^i) = -4\pi\rho(x^i) \,, \tag{2.2}$$

[†]To account for arbitrary choices of units, a conversion factor is often included in this equation; in the case of SI units, this factor is called the gravitational constant, G.

[‡]The Laplace equation, $\partial^j \partial_j \phi = 0$, is valid for describing fields in the absence or sources and sinks. Since forces, by definition, are sourced by charged particles and have no effect in their absence, the Laplace equation cannot be used to accurately describe any fundamental force, but it can be used to describe the dynamics of fluids in sourceless environments, such as water in a frictionless container. Phrased in English, the equation reads *the amount of field, that being the rate of change in the potential, that is lost or gained in the absence of a source or sink is zero*. In other words, without something to create or remove gradient in a potential, the overall gradient will remain the same indefinitely.

[§]In the case of gravity with SI units, this becomes

$$\partial^j \partial_j \phi(x^i) = -4\pi G\rho(x^i) \,.$$

where $\rho(x^i)$ is the density of the source at coordinates x^i. This is the Poisson equation of gravitational potentials and can be phrased in English as *gravitational fields, which are the gradient of gravitational potentials, are sourced by and equal to a weighting of mass densities*.

Eq. (2.2) can be solved to give[¶]

$$\phi(x^i) = \int dx^j \frac{\rho(x^j)}{|x^i - x^j|} \ , \tag{2.3}$$

which can be used to calculate the potential induced by a gravitating object of any shape. Once the potential has been calculated, the gravitational acceleration in any given dimension α experienced by an object in the vicinity of the object responsible for the potential is given by[‖]

$$\partial_t^2 r^i = \partial_i \phi \ . \tag{2.4}$$

2.1.4 | The Euler Equation

In the context of gravitating matter on large scales, the only forces that are relevant are the gravitational force, F_g, which will draw all dark matter particles towards one another, and the pressure generated by collisions between particles, F_p, which will push them apart[**]. Remembering Newton's laws of motion and noting that we are now dealing with a sum of two forces, $F = F_\mathrm{p} + F_\mathrm{g}$, $F = ma$ becomes

$$\int_V dV \, (-pn + \rho\phi) = \int_V dV \rho \frac{Dv^i}{Dt} \ . \tag{2.5}$$

[¶]In the case of SI units, a factor of G multiplies the integral.

[‖]This follows from the definition of a force's potential $\phi(x^i)$, which is the amount of energy transfer required to move an object of a given mass from point x^i to a point infinitely far away from the source of the potential. Thus, in order to move from a region with potential ϕ_a to one with potential ϕ_b, one would require an additional amount of energy equal to $\phi_b - \phi_a$ to move to an infinite distance; in the event that $\phi_b < \phi_a$, this will of course be negative, indicating that less energy is required to travel to infinity and, by extension, that that amount of energy has been expended in the transport. By the model of gravitation given in potential theory, geodesics will naturally travel in the direction of increasing potential energy unless another source of energy counteracts it.

[**]Pressure is the result of large numbers of electromagnetic interactions between closely spaced particles; dark matter appears to have no electromagnetic charge and will therefore have negligible if any pressure, such that the pressure terms can usually be set to zero. However, we derive the Euler equation in full as we find that the pressure terms in the equation may be used to represent physical effects other than pressure under certain circumstances, as will be explored in Chapter 5.

where V is the volume in which the fluid is contained, v^i is the velocity of the fluid flow, p is the pressure of the fluid, n is the number density of the particles making up the fluid, and ϕ is the fluid's gravitational potential as defined in Eq. (2.2).

Applying divergence theorem to Eq. (2.5), one obtains

$$\int_V dV \left(-\partial_j p^i - \rho \partial_i \phi\right) = \int_V dV \rho \frac{Dv^i}{Dt} \,. \tag{2.6}$$

Noting that the integrals are over the same volume and that the total derivative of the velocity is given by

$$\rho \frac{Dv^i}{Dt} = \rho \left(\partial_t + v^j \partial_j\right) v^i \,, \tag{2.7}$$

we can equate the integrands and arrive at the Euler equation:

$$\partial_t v^i + v^j \partial_j v^i = -\frac{\partial_j p^i}{\rho} - \partial_j \phi^i \,. \tag{2.8}$$

The Euler equation is one of the most important equations in fluid dynamics and describes the gravitation and pressure of a fluid in terms of the mass and velocity of its constituent particles. Eq. (2.8) can be rephrased in English as *the change in the overall pressure and gravitational field of a fluid is equal to the acceleration weighted by mass of the sum of all particles making up the fluid*.

In the event that the fluid under description is located in an expanding background, that meaning that the particles constituting the fluid are feeling an additional force pulling them apart at all times, a new term must be added into Eq. (2.8) to account for these effects by altering the fluid density with time. If we normalise the rate of expansion of the fluid to the magnitude of the fluid's background at a given time, such that we define the expansion parameter $E(t) = \dot{d}(t)/d(t)$ for distance between particles d and note that this new parameter will have dimensions of inverse time, we may conclude that in order to be a valid contribution to the Euler equation it must be multiplied by a term with dimensions of distance per unit time; in other words, a velocity term. Inserting this new term we have constructed into Eq. (2.8) and noting that, in the case of a perfect fluid, we have that the stress-energy tensor is defined as

$$\tau^{\mu\nu} \equiv \begin{bmatrix} \rho & 0 & 0 & 0 \\ 0 & p^1 & 0 & 0 \\ 0 & 0 & p^2 & 0 \\ 0 & 0 & 0 & p^3 \end{bmatrix} \,, \tag{2.9}$$

such that its non-zeroth components are $\tau^{ij} = \delta^{(\mathrm{K})ij} p^i$, Eq. (2.8) may be generalised to become the Euler equation for variable backgrounds:

$$\partial_t v^i + E v^i + v^j \partial_j v^i + \partial^i \phi = -\frac{1}{\rho} \partial_j \tau^{ij} \ . \tag{2.10}$$

2.2 | General Relativity

In 1905, Albert Einstein published his theory of relativity [29]. This theory begins with the axiom that the laws of physics will appear the same to all observers who are in uniform states of motion with respect to one another. It then derives from this axiom a set of equations of motion which imply that space and time are both experienced differently by observers in different states. In 1915, he published his field equations of gravitation [30], which originated from a generalisation of relativity to include observers who are accelerating with respect to one another; this more generalised theory was soon known as general relativity and his original theory of relativity, which could now be seen as being a specialised case of general relativity which applied only to regions which lacked any forces, became known as special relativity.

In general relativity, gravity is modelled as being the modification of geodesics, the paths objects will follow if subjected to no external forces, on a four dimensional Lorentzian manifold called *spacetime*. Spacetime itself is a model of combined space and time which can be taken to be the set of all possible geodesics connecting any given points that fall within its domain. Spacetime manifolds which describe a flat space are referred to as Minkowski manifolds and possess the Minkowski metric,

$$\eta_{\mu\nu} \equiv \begin{bmatrix} -1 & 0 & 0 & 0 \\ 0 & 1 & 0 & 0 \\ 0 & 0 & 1 & 0 \\ 0 & 0 & 0 & 1 \end{bmatrix} \ . \tag{2.11}$$

2.2.1 | Special Relativity

Special relativity begins with the observation that the notion of simultaneity of observation is not valid in a universe with a finite speed of signal propagation; specifically, in a universe with a finite speed of light.

The notion that the witnessing of events occurs at different times to different observers is not new; sound, for example, has long been known to propagate at a finite speed, defined by

the medium in which it is travelling. However, this speed will vary depending on the speed of the observer who is watching the propagation of the sound wave; an observer moving at the speed of sound alongside a sound wave will witness the wave as being static, while an observer moving in the opposite direction to the wave's propagation will witness its speed increased. When formulating special relativity, Einstein began with the axiom that *the speed of light is constant for all observers*. That meaning all observers, regardless of their motion towards or away from a given event, will witness the same speed of light for any light signals propagating from that event. This axiom arose from the results of the Michelson-Morley experiment, first performed by Michelson from 1880 to 1881 and subsequently repeated by both Michelson and Morley in 1887, which, while attempting to measure the speed of the Earth with respect to a hypothesised luminiferous aether that was believed to be a fluid through which light flowed as waves, discovered instead that light signals appear to travel at the same speed regardless of the observers motion. Specifically, they measured the speed of propagation of light both in the direction of the Earth's motion and perpendicular to it, expecting to find that the former signal would travel faster due to the detecter moving towards the light source, but instead found no difference between the speeds.

The second axiom upon which special relativity is built is the notion that the laws of physics are the same for all observers; this one did not stem directly from any one experiment, but was an intuitive notion which was not opposed by the results of any experiments that had ever been conducted, nor by any that have been conducted since.

Beginning with these axioms, it becomes apparent that the usual rule of addition of velocities, which forms the basis of transforming from one observers frame of reference to another's in classical mechanics, is no longer valid, and an alternative set of transformations, known as Lorentz transformations, was proposed instead.

2.2.2 | The Equivalence Principle

Inertial mass, m, is a measure of the magnitude of an objects reaction to the application of a force upon itself; an object with a larger inertial mass will experience less acceleration towards or away from an attractive or repulsive force generator than an equivalent object with a smaller inertial mass. In theory there is no a priori reason to connect the inertial mass of an object with the magnitude of any of its force charges. A magnet, for example, may have a large electromagnetic charge and little inertial mass, or a large mass and little charge.

From naive interactions with the world, it has been suspected for centuries that gravitational charge and inertial mass are the same property; however, it was not until the Eötvös experiment, which intially ran in 1885 and saw improvements resulting in a much more conclusive set of tests from 1906 to 1909, that this was experimentally shown to be true to

a high degree of precision. The experiment consisted of placing a pair of weights at either end of a rod, upon which was also placed a mirror; the rod and its attachments were then suspended from above by a single fibre, allowing the rod to rotate freely. A light was then reflected from the mirror into a receiving telescope such that, were the rod to rotate, the light would not be detected by the telescope. The inertial mass of the weights reacted to the centrifugal force imposed by the Earth's rotation, while the gravitational charges of the masses caused them to be attracted to the Earth's gravity. The arrangement was such that the amount of rotation the rod would undergo would be proportional to $m_{\text{Earth}}/g_{\text{Earth}}$; if the inertial mass and the gravitational charge were the same, the rod would not rotate. The experiment found no meaningful rotation, empirically validating the hitherto merely intuitive notion that gravitational charge and inertial mass are the same.

This equivalence of gravitational charge and inertial mass, $g = m$, is referred to as the equivalence principle and is fundamental to the development of the modern gravitic theory of general relativity. The principle requires that at any point in any gravitational field there is a coordinate system that is locally inertial, that meaning a coordinate system in which the effects of the gravitational force are absent and any object following that gravitational field will appear to be following a kinematic path.

2.2.3 | Spacetime Geodesics

In the absence of gravity, an object's acceleration in a given coordinate x^α with respect to a parameter u which parametrises its trajectory[††] is simply

$$\partial_u^2 x^\alpha = 0 \,. \tag{2.12}$$

Intuitively, this tells us that the object will not accelerate in any direction; this is of course natural for a Minkowski space.

In order to generalise this to systems with non-trivial geometry, we may begin with a coordinate x^μ and study the transformation properties of its rate of change with u:

$$\partial_u x'^\rho = \partial_\mu x'^\rho \, \partial_u x'^\mu \,. \tag{2.13}$$

This first derivative transforms as a vector, but if we take the second derivative to find the transformation relations of the acceleration of the coordinate with respect to u, we see that it

[††]A simple example of what u might represent is the time shown on clock; regardless of whether the clock is following the trajectory under consideration or is experiencing a separate geodesic of its own, every time shown on its face should correspond to any object following that trajectory being at a particular point along it.

does not:

$$\begin{aligned}\partial_u^2 x'^\rho &= \partial_u \left(\partial_\mu x'^\rho \partial_u x'^\mu\right) \\ &= \partial_\mu x'^\rho \partial_u^2 x'^\mu + \partial_{\mu\nu} x'^\rho \partial_u x^\mu \partial_u x^\nu \ . \end{aligned} \tag{2.14}$$

Thus, $\partial_u^2 x^\mu = 0$ is not a covariant equation and is not therefore a valid generalisation of Eq. (2.12) to gravitating systems.

In order to correct for this, we need to introduce a new term which cancels the second term in Eq. (2.14). We can do this by defining

$$\partial_u^2 x^\lambda + \Gamma^\lambda_{\mu\nu} \partial_u x^\mu \partial_u x^\nu = 0 \ , \tag{2.15}$$

where the new object $\Gamma^\lambda_{\mu\nu}$, which we refer to as an affine connection, transforms as

$$\Gamma'^\tau_{\sigma\rho} = \partial_\lambda x'^\tau \partial_{\sigma'} x^\mu \partial_\nu x'^\sigma \partial_{\rho'} x^\nu \Gamma^\lambda_{\mu\nu} - \partial_{\mu\nu} x'^\tau \partial_{\sigma'} x^\mu \partial_{\rho'} x^\nu \tag{2.16}$$

and vanishes in a locally inertial coordinate system. This can also be written as a function of the metric for the given system,

$$\Gamma^\lambda_{\mu\nu} = \frac{1}{2} g^{\lambda\rho} \left[\partial_\nu g_{\rho\mu} + \partial_\mu g_{\rho\nu} - \partial_\rho g_{\mu\nu}\right] \ . \tag{2.17}$$

Any trajectory which solves Eq. (2.15) is a *spacetime geodesic* and describes the trajectory of a body in the gravitational field described by the metric which defines the affine connection. These trajectories are covariant, as can be seen by noting that, for any spacetime geodesic,

$$\int_{u_1}^{u_2} du \sqrt{g_{\mu\nu}(x(u)) \partial_u x^\mu(u) \partial_u x^\nu(u)} \tag{2.18}$$

is stationary under any coordinate transformations that leave $x^\mu(x)$ unchanged at the limits of the trajectory, u_1 and u_2.

However, we must note that Eq. (2.15) is not valid for all parametrisations of the trajectories; u must be a linear function of the proper time, τ, defined as

$$d\tau \equiv \sqrt{-g_{\mu\nu} dx^\mu dx^\nu} \ , \tag{2.19}$$

which measures the time recorded by an observer falling along the geodesic. Following from this, we can see that a natural alternative to writing the metric, when we wish to describe a given spacetime manifold, is to write down the square of the proper time or its equivalent, the line element, $ds^2 = -c^2 d\tau^2 = g_{\mu\nu} dx^\mu dx^\nu$.

2.2.4 | The Einstein Field Equations

Einstein began his derivation of the gravitational field equations with what he called the happiest thought in his life: *the gravitational field has only a relative existence in a way similar to the electric field generated by magnetoelectric induction. Because for an observer falling freely from the roof of a house there exists, at least in his immediate surroundings, no gravitational field.* To put it another way: at any point p in spacetime, there must be a coordinate system in which the metric is the Minkowski metric, $g_{\mu\nu} = \eta_{\mu\nu}$ whose derivatives vanish at p.

Einstein's theory of general covariance is an evolution of his special relativistic axiom that the laws of physics must be the same for all observers. Specifically, it states that the laws of physics should be expressible in a generally covariant manner and therefore modellable with tensors.

Taking into account both the notion of locally Minkowski coordinates and the theory of general covariance, one may model the generally covariant forms of any laws of physics observed in a locally inertial frame by making the transformations

$$\eta_{\mu\nu} \to g_{\mu\nu} \ , \qquad \partial_\mu A^\nu \to \partial_\mu A^\nu + \Gamma^\nu_{\mu\lambda} A^\lambda \ , \tag{2.20}$$

in other words, substituting the locally Minkowski metric for the spacetime metric in another coordinate system and replacing derivatives with covariant derivatives.

The curvature of a manifold, which in general relativity is the representation of gravity, is encapsulated in the Riemann curvature tensor:

$$R^\lambda_{\mu\rho\nu} = \partial_\rho \Gamma^\lambda_{\mu\nu} + \Gamma^\kappa_{\mu\rho}\Gamma^\lambda_{\nu\kappa} - \Gamma^\kappa_{\mu\nu}\Gamma^\lambda_{\rho\kappa} \ . \tag{2.21}$$

When contracted through its second lower index, it transforms into the Ricci tensor:

$$R_{\mu\nu} = R^\lambda_{\mu\lambda\nu} = \partial_\lambda \Gamma^\lambda_{\mu\nu} + \Gamma^\kappa_{\mu\lambda}\Gamma^\lambda_{\nu\kappa} \ , \tag{2.22}$$

which further contracts to give the Ricci scalar:

$$R = R^\lambda_\lambda \ . \tag{2.23}$$

Since Einstein's theory of general relativity began with the notion that gravity could be modelled as curvature in spacetime, and given that gravity requires the presence of gravitating matter to exist, Einstein's starting point in the derivation of his field equations was the rather intuitive notion that in a vacuum, there should be no gravitational curvature; in other words,

the Ricci tensor of the spacetime manifold should vanish:

$$R_{\mu\nu} = 0 \, . \tag{2.24}$$

By remembering the definitions of the Ricci scalar given in Eq. (2.22), one may rewrite Eq. (2.24) as the Einstein field equations for a vacuum:

$$g^{\nu\rho} R_{\mu\nu} = \partial_\lambda g^{\rho\beta} \Gamma^\lambda_{\mu\beta} + \kappa \left(t^\rho_\mu - \frac{1}{2} \delta^\rho_\mu t \right) = 0 \, , \tag{2.25}$$

for constant κ, vacuum stress-energy tensor of the gravitational field $t_{\mu\nu}$, and its contraction $t = t^\mu_\mu$ where

$$t_{\mu\nu} \equiv \frac{1}{2\kappa} \left(\delta^\sigma_\mu g^{\alpha\beta} \Gamma^\eta_{\alpha\lambda} \Gamma^\lambda_{\beta\eta} - g^{\alpha\beta} \Gamma^\sigma_{\alpha\lambda} \Gamma^\lambda_{\beta\mu} \right) \, . \tag{2.26}$$

To derive a more general set of field equations which allow for the presence of matter as well as a gravitational field, Einstein introduced a more general stress-energy tensor: $t_{\mu\nu} \to t_{\mu\nu} + \tau_{\mu\nu}$, where $\tau_{\mu\nu}$ is the stress-energy tensor for matter. By substituting this into Eq. (2.25), we can arrive at the familiar Einstein field equations of gravitation in the presence of a general stress-energy tensor[‡‡]:

$$R_{\mu\nu} - \frac{1}{2} g_{\mu\nu} R = 8\pi \tau_{\mu\nu} + \Lambda g_{\mu\nu} \, , \tag{2.27}$$

where

$$\tau_{\mu\nu} = (\rho + p) u_\mu u_\nu - p g_{\mu\nu} \tag{2.28}$$

for density ρ, pressure p, and velocity vector of the fluid being described u_α, and the cosmological constant Λ models effects on the manifold which are not described by the stress energy tensor[§§].

[‡‡] In the case of SI units, the stress-energy tensor is rescaled by G.

[§§] The cosmological constant was originally introduced into Eq. (2.27) by Einstein in 1917 to counteract cosmic expansion and allow his description of the Universe to remain static; at the time, the age and history of the Universe were not known and it was generally believed to be neither expanding nor contracting. Upon the discovery that the Universe is actually expanding, that meaning that the ratios of the sizes of fundamental particles to the distances between them are decreasing with time in a manner that, while not strong enough to affect closely interacting particles, leads to distantly spaced objects become increasingly far apart, he began disregarding the constant; lore has it that he described its introduction as his greatest blunder. However, the notion of a constant term which describes matter effects which are independent of the stress-energy tensor provides the ability to modify our description of gravitation in accordance with observed phenomenon; by comparison with observations made over the past several decades, it has ironically found itself being used to describe the acceleration of cosmic expansion, rather than eliminating it.

2.2.5 | Scalar Fields on Spacetime

Many cosmological models begin by defining a spacetime manifold and modify it to fit to observations by including a scalar field ψ with an action given by

$$S_\phi = -\int d^4x\sqrt{-\mathrm{Det}(g)}\left[\frac{1}{2}g^{\mu\nu}\partial_\mu\psi\partial_\nu\psi + V(\psi)\right] , \tag{2.29}$$

where $V(\psi)$ is the potential of the scalar field. The existing spacetime manifold can still be used on the condition that the metric does not vary as a function of ψ. The energy-momentum tensor for the scalar field can be found by varying the metric and removing the components present before the inclusion of the field and is given by

$$\tau_\phi^{\mu\nu} = -g^{\mu\nu}\left[\frac{1}{2}g^{\rho\sigma}\partial_\rho\psi\partial_\sigma\psi + V(\psi)\right] + g^{\mu\rho}g^{\nu\sigma}\partial_\rho\psi\partial_\sigma\psi . \tag{2.30}$$

This has the form of the energy-momentum tensor of a perfect fluid with energy density, pressure, and four-velocity given by

$$\rho = -\frac{1}{2}g^{\mu\nu}\partial_\mu\psi\partial_\nu\psi + V(\psi) , \tag{2.31}$$

$$P = -\frac{1}{2}g^{\mu\nu}\partial_\mu\psi\partial_\nu\psi - V(\psi) , \tag{2.32}$$

$$u^\mu = -\left[-g^{\rho\sigma}\partial_\rho\psi\partial_\sigma\psi\right]^{-\frac{1}{2}} g^{\mu\tau}\partial_\tau\psi . \tag{2.33}$$

2.2.6 | The Newtonian Approximation of Weak Field Relativity

In relativistic gravity, geodesics are obtained from a metric $g_{\mu\nu}$ through the line element

$$ds^2 = g_{\mu\nu}dx^\mu dx^\nu . \tag{2.34}$$

For any differentiable manifold, the tensor must be locally Minkowski on small scales, such that one can write $g_{\mu\nu} = \eta_{\mu\nu} + h_{\mu\nu}$ for Minkowski metric $\eta_{\mu\nu}$ and perturbation metric

$$h_{\mu\nu} = (\phi\eta)_{\mu\nu} - \eta_{\mu\nu} , \tag{2.35}$$

for diffeomorphism ϕ mapping $\eta_{\mu\nu}$ to $g_{\mu\nu}$, which can be physically interpreted as the gravitational potential.

From the weak field approximation one finds that

$$R_{00} = \nabla_{\boldsymbol{r}}^2\phi , \tag{2.36}$$

such that the 00 component of the field equations becomes

$$\nabla^2_{\boldsymbol{r}}\phi = 4\pi G(\rho + 3p) - \Lambda \,. \tag{2.37}$$

In the limit $v \ll c$ and $h \ll 1$, this leads to the geodesic equation

$$\partial_t^2 r^\alpha = -\partial_\alpha \phi \,. \tag{2.38}$$

Eqs. (2.37) and (2.38) are the equations of Newtonian potential gravity, as given in Eq. (2.2) and (2.4), respectively. Thus, Newtonian gravity emerges as the limiting case of relativistic gravity in the case that spacetime can be treated as almost entirely Minkowski and populated by non-relativistic matter.

2.3 | Summary

In this chapter, we have reviewed both classical and relativistic gravity, ultimately deriving the Einstein field equations and describing how they can be modified to include scalar fields, such as the inflaton field which will be discussed in more detail in Chapter 4. We have also shown that the use of Newtonian mechanics to describe weak gravitational fields without recourse to solving the field equations is not only a useful approximation but that Newtonian gravity is actually the weak field limit of relativistic gravity, such that this approximation has a basis in the mathematics of general relativity as well as the more intuitive basis provided by its agreement with physical observations. The research presented in this thesis is based entirely upon weak field gravitational interactions and makes use of the Newtonian approximation; while a study of the same physics with relativistic gravity may lead to small corrections, previous studies of large scale structure physics have shown that such relativistic corrections are usually small enough that a Newtonian treatment is adequate for creating models to compare with current cosmological survey data. In Chapter 10 we discuss the possibility of a future research project which explores the magnitude of these relativistic corrections.

3

A Homogeneous Universe

In this chapter we discuss the notions of homogeneity and isotropy and how they form the bases of the principal model of large scale structure across the Universe. We then formulate this model in detail, beginning with a derivation of the most general metric to describe a homogeneous and isotropic universe and the equations of motion that result from its use as a solution to the Einstein field equations, before discussing specific solutions to these equations of motion and how they relate to our understanding of cosmology.

3.1 | Homogeneity and Isotropy

A homogeneous universe is translation invariant, such that an observer sees the same distribution of matter regardless of their spatial location. More precisely, a homogeneous universe is described by a spacetime that, when foliated into spacelike hypersurfaces, permits isometries in $g_{\mu\nu}$ between any points upon each spacelike hypersurface. Thus, while with present technology we are limited to observing the Universe from our Solar System, if the Universe is homogeneous, we should see that the statistical distribution of matter is the same at any given time when viewed from any other location.

An isotropic universe is rotationally invariant, such that an observer sees the same distribution of matter regardless of the angle at which they have rotated about a stationary axis. More precisely, an isotropic universe is described by a spacetime for which, taking any point p, timelike vector through that point u^μ, and space of vectors orthogonal to u^μ at p, V_p, there exist spacelike vectors $s_1^\mu s_2^\mu \in V_p$ and an isometry in $g_{\mu\nu}$ which maps s_1^μ to s_2^μ while leaving p and u^μ unchanged. In this definition, u^μ represents the position of a static observer at a given point in space and the tangent vector space represents all possible lines of sight that observer may have, rotating about their static axis, at a given timeslice. Thus,

in an inhomogeneous universe, the distribution of matter on large scales will look the same regardless of which way we turn at a given point.

In 1917 [31], Einstein argued that the Universe could be accurately modelled as a closed, homogeneous system; this was in keeping with unmodified general relativity and with Mach's Principle, which asserts that the combined, weak frame dragging of the matter throughout the Universe is responsible for the Universe's apparent preferred rotational frame at any given point in space. In 1926 [32], Hubble showed observationally that large scale structure seemed homogeneous and this was reinforced by Lemaître's study of galaxy redshifts in 1927 [33] and a number of subsequent surveys over the next several years. Subsequent observations, including the results of the most recent contemporary LSS surveys, show that, on large scales, the Universe is indeed both isotropic and homogeneous to a very high level of precision.

In the case of a homogeneous and isotropic universe, cosmic geometry must be constant. Variations in the curvature of the Universe would constitute inhomogeneities and anisotropies in of themselves and would lead to visible alterations in matter dynamics in their local regions; furthermore, given the relation between spacetime geometry and matter, such a curvature perturbation would imply the pre-existence of an inhomogeneity in the matter density distribution. As such, we will take the Universe to have constant curvature for the remainder of this thesis. In the case that cosmic Gaussian curvature is positive, the Universe will have the overall shape of the surface of a 3-sphere, in the case that it is negative, the Universe will have an overall shape of the surface of a 3-pseudosphere, and in the case that the curvature is zero, it will be a flat, Euclidean 3-plane on large scales.

3.2 | The FLRW Metric

The metric defining lengths in a Euclidean space is simply

$$ds^2 = dx^2 \tag{3.1}$$

and those defining lengths along the surface of a 3-sphere or 3-pseudosphere are

$$ds^2 = dx^2 \pm dz^2 \,, \tag{3.2}$$

where a positive second term on the right hand side would allow for the calculation of distances on the surface of a 3-sphere and a negative sign would allow for the calculation of distances on the surface of a 3-pseudosphere, we have used a Cartesian coordinate system with arbitrary metrics defined on the surface x^i and z^i for simplicity, and these vectors must

satisfy

$$z^2 \pm x^2 = a^2 \ , \tag{3.3}$$

for radius of the sphere or pseudosphere a with the sign of the second term in Eq. (3.3) being the same as the sign of the second term in Eq. (3.2).

We can choose to rescale our coordinates by defining $x^i \to x^i/a$ and $z^i \to z^i/a$, such that Eq. (3.2) becomes

$$ds^2 = a^2 \left[dx^2 \pm dz^2\right] \tag{3.4}$$

and Eq. (3.3) becomes

$$z^2 \pm x^2 = 1 \ . \tag{3.5}$$

The reason for doing this seemingly arbitrary redefinition is to allow us to turn the metric into an explicit function of the radius of the sphere or pseudosphere in question; this will allow us to perform calculations on the surface of an expanding or contracting sphere or pseudosphere.

To allow the metric to be easily parametrised to describe any arbitrarily spherical, pseudospherical, or Euclidean plane, we introduce the curvature parameter $k \equiv 1/a^2$ to provide measure of the Gaussian curvature of the our dimensional shape upon which the plane resides, such that Eq. (3.4) becomes

$$ds^2 = a^2 \left[dx^2 + kdz^2\right] \tag{3.6}$$

and Eq. (3.5) becomes

$$z^2 + kx^2 = 1 \ , \tag{3.7}$$

where the value of k allows for the following surfaces:

$$k \begin{cases} > 0 & \text{spherical plane} \\ < 0 & \text{pseudospherical plane} \\ 0 & \text{Euclidean plane} \end{cases} \tag{3.8}$$

If $k = 0$, the Universe is said to be flat and its geometry results in parallel geodesics remaining parallel indefinitely. If the Universe is spherical, we would expect all geodesics to be closed in keeping with the notion of our living on the surface of a 3-sphere. If the Universe is pseudospherical, we would expect to observe divergent parallel geodesics and a hyperbolic geometry, in keeping with the notion of our living on the surface of a 3-pseudosphere. However, observations indicate to a high degree of precision that we live in a universe with a negligable amount of curvature, such that $k \approx 0$.

In order to simplify Eq. (3.6), we may note that the derivative of Eq. (3.7) gives

$$z dz^i + k x^j dx_j = 0 \,, \tag{3.9}$$

such that Eq. (3.6) becomes

$$ds^2 = a^2 \left[dx^2 + k \frac{x^j dx_j^2}{(1 - k x^i)^2} \right] \,. \tag{3.10}$$

Converting Eq. (3.10) to spherical coordinates, in which

$$dx^2 = dr^2 + r^2 d\Omega \,, \tag{3.11}$$

for solid angle

$$d\Omega \equiv d\theta^2 + \sin^2\theta d\phi^2 \,, \tag{3.12}$$

gives us

$$ds^2 = a^2 \left[\frac{dr^2}{1 - kr^2} + r^2 d\theta^2 - r^2 \sin^2\theta d\phi^2 \right] \,, \tag{3.13}$$

the metric form for which is

$$g_{ij} = a^2 \begin{bmatrix} \frac{dr^2}{1-kr^2} & 0 & 0 \\ 0 & r^2 d\theta^2 & 0 \\ 0 & 0 & r^2 \sin^2\theta d\phi^2 \end{bmatrix} \,. \tag{3.14}$$

Observations show that we live in an expanding universe (see Appendix A for a discussion of causal implications of this which will become important in Chapter 4). Thus, the separation between points r and the local curvature of space k will be time dependent. As the Universe expands, we define a time dependent scale factor to be equal to the radius of the pseudosphere underyling our cosmic plane, $a \to a(t)$, and normalise it such that $a(t_0) = 1$ where t_0 represents the present time. As the Universe expands or contracts, spatial separations will evolve as $r(t) = a(t) r$, where we refer to this new r as the comoving separation.

In order to turn Eq. (3.13) into a solution to Eq. (2.27) which can describe a relativistically gravitating universe, we must include a temporal term. In a homogeneous and isotropic universe, there is no reason for time to flow differently at different locations, such that the change in time can be simply measured as cdt; thus, we arrive at the most general metric

compatible with a closed, homogeneous, and isotropic universe:

$$g_{\mu\nu} = \begin{bmatrix} dt^2 & 0 & 0 & 0 \\ 0 & \frac{a^2 dr^2}{1-kr^2} & 0 & 0 \\ 0 & 0 & a^2 r^2 d\theta^2 & 0 \\ 0 & 0 & 0 & a^2 r^2 \sin^2\theta d\phi^2 \end{bmatrix} , \tag{3.15}$$

which defines the line element

$$d\tau^2 = -dt^2 + a^2 \left[\frac{1}{1-kr^2} dr^2 + r^2 \left(d\theta^2 + \sin^2\theta d\phi^2 \right) \right] . \tag{3.16}$$

This is the Friedmann-Lemaître-Robertson-Walker (FLRW) metric, a simple metric which describes a homogeneous and isotropic, spherical, pseudospherical, or flat space with time varying cosmic scale factor.

By inserting Eq. (3.15) into Eq. (2.27), one may see that the stress-energy tensor in an FLRW universe takes the form

$$\tau_{\mu\nu} = \begin{bmatrix} \rho & 0 & 0 & 0 \\ 0 & \frac{a^2 p_1}{1-kr^2} & 0 & 0 \\ 0 & 0 & a^2 p_2 r^2 & 0 \\ 0 & 0 & 0 & a^2 p_3 r^2 \sin^2\theta \end{bmatrix} . \tag{3.17}$$

Thus, in an FLRW cosmology, we are treating the Universe as being composed of a homogeneous and isotropic perfect fluid.

3.3 | The Friedmann Equations

Inserting the FLRW metric into the Einstein field equations and taking the time-time component gives us

$$R_{00} - \frac{1}{2} R g_{00} = 8\pi G \rho u_0 u_0 + \Lambda g_{00} , \tag{3.18}$$

where

$$R_{00} = -3\frac{\ddot{a}}{a} , \tag{3.19}$$

$$R = -6 \left[\frac{\ddot{a}}{a} + \left(\frac{\dot{a}}{a} \right)^2 + \frac{1}{k^2 a^2} \right] . \tag{3.20}$$

By inserting Eqs. (3.20) into Eq. (2.27) and defining the Hubble parameter as the expansion parameter for an expanding universe,

$$H \equiv \frac{\dot{a}}{a} \,, \tag{3.21}$$

where the present day value is known as the Hubble constant, H_0, one may derive the Friedmann Equation [34]:

$$H^2 = \frac{8\pi G\rho + \Lambda}{3} - \frac{kc^2}{a^2} \,, \tag{3.22}$$

which describes the expansion of a universe defined by the FLRW metric.

Taking the time derivative of the Friedmann Equation and inserting the definition of $\dot{\rho}$ from Eq. (3.28) gives the acceleration equation,

$$\frac{\ddot{a}}{a} = -\frac{4\pi G}{3}\left(\rho + \frac{3P}{c^2}\right) \,, \tag{3.23}$$

which describes the rate of change of the expansion rate of a homogeneous and isotropic universe.

By defining the total matter, radiation, and Λ density of a flat Universe, which we call the critical density:

$$\rho_{\rm c} = \frac{3H^2}{8\pi G} \,, \tag{3.24}$$

we can define the fractional densities of the constituents of the Universe as the ratio of their respective components' densities to this overall density:

$$\Omega_{\rm m} \equiv \frac{\rho_{\rm m}}{\rho_{\rm c}} \,, \qquad \Omega_{\rm r} \equiv \frac{\rho_{\rm r}}{\rho_{\rm c}} \,, \qquad \Omega_\Lambda \equiv \frac{\rho_\Lambda}{\rho_{\rm u}} \,, \tag{3.25}$$

where $\rho_{\rm m}$ is the density of non-relativistic matter, $\rho_{\rm r}$ is the density of relativistic matter and light, and Ω_Λ is the energy density of the phenomenon modelled by the cosmological constant.

We can generalise this to non-flat Universes by defining the fraction of the Universe's dynamics defined by cosmic curvature:

$$\Omega_{\rm k} \equiv \frac{\rho_{\rm k}}{\rho_{\rm c}} \,, \tag{3.26}$$

where $\rho_{\rm k}$ is the effective energy density modelling the effects of curvature on cosmic dynamics. Given that matter, radiation, the cosmological constant, and curvature are the only

contributors to cosmic dynamics in our standard model of cosmology, we now have that

$$\Omega_{\rm m} + \Omega_{\rm r} + \Omega_{\Lambda} + \Omega_{\rm k} = 1 \ . \tag{3.27}$$

3.3.1 | The Continuity Equation

The conservation equation $\partial_\nu \tau^{\mu\nu} = 0$ encapsulates the notions of conservation of energy and conservation of momentum into one tensor derivative. For an FLRW universe, the $\mu = 0$ component of this takes the form

$$\dot{\rho} + 3H\left(\rho + \frac{p}{c^2}\right) = 0 \ , \tag{3.28}$$

which is the continuity equation for a fluid in an expanding background. Continuity equations in fluid dynamics assert that *the change in fluid density in a given region corresponds to the amount of fluid entering or exiting that region*; an intuitive notion that, when captured in an equation, constitutes one of the starting points of most fluid dynamical derivations. The H term in Eq. (3.28) separates our continuity equation apart from those of most fluids; this term accounts for the change in the density of matter in a given region due to the expansion of the Universe, which will serve as an additional source of pressure acting to disperse all matter. The first H term, $3H\rho$, directly encapsulates the expansion of matter and the ensuing change in density, while the second H term, $3Hp/c^2$, acounts for how this dispersion affects the fluids self-pressure. Thus, our continuity equation for matter in an expanding background can be phrased in English as *the change in density of a fluid in an expanding background at a given time corresponds to the change in density due to the expansion of the background at that time and the change in pressure due to the fluid motion at that time*. Eq. (3.28) can be solved by noting that the equation of state parameter ω is defined such that $p = \omega\rho$, leading to the general solution

$$\rho = \rho_0 a^{-3(1+\omega)} \ . \tag{3.29}$$

Non-relativistic matter has a negligible pressure, such that $\omega = 0$ and $\rho = \rho_0 a^{-3}$. As such, cold matter scales as a^{-3}. Relativistic matter has an equation of state $\omega = 1/3$, such that $\rho = \rho_0 a^{-4}$. The vacuum energy described by the cosmological constant term has $\omega = -1$, such that ρ is a constant in time.

Thus, for ΛCDM cosmology, we can then rewrite Eq. (3.22) as

$$H^2(t) = H_0^2\left[(1 - \Omega_{\rm m} - \Omega_{\rm r} - \Omega_{\rm k})a^{-2} + \Omega_{\rm m} a^{-3} + \Omega_{\rm r} a^{-4} + \Omega_{\Lambda}\right] \ . \tag{3.30}$$

3.3.2 | Cosmic Time Evolution

In this subchapter we will explore a number of hypothetical cosmologies and their dynamics as defined by Eq. (3.30). While each of these cosmologies is an oversimplified idea of cosmic dynamics with only one constituent, they provide useful approximations for eras of the Universe's history in which one component dominated over the others, as will be seen in Chapter 4.

Matter Domination

In a matter dominated universe, defined as being one in which $\Omega_{\mathrm{m}} \approx 1$ and all other density fractions approach zero, Eq. (3.30) becomes

$$H^2 \approx H_0^2 \Omega_{\mathrm{m}} a^{-3} \,, \tag{3.31}$$

where the approximation becomes an equality in the case of a matter only universe, also called an Einstein de-Sitter (EdS) universe, when $\Omega_{\mathrm{m}} = 1$.

In an EdS universe, one may rearrange Eq. (3.31) to see that

$$\dot{a} = \sqrt{H_0^2 a^{-1}} \,, \tag{3.32}$$

which can be solved to give the equation defining the evolution of the EdS scale factor,

$$a = \left(\frac{3}{2} H_0 t \right)^{2/3} \,. \tag{3.33}$$

Thus, in a flat universe containing only non-relativistic matter, we would expect to see the large scale structure of the Universe scale as $a \sim t^{2/3}$.

Radiation Domination

For a radiation dominated universe, defined as being one in which $\Omega_{\mathrm{r}} \approx 1$, Eq. (3.30) becomes

$$H^2 \approx H_0^2 \Omega_{\mathrm{r}} a^{-4} \,. \tag{3.34}$$

In the extremal case of a radiation only universe, in which $\Omega_{\mathrm{r}} = 1$ and all other density fractions vanish, Eq. (3.34) can be rearranged to become

$$\dot{a} = \sqrt{H_0^2 a^{-2}} \,, \tag{3.35}$$

such that

$$a = \sqrt{2H_0 t} \ . \tag{3.36}$$

Inserting Eqs. (3.35) and (3.36) into $H = \dot{a}/a$, we have that

$$H = \frac{1}{2t} \ . \tag{3.37}$$

Thus, in a flat universe containing only relativistic matter and light, the overall distribution of large scale structure would be expected to scale as $t^{1/2}$ and the normalised rate of cosmic expansion will decrease linearly with time.

Λ Domination

For a cosmological constant dominated universe, in which $\Omega_\Lambda \approx 1$, Eq. (3.30) becomes

$$H^2 \approx H_0^2 \Omega_\Lambda \ , \tag{3.38}$$

A universe with only the cosmological constant and no curvature or matter, such that $\Omega_\Lambda = 1$ and all other density fractions vanish, is known as a de-Sitter universe. In such a universe, Eq. (3.38) becomes

$$\dot{a} = \sqrt{H_0^2 a^2} \ , \tag{3.39}$$

which can be solved to see that

$$a \propto e^{H_0 t} \ . \tag{3.40}$$

Thus, in a flat universe dynamically described only by a cosmological constant, the scale factor of the universe would be expected to exponentially increase. Of course, in such a universe there would be no large scale structure as there would be no matter or radiation with which to form it; however, Eq. (3.40) can be used as an approximate solution of the Friedmann Equation for more realistic cosmologies in which a cosmological constant dominates dynamics in a universe which also contains matter and radiation. Furthermore, as will be discussed in Chapter 4, a conjectured period of exponential expansion early in the Universe's history can be approximately described by de-Sitter cosmology, allow us to make predictions regarding its observable effects.

3.4 | Summary

We have discussed cosmological homogeneity and isotropy and have derived the FLRW metric, the most generic metric with which one may describe such universes. From the

FLRW metric we have derived the Friedmann equations and solved them for a number of hypothetical cosmologies. While none of these cosmologies perfectly describes our own universe, as each relies upon the notion that the universe under study contains only one dynamical element while our universe has always been affected by many, we may use the solutions to give ourselves an understanding of how we might expect our universe to scale as it transitions from being dominated by one component to being dominated by another. We will discuss in Chapters 4 and 7 the way in which this constituent-dependent evolution of the scale factor plays a role in defining our currently observable universe.

4

An Inhomogeneous Universe

In this chapter we will briefly review cosmological inflation and how it leads to Hawking radiation which forms the basis of cosmic inhomogeneities. We will then discuss the process of structure formation that causes cosmic inhomogeneities to self-reinforce until they form the basis of the modern observable matter structure of the Universe. Finally, we relate our theoretical work to observations by discussing past, present, and near future LSS surveys and how their analyses may impact our understanding of fundamental physics.

4.1 | Inflation

Broadly, the term *inflation* can be taken to refer to any period in which the scale factor of the Universe is accelerating, $\ddot{a} > 0$. Specifically, it is used to refer to a conjectured period of exponential expansion that brought the Universe from the quantum gravity era to the eras of matter and radiation as we know them now. The expansion of the Universe could also be considered to be a contraction of the Hubble length; as the Universe accelerates, the distance light can travel in a given time decreases, such that the obervable Universe at any point actually becomes smaller.

Inflation was originally proposed by Guth in 1981 [35] as a solution to the problem of unobserved magnetic monopoles; the lack of evidence for such relic particles was inconsistent with the belief that they would have been created early in the Universe's history. By introducing a period of exponential expansion which occurs after their creation but before the limits of our observations, the theory would predict that they became so widely separated by this expansion that the lack of observations would be expected. Guth's original proposal was that the vacuum underwent a first order phase transition, with the bubbles of the new vacuum state expanding at the speed of light. However, this model struggled to adequately incorporate reheating, the creation of modern matter and radiation, as the decay from the

higher energy vacuum state to what we now call matter and radiation could only happen at bubble collision sites, which were predicted to be too rare to explain the observed abundance of matter.

In 1982, Linde [36] and Albrecht and Steinhardt [37] independently solved this problem by instead proposing that the early period of exponential expansion was caused not by bubble nucleation but by the presence of a scalar field, known hereafter as the inflaton field, slowly rolling down its potential*. This model of inflation which is still used today solves not only the monopole problem, but also the horizon, flatness, and structure formation problems.

The horizon problem states that the fact that the Universe is approximately homogeneous and isotropic on scales larger than the causal horizon indicates superluminal transport of information; this is not a problem in inflationary models, as the horizon would have become significantly smaller during inflation, allowing previously causally connected regions to become causally disconnected.

The flatness problem asserts that the near perfect flatness of the Universe requires unjustified fine tuning; in inflationary models, any curvature is expanded to such an extent that it will resemble flat space on cosmological horizon scales.

The structure formation problem points out that the origin of cosmic structure, of galaxies and halos and their formations, cannot be explained without new physics in the early universe to create the inhomogeneities they must have originated from; inflation provides this new physics, as will be described below.

4.1.1 | Slow Roll Inflation

In the early universe, the cosmological constant made a negligable contribution to the cosmic density, such that we can set $\Lambda = 0$ and obtain from Eq. (3.23) that during inflation

$$\rho + 3p < 0 \, . \tag{4.1}$$

Note that this requires either the density or pressure to be negative; generally, due to the exotic nature of negative densities†, it is assumed that $\rho > 0$ and $p < 0$. Scalar fields exibit

*At the time of the writing of this thesis, numerous inflationary and alternative models exist, many incorporating multiple interacting inflaton fields, with single field, slow roll inflation being the simplest model which is consistent with observations; for the remainder of this chapter, we treat inflation as being caused by a single, slow rolling field, though the results we obtain regarding the creation of inhomogeneities are equally applicable to other forms of inflation. In the event that an alternative model predicted alterations in the formation of these inhomogeneities, the differences would be observable in near future survey data by studying present day structure and thereby inferring the precise distribution and nature of primordial inhomogeneities.

†Some theories predict the existence of fluids with negative energy densities and they are seen as necessary for the existence of certain spacetimes; however, no experimental or observational evidence exists to indicate

negative pressure, such that Eq. (4.1) provides another reason for us to consider scalar field driven inflation.

Remembering Eqs. (2.31) and (2.32), the momentum and pressure of a spatially homogeneous scalar field ϕ with potential $V(\phi)$ on an FLRW background are given by

$$\rho = \frac{1}{2}\dot{\phi}^2 + V(\phi) \ , \quad p = \frac{1}{2}\dot{\phi}^2 - V(\phi) \ , \tag{4.2}$$

from which we can see that the pressure will be negative when $\dot{\phi}^2 < 2V(\phi)$.

In the case of the inflaton, the potential is unknown and is usually left as a free function determined by whichever inflationary model is chosen. From these, we can see from the Friedmann and continuity equations that

$$H^2 = \frac{1}{3}\left[\frac{1}{2}\dot{\phi}^2 + V(\phi)\right] \ , \quad \ddot{\phi} + 3H\dot{\phi} = -\frac{dV}{d\phi} \ . \tag{4.3}$$

Defining the slow roll parameters

$$\varepsilon(\phi) = \frac{1}{2}\left(\frac{V'(\phi)}{V(\phi)}\right)^2 , \quad \mu(\phi) = \frac{V''(\phi)}{V(\phi)} \ , \tag{4.4}$$

we can see that if the conditions $\varepsilon(\phi) \ll 0$ and $\mu(\phi) \ll 0$ are met, such that the potential remains approximately unchanged as the scalar field itself changes in value, then we have that

$$H^2 \approx \frac{1}{3}V(\phi) \ , \quad 3H\dot{\phi} \approx -V'(\phi) \ . \tag{4.5}$$

An inflaton field which obeys these conditions will lead to slow roll inflation. Inflation ends with reheating, when the inflaton field decays into the particles we see around us today.

4.1.2 | The Origin of Inhomogeneities

Due to the rate of expansion during inflation, an event horizon forms, allowing pair production to result in Hawking radiation [38]. This exchange of energy to the created particles results in fluctuations in the energy density of the inflaton field, which ultimately become the inhomogeneities in the particle field formed during reheating.

In order to have caused the effects we observe, inflation must have lasted long enough for the scale factor to expand by at least 10^{26} times. Such a period can be approximately described by a de-Sitter cosmology, which, as was discussed in Chapter 3.3.2, describes

that any such fluids exist or that any real regions of space correspond to such spacetimes, such that many consider them to be undesirable exotic particles which should only be treated when absolutely necessary.

a universe that is eternally dominated by a cosmological constant. In a de-Sitter universe, there is no meaningful definition of time or scale beyond those that can be defined by the horizon scale at any given time, c/H, as in a period of indefinite exponential expansion, there will have been no beginning or end but only expansion. Thus, these fluctuations will be predicted to be scale invariant; in other words, inhomogeneities will be expected to follow the same statistical distribution on all scales. Furthermore, they would be expected to have a magnitude of roughly $\delta\phi \sim H$.

The fluctuations cause the inflaton field to begin decaying into a matter field at slightly different times at different places, with those areas that have lost energy to fluctuations undergoing reheating sooner than other regions with $\delta t \sim \delta\phi/\dot{\phi}$.

The inhomogeneities in the particle field after reheating will take the form of regions of over and underdensity in the resulting matter and radiation distributions. Over the span of billions of years, even the slightest overdensity could gravitationally attract surrounding matter and find itself amplified into a significantly overdense region of the universe. This is believed to be the process by which matter began to coalesce into dark matter halos and baryonic galaxies; this is the story of structure formation.

Of course, inflation does not last eternally and is not a true de-Sitter universe, but for its duration the horizon scale is the only meaningful scale with which to compare distances, aside from the scale of the initial, pre-inflationary universe, which will be so small as to have no meaningful effect on the distribution of fluctuations. Furthermore, there will be differences between the fluctuations generated towards the end of inflation which result in immediate density perturbations during reheating and those that occurred earlier and have been pushed beyond the horizon by that time, which will be able to re-enter the horizon once inflation has stopped. This leads to effects which alter the distribution of fluctuations and their remnants from what would be expected in a truly scale invariant universe, as will be discussed in Chapter 4.4.2.

4.2 | The Cosmic Microwave Background

Prior to the mid-1960s, the majority of our information regarding cosmological structure and its evolution came from observations of the redshifts and distances of individual galaxies. In 1964, by serendipitous accident, Bell Labs radio astronomers Arno Penzias and Robert Wilson discovered the CMB. Since then, it has become the most important observational probe of inflation and structure formation [39, 40] prior to the 2010s, during which direct studies of the contemporary large scale structure of the Universe became capable of competing with and overtaking them in information content.

The CMB originated as much higher frequency light in the early universe. Shortly after reheating, the energy density of the Universe was high enough that baryonic matter was coupled strongly to photons; electrons and protons were constantly colliding to form atoms only to collide with ionising light or other charged particles, returning them to their ionised states, all the while photons were scattering from every charged particle they came across. As the Universe continued expanding, the energy density of the matter within decreased until neutral atoms were able to form and remain stable. These atoms did not scatter light as their free, charged constituents had done, causing the light that had previously been being scattered to begin shining freely across the cosmos; this is referred to as the decoupling of light from baryonic matter. The plasma the light decoupled from would have formed a blackbody, such that the light was consistent with a blackbody's radiation spectrum. This light is still visible today, having been redshifted to the microwave band of radiowaves, where its frequency modes still make up a spectrum the shape of a cold blackbody's radiation, and makes up the CMB.

The density of photons in the CMB is a function of both the baryonic density field at the time of decoupling and of gravitational lensing and scattering which has affected the light between the time of decoupling and the time of observation[‡]. Studying the observable CMB map can not only be used to learn about the inflaton field itself, but also gives us a map of the structure of the Universe as it was at the time of decoupling, allowing us to model the evolution of structure using known gravitational equations from an observed initial state.

The CMB is visible from all parts of the Universe, though the precise image one would see when mapping the CMB across the sky will vary from location to location; of course, with present technology, we are limited to observing only the CMB map that is visible from Earth. Throughout this thesis we use data taken from the Wilkinson Microwave Anisotropy Probe (WMAP) to generate the seeds of our structure formation simulations and to calibrate our model by noting that we have a $\Omega_{\mathrm{m},0} = 0.272$, $\sigma_8 = 0.81$, $n_{\mathrm{s}} = 0.967$ cosmology with $h = 0.724$. It should be noted that a more recent study by the Planck collaboration [41] has estimated that these parameters are $\Omega_{\mathrm{m},0} = 0.315$, $\sigma_8 = 0.811$, $n_{\mathrm{s}} = 0..965$ and that the precise value of h is subject to controversy at the present time; however, any such corrections are minor and are minimised once the error bars of the respective studies are taken into account.

[‡]With the formation of the first stars and other radiation emitting objects after recombination, the radiation they emitted led to the matter of the Universe becoming once again predominantly ionised; the era in which this transition occurred is known as the Epoch of Reionisation. As the scale factor had expanded significantly between decoupling and reionisation, the energy density of the Universe had decreased such that the CMB has not been able to couple to ionised matter as it did before, but scattering between CMB photons and modern ionised matter can still lead to detectable alterations in the CMB map that must be accounted for in order to reconstruct an accurate image of the primordial density field.

4.3 | The Formation of Structure

LSS, the large scale distribution of matter across the Universe, promises to be the next major observable probe of fundamental physics. Its three dimensional nature offers orders of magnitude more observables than the two dimensional CMB and the fact that it is directly observable as far back as the Epoch of Reionisation makes it possible to place significantly more precise constraints on late time parameters.

The origin of LSS lies with the same inflationary perturbations which resulted in the inhomogeneities in the CMB. Over the billions of years since decoupling, these small perturbations expanded with time to become the galaxies and dark matter halos around the Universe today. The temperature fluctuations in the CMB are of the order

$$\frac{\delta T}{T} \approx 10^{-5} \,, \tag{4.6}$$

resulting in a primarily homogeneous surface with only minor perturbations, while the matter density of galaxies in contrast to that of the Universe overall is

$$\frac{\rho_{\text{galactic}}}{\rho_{\text{cosmic}}} \approx 10^{6} \,, \tag{4.7}$$

displaying a significantly less homogeneous surface on all but the largest scales. This $\mathcal{O}(10^{11})$ magnification of matter density perturbations is the result of gravitational attraction and collapse, a well developed model of which will be necessary if present and near future LSS survey data is to be used to its full potential. The remainder of this thesis concerns itself with the modelling of structure formation through fluid dynamical equations in order to try to further develop just such a model, the EFTofLSS.

4.3.1 | Gravitational Fluid Dynamics

We wish to model the density and velocity fields of cold dark matter particles in a given background cosmology. Because dark matter particles only interact gravitationally and, potentially, via the weak interaction, they are incapable of collisions, which describe repulsive electromagnetic interactions. Viscocity and heat transfer are emergent phenomenon from electromagnetic interactions, resulting from electromagntic interactions between particles and both such interactions and the emission of light, respectively, so dark matter can be treated as having no viscocity or heat properties. Thus, we can model cold dark matter as a collisionless, perfect fluid.

Fluid equations are only valid on scales larger than the mean free path of a constituent particle. For dark matter, the mean free path integrated over all of time is infinite, but we can define a limitation on the mean free path at any given redshift by noting that we are treating cold dark matter, which moves at non-relativistic speeds, and that at any given redshift it has only had a finite amount of time to travel since reheating. This gives an effective mean free path at redshift z of $vH(z)^{-1} \sim 1/k_{\rm n}$, where $k_{\rm n}$ is what we call the non-linear scale for reasons that will become apparent throughout this chapter and the next and which constitutes a small enough scale that we can consider our fluid description to work as a description of LSS but not of smaller scale structures such as individual galaxies.

A single particle can be described in real and momentum space by the phase space density

$$f^i(x^j, p^j, \eta) = \delta^{(\rm D)}(x^j - x^i)\delta^{(\rm D)}(p^j - mav^i) \tag{4.8}$$

at comoving time $\eta = t/a$[§], where p^j is the canonical momentum of the particle in the system, such that $\int f^i(x^j, p^j, \eta) d^3x^j d^3p^j$ gives the probability of finding the particle in volume $d^3x^j d^3p^j$ at comoving time η. In a system of multiple interacting particles, each particle individually obeys the collisionless Boltzmann equation

$$\frac{{\rm D}f}{{\rm D}t} = \frac{\partial f_a}{\partial t} + \frac{p_a^i}{ma^2} \cdot \frac{\partial f_a}{\partial x_a^i} - \sum_{b \neq a} m \frac{\partial \phi_b}{\partial x_a^i} \cdot \frac{\partial f}{\partial p_a^i} = 0 \,, \tag{4.9}$$

where ϕ_a is the gravitational potential of the particle with phase space density $f_a(x^j, p^j)$ and density $\rho(x^j)$. It is important to note that this is the Newtonian potential; relativistic effects dominate descriptions of gravity on very large cosmological scales through cosmic curvature and on very small astrophysical scales through small scale curvature, but these are usually taken to be negligible on the scales of interest for LSS studies, those generally ranging from $\mathscr{O}(1\text{Mpc})$ to $\mathscr{O}(100\text{Mpc})$. The Boltzmann equation makes the statement *the probabilty of finding the particle anywhere with any momentum within the closed system does not change*, such that it is effectively the continuity equation for quantised, stochastically distributed particles. The first term in the expanded total derivative describes the evolution of the probability distribution in time; the second term describes the particles motion at a given moment, while the third term describes the gravitational effects of the other particles in the system on the particles motion at that time; together, they assert that *each particle is in a closed system and gravitationally attracted to every other particle; as such, the evolution of the probability of finding the particle in a particular location with a particular motion is*

[§]The comoving time provides a measure of the time taken to travel at a given velocity between two fixed points which remains constant as the background and, by extension, the absolute distance between those points expands.

given by its existing motion and location, taking into account cosmic expansion and the sum of its attractions to all other particles.

The models of cosmological dynamics explored in this thesis are based on an ensemble of N collisionless point particles [7] whose overall phase space density is given by

$$f(x^i, p^i, \eta) = \sum_{j=1}^{N} f_j(x^i, p^i) \ . \tag{4.10}$$

Treating the system as a whole through this overall phase space density rather than focusing on individual particles, the collisionless Boltzmann equation for such an ensemble is

$$\frac{\mathrm{D}f}{\mathrm{D}t} = \frac{\partial f}{\partial t} + \frac{p^i}{ma^2} \cdot \frac{\partial f}{\partial x^i} - m\frac{\partial \phi}{\partial x^i} \cdot \frac{\partial f}{\partial p^i} = 0 \ . \tag{4.11}$$

We are interested primarily in solving Eq. (4.11) for the real space distribution of the system as a function of time, rather than in solving for the full phase space function. As such, we may take the momentum moments of the Boltzmann equation to obtain important functions of real space. Taking the first three moments of Eq. (4.11) gives us definitions for the matter and momentum densities,

$$\rho(x^l, \eta) = \frac{m}{a^3} \int d^3p^l \ f(x^l, p^l, \eta) \ , \tag{4.12}$$

$$\pi^i(x^l, \eta) = \frac{1}{a^4} \int d^3p^l \ p^i \ f(x^l, p^l, \eta) \ , \tag{4.13}$$

and

$$\sigma^{ij}(x^l, \eta) + \tau^{ij}(x^l, \eta) = \frac{1}{ma^5} \int d^3p^l \ p^i p^j \ f(x^l, p^l, \eta) \ , \tag{4.14}$$

where σ^{ij} is the kinetic tensor and τ^{ij} is the stress-energy tensor, defined such that the stress-energy tensor contains terms multiplied by free parameters which are explored in more detail in Chapter 5 and the kinetic tensor encompasses the remaining, deterministic components of this moment.

Now that we have defined fluidic parameters, we might try to redefine our equations of motion to describe fluidic density rather than the less tangible ensemble phase space function. Applying Eqs. (4.12), (4.13), and (4.14) to the Boltzmann equation [42] allows us to obtain the continuity equation[¶]

$$\partial_\eta \rho + 3H\rho + \partial_i(\rho v^i) = 0 \tag{4.15}$$

[¶]We have used that momentum density is the momentum per unit volume such that $\pi^i = v^i \rho$.

and the Euler equation

$$\partial_\eta v^i + H v^i + v^j \partial_j v^i + \partial_i \phi = -\frac{1}{\rho}\partial_j \tau^{ij}. \tag{4.16}$$

Taking the derivative of Eq. (4.16) and defining the velocity divergence field $\theta = \partial_i v^i$, we see that

$$\partial_\eta \theta + H\theta + v^j \partial_j \theta + \partial_i v^j \partial_j v^i + \partial_i \partial^i \phi = -\frac{1}{\rho}\partial_i \partial_j \tau^{ij} \ . \tag{4.17}$$

The equations of motion derived above work for any gravitating, otherwise forceless set of particles on scales larger than their free streaming distance. We wish to develop a model that specifically describes inhomogeneities in the density field, such that we can describe the distribution of regions of overdensity throughout the Universe. We begin by defining the density contrast

$$\delta(x^i, \eta) \equiv \frac{\rho(x^i, \eta) - \bar{\rho}(\eta)}{\bar{\rho}(x^i, \eta)} \ , \tag{4.18}$$

where $\bar{\rho}$ is the mean of the overall field, such that the density field is given by

$$\rho(k^i, \eta) = \bar{\rho}(k^i, \eta)(1 + \delta(k^i, \eta)) \ . \tag{4.19}$$

Transforming Eqs. (4.15) and (4.17) into Fourier space, inserting Eq. (4.19), and subtracting the background terms gives us the continuity and Euler equations for cosmological inhomogeneities:

$$\partial_\eta \delta(k^i, \eta) + \theta(k^i, \eta) = S_\alpha(k^i, \eta) \ , \tag{4.20}$$

$$\partial_\eta \theta(k^i, \eta) + H\theta(k^i, \eta) + \frac{3}{2}\Omega_{\rm m} H^2 \delta(k^i, \eta) = S_\beta(k^i, \eta) \ , \tag{4.21}$$

where the source terms S_α and S_β are convolutions describing the coupling between fields and are defined as

$$S_\alpha(k^i, \eta) = -\int \frac{{\rm d}^3 q^i}{(2\pi)^3} \alpha(q^i, k^i - q^i)\theta(q^i, \eta)\delta(k^i - q^i, \eta) \ , \tag{4.22}$$

$$S_\beta(k^i, \eta) = -\int \frac{{\rm d}^3 q^i}{(2\pi)^3} \beta(q^i, k^i - q^i)\theta(q^i, \eta)\theta(k^i - q^i, \eta) + \frac{1}{\rho}\partial_i \partial_j \tau^{ij} \ , \tag{4.23}$$

where the kernels α and β are

$$\alpha(k_1^i, k_2^i) = \frac{k_1^j (k_{1j} + k_{2j})}{k_1^2} \tag{4.24}$$

and

$$\beta(k_1^i, k_2^i) = \frac{1}{2}(k_1^i + k_2^i)^2 \frac{k_1^j k_{2j}}{k_1^2 k_2^2} \,. \tag{4.25}$$

4.3.2 | Linear Inhomogeneities

Eqs. (4.20) and (4.21) are two of the foundational equations for studies of cosmological large scale structure; by solving for δ and θ, we can estimate the distributions of density and velocity inhomogeneities across the Universe for various cosmological models and compare them to observations. This is the reason for developing analytic models of LSS; by comparing the predicted fields from various cosmological models that are currently considered potentially accurate descriptions of our Universe to observations, we can rule out a significant fraction of the parameter space of such models. Ultimately, this serves the aim of allowing us to develop the ability to precisely and confidently understand the past and predict the future of the Universe and its constituents. However, they are non-linear differential equations that permit no exact solution. As such, we cannot construct an exact analytic function to describe the evolution of density inhomogeneities across time. Instead, we must rely upon approximate solutions which are valid only on certain scales even within the confines of the fluid description; in this subchapter we will explore the largest scale approximation, the solution to the linearised forms of these equations, and its cosmological implications.

Noting that on large scales, $\delta(k^i, \eta) \ll 1$ and $\theta \ll 1$, such that any terms featuring higher power of δ and v^i will be highly subleading, we can approximate a full solution to Eqs. (4.20) and (4.21) with solutions to their linearised forms. These can be obtained by setting the source terms to zero as they contain all of the equations' higher powers in the density and velocity divergence fields, and we define the solutions to these linear equations as $\delta_1(k^i, \eta)$ and $\theta_1(k^i, \eta)$ to differentiate them from the fully non-linear solutions we are hoping to approximate:

$$\partial_\eta \delta_1 + \theta_1 = 0 \,, \tag{4.26}$$

and the Euler equation becomes

$$\partial_\eta v_1^i + H v_1^i = -\partial_i \phi^j \,. \tag{4.27}$$

The velocity field of the dark matter fluid can be described entirely by its vorticity, $w_1^i = \varepsilon^{ijk} \partial_j v_{1k}$, and divergence field, θ_1, the equations of motion for which follow from

Eq. (4.27):

$$\partial_\eta \theta_1 + H\theta_1 + \frac{3}{2}\Omega_\mathrm{m} H^2 \delta_1 = 0 \,, \tag{4.28}$$

$$\partial_\eta w_1^i + H w_1^i = 0 \,. \tag{4.29}$$

Eq. (4.29) can be solved to see that $w_1^i \sim a^{-1}$, such that any cosmic vorticity will be damped with time; indeed, observations have shown there to be negligible non-linear vorticity on large scales, such that for the duration of this thesis we set $w^i = 0$ regardless of linearity.

Noting the definition of θ_1 in terms of δ_1 from Eq. (4.26) and taking the time derivative of Eq. (4.28) gives us

$$\partial_\eta^2 \delta_1 + H\partial_\eta \delta_1 = -\frac{3}{2}\Omega_\mathrm{m} H^2 \delta_1 \,. \tag{4.30}$$

This is the equation of motion for the linear density inhomogeneity field and can be solved to give us estimations of cosmic evolution on large scales as functions of the density fraction parameters defined in Chapter 3.

4.3.3 | Time Evolution of Linear Inhomogeneities

By splitting $\delta_1(k^i, \eta)$ into its time dependent and independent components,

$$\delta_1(k^i, \eta) = D_1(\eta)\delta_1(k^i) \,, \tag{4.31}$$

we can obtain from Eq. (4.30) the evolution equation for the growth factor of linear perturbations:

$$\partial_\eta^2 D_1 + H\partial_\eta D_1 = -\frac{3}{2}\Omega_\mathrm{m} H^2 D_1 \,. \tag{4.32}$$

As this is a second order differential equation, we know that there must be two solutions and define

$$\delta_1(k^i, \eta) = D_{1\mathrm{A}}(\eta)A(k^i) + D_{1\mathrm{B}}(\eta)B(k^i) \,. \tag{4.33}$$

for time independent functions $A(k^i)$ and $B(k^i)$.

Matter Domination

Taking the example of an EdS universe, we set $\Omega_\mathrm{m} = 1$ and, remembering Eq. (3.24), we see that

$$4\pi\rho \approx \frac{3}{2}H^2 \,. \tag{4.34}$$

Taking the time derivative of Eq. (3.33), we see that

$$H^2 = \frac{4}{9}t^{-2} \,, \tag{4.35}$$

such that Eq. (4.34) becomes

$$4\pi\rho = \frac{2}{3}t^{-2} \,. \tag{4.36}$$

Inserting this into the right hand side of Eq. (4.32), we now have

$$\partial_\eta^2 D_1 + 2H\partial_\eta D_1 = \frac{2}{3}t^{-2}D_1 \,. \tag{4.37}$$

We can solve Eq. (4.37) with a power law solution such that

$$D_1 \propto t^{2/3} + t^{-1} \,, \tag{4.38}$$

where we refer to the first and second components of the right hand side as the growing and decaying modes, respectively.

Remembering that in a matter dominated universe, $a \propto t^{2/3}$, the growing mode indicates that EdS density perturbations would grow linearly with the expansion of the universe.

Radiation Domination

Thus far, when treating cosmologies dominated a particular component, we have treated them as being entirely composed of that component and have disregarded other sources of gravitation. Of course, even in an epoch dominated by radiation, dark and baryonic matter will exist, though their effects on cosmology will be subleading. Nonetheless, in this subchapter we will explore the behaviour of dark matter in a radiation dominated epoch, which requires a generalisation of Eq. (4.30) to multiple component cosmologies. This can be found by simply defining a system of equation

$$\partial_\eta^2 \delta_{1,i} + 2H\partial_\eta \delta_{1,i} = 4\pi\bar{\rho}\sum_j \Omega_j \delta_{1,j} + \frac{1}{a}\frac{dp}{d\rho}\partial^2\delta_{1,i} \,, \tag{4.39}$$

where the index i labels a given source of gravity and the sum over j introduces the gravitational effects of all components on to each of them.

In the case of a Universe modelled as containing only dark matter, labeled with index m, and radiation labeled with index r, we have

$$\partial_\eta^2 \delta_{1,\mathrm{m}} + 2H\partial_\eta \delta_{1,\mathrm{m}} = 4\pi\bar{\rho}\left(\Omega_\mathrm{m}\delta_{1,\mathrm{m}} + \Omega_\mathrm{r}\delta_{1,\mathrm{r}}\right) + \frac{1}{a}\frac{dp}{d\rho}\partial^2\delta_{1,\mathrm{m}} \,. \tag{4.40}$$

In a radiation dominated epoch, $\rho_{\rm r} \gg \rho_{\rm m}$ such that $\Omega_{\rm m} \ll 1$, and $\Omega_{\rm r} \approx 1$, and $H \sim t^{-1}$, as shown in Chapter 3.3.2. Furthermore, the radiation background is significantly less inhomogeneous than the matter fields, such that $\delta_{1,{\rm r}} \approx 0$, such that Eq. (4.32) becomes

$$\partial_\eta^2 D_{1,{\rm m}} + \frac{1}{t}\partial_\eta D_{1,{\rm m}} = 0 \, . \tag{4.41}$$

This can be solved by the generic solution

$$D_{1,{\rm m}} = x + y\ln(t) \tag{4.42}$$

for constants x and y.

The dark matter perturbation given by Eq. (4.42) will scale logarithmically with time, such that even when $\lambda > \lambda_{\rm J}$, the evolution of gravitational collapse will be extremely slow. Thus, in a radiation dominated universe, the growth of density inhomogeneities is damped and they must wait until matter domination before they are able to grow at a rapid rate.

This damping of density inhomogeneity evolution during radiation domination is known as the Mészáros effect and is the result of radiation expanding the universe at such a rate that non-relativistic matter is unable to collapse, the self-gravity of matter being insufficient to overcome the radiation pressure pushing it to expand.

Λ Domination

In a universe containing both a Λ term and matter, the first solution may be found to be [43]

$$D_{1{\rm B}} = H \, . \tag{4.43}$$

To find the remaining solution, we may use the integral representation of the linear growth factor [43, 44]

$$D_1 = H\frac{5}{2}\Omega_{\rm m}\int_0^a \frac{da}{a^3 H} \, , \tag{4.44}$$

where we can see from Eq. (3.30) that $H = \sqrt{\Omega_{\rm m}a^{-3} + (1-\Omega_{\rm m}-\Omega_\Lambda)a^{-2} + \Omega_\Lambda}$.

It is not generally possible to solve Eq. (4.44) analytically, but solutions can be approximated as [44]

$$D_{1{\rm A}} \approx \frac{5}{2}\frac{a\Omega_{\rm m}}{\Omega_{\rm m}^{4/7} - \Omega_\Lambda + \left(1+\frac{\Omega_{\rm m}}{2}\right)\left(1+\frac{\Omega_\Lambda}{70}\right)} \, . \tag{4.45}$$

4.4 | Correlation Functions

LSS is a large distribution driven by stochastic processes; as such, the most efficient way to analyse the data it can provide us is not by mapping every object exactly and trying to replicate the distribution in theory but by trying to equate observed and theoretical statistics. These take the form of correlation functions [5, 6, 45, 46]; a correlation function is a statistical measure of the distribution of inhomogeneities formed from the convolution of two density inhomogeneity field values at chosen coordinates.

Correlators can be studied between any observables but are most commonly measured for galaxy distributions, which can be theoretically predicted by analytically describing the distribution of dark matter inhomogeneities as will be described in Chapter 5 and accounting for the statistical differences between galaxy and dark matter distributions. Most commonly studied are the Fourier transforms of the two, three, and four point correlation functions: respectively, the power spectrum,

$$\langle \delta_{\mathrm{A}}(k_1^i)\delta_{\mathrm{B}}(k_2^i)\rangle = (2\pi)^3\delta^{(\mathrm{D})}(k_1^i+k_2^i)P_{\mathrm{AB}}(k_1)\ , \tag{4.46}$$

bispectrum,

$$\langle \delta_{\mathrm{A}}(k_1^i)\delta_{\mathrm{B}}(k_2^i)\delta_{\mathrm{C}}(k_3^i)\rangle = (2\pi)^3\delta^{(\mathrm{D})}(k_1^i+k_2^i+k_3^i)B_{\mathrm{ABC}}(k_1,k_2,k_3)\ , \tag{4.47}$$

and trispectrum,

$$\langle \delta_{\mathrm{A}}(k_1^i)\delta_{\mathrm{B}}(k_2^i)\delta_{\mathrm{C}}(k_3^i)\delta_{\mathrm{D}}(k_4^i)\rangle = (2\pi)^3\delta^{(\mathrm{D})}(k_1^i+k_2^i+k_3^i+k_4^i)T_{\mathrm{ABCD}}(k_1^i,k_2^i,k_3^i,k_4^i)\ . \tag{4.48}$$

Note that the power spectrum is a function of only one parameter, the momentum magnitude k; this is because there is only one momentum separating the two points and, due to the isotropy and homogeneity of the Universe, the orientation of these points relative to the observer is irrelevant. The bispectrum is dependent upon three parameters, given above as the magnitudes of the three wavevectors connecting the three points although alternative parametrisations are possible, as these points fully specify the positions of the points relative to one another and, once again, the isotropy and homogeneity of the Universe renders the resulting triangle's orientation with respect to Earth irrelevant. The trispectrum is a function of six variables, given above as four full wavevectors connecting the four points, as the shape connecting the four points is a tetrahedron whose orientation, as before, is irrelevant due to isotropy and homogeneity.

The space of possible shapes a correlator can take in real or momentum space is called its configuration space. Ordinarily, we study correlators in momentum space with the magnitudes of their vectors chosen in bins ranging from a chosen $k_{\rm min}$ to a chosen $k_{\rm max}$, thus defining the shells in which we perform measurements. The power spectrum is the correlator of two fields and so takes the form of a single line which can be entirely defined by its magnitude, k. Thus, it has a one dimensional configuration space which is numerically simple to study in full. The bispectrum is the correlator of three fields and so takes the form of a triangle, with each density field represented by a vector. By convention, we refer to the vector defining the first density field as k_1^i, that defining the second density field as k_2^i, and that defining the third density field as k_3^i. We can entirely define the configuration of a bispectrum using three parameters; if we take the magnitudes of k_1^i and k_2^i together with the enclosed angle ϕ, we can calculate k_3^i from the requirement that these two vectors are connected into a closed triangle. Alternatively, we could take the magnitudes of all three vectors and calculate ϕ using basic trigonometry. Thus, the bispectrum has a three dimensional configuration space. The momentum space shapes of the power spectrum and bispectrum are shown in Fig. 4.1.

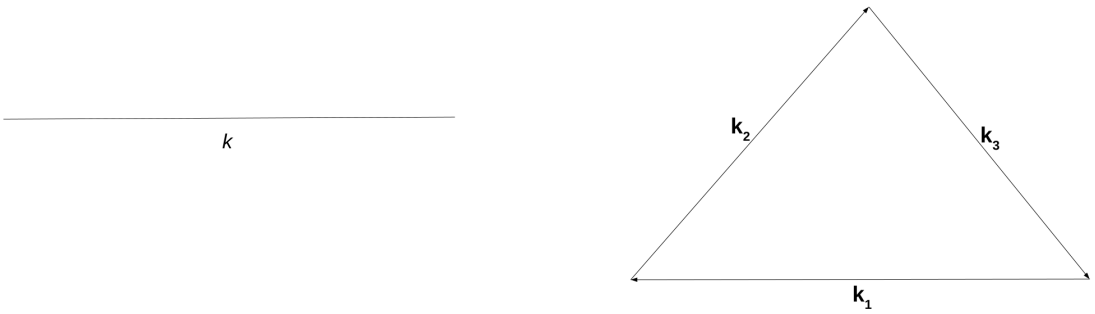

Figure 4.1: *Left:* The shape of the power spectrum in momentum space: As we are only connecting two points in a homogeneous and isotropic space, we can entirely define the power spectrum with one parameter: the momentum, k. *Right:* The shape of the bispectrum in momentum space. It can be entirely defined by three parameters; either the magnitudes of two vectors and the angle that separates them, or the magnitudes of all three vectors. The requirement that the vectors connect to form a closed triangle allows us to deduce the remaining parameters defining all three vectors from basic trigonometry.

The trispectrum is the correlator of four fields and so takes the shape of a tetrahedron, as shown in Fig. 4.2. This shape has six momentum vectors defining the four fields; four of them we label the external legs and the remaining two we call diagonal legs. When we come to studying individual configurations, we will see that this distinction allows us to define trispectra by their external legs while averaging over their diagonals.

We can parametrise the trispectrum as

$$k_1^i = (k_1, 0, 0) \,, \tag{4.49}$$

$$k_2^i = k_2 \left(\sqrt{1-\mu_1^2}, 0, \mu_1 \right) \,, \tag{4.50}$$

$$k_3^i = k_3 \left(\sqrt{1-\mu_2^2}\cos(\phi_2), \sqrt{1-\mu_2^2}\sin(\phi_2), \mu_2 \right) \,, \tag{4.51}$$

$$k_4^i = -k_1^i - k_2^i - k_3^i \,, \tag{4.52}$$

$$k_5^i = k_1^i + k_2^i \,, \tag{4.53}$$

$$k_6^i = k_2^i + k_3^i \,, \tag{4.54}$$

with k_5^i and k_6^i being referred to hereafter as the diagonal legs. The choice of these two as the diagonal legs is arbitrary, with the only requirement being that the external legs form a closed quadrilateral. With three legs defined, the remaining three can be inferred from the requirement that every point be connected to every other in a closed tetrahedron; thus, we can define a configuration fully with six scalar parameters; those are usually chosen to be either the magnitude of three vectors and the three angles that separate them from one another in 3D space, $(k_1, k_2, k_3, \mu_1, \mu_2, \phi_2)$, or the magnitudes of all six legs, $(k_1, k_2, k_3, k_4, k_5, k_6)$. The shape of the trispectrum in momentum space is shown in Fig. 4.2.

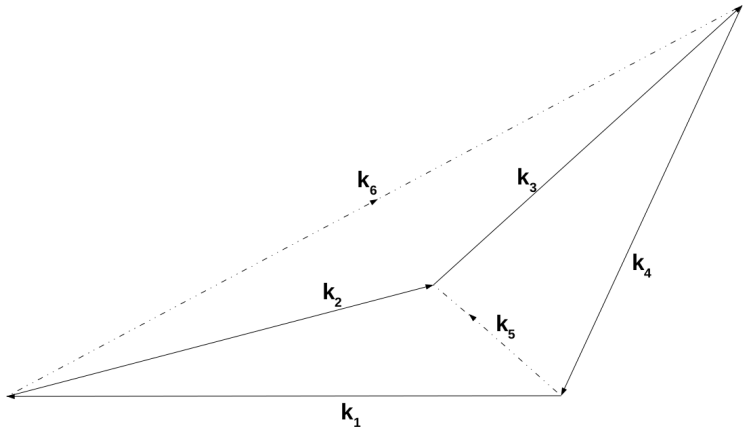

Figure 4.2: The shape of the trispectrum in momentum space. The four density field points are connected by six legs to form a tetrahedron; by convention, we refer to four of those legs as the external legs, shown by solid lines, and two as diagonal legs, shown by dotted lines.

Higher order correlators are more prone to systematic errors than lower order correlators; as such, the power spectrum remains the most commonly used object of study in LSS cosmology. However, the study of higher order correlators such as the bispectrum and trispectrum allows the breaking of degeneracies that may arise when studying only one

observable, potentially allowing constraints to be placed on fundamental physics with much higher precision, should those systematic errors be correctly accounted for.

4.4.1 | Correlator Surveys

Recent and near future surveys of LSS such as Euclid [1], SPHEREx [2], LSST [3] , and SKA [4] promise to allow us to perform parameter constraints with unprecedented precision. They measure the respective positions of millions of galaxies in redshift space, allowing correlation functions which provide a statistical measure of the distribution of galaxies at chosen scales to be measured and compared to those predicted by fundamental theory.

Different surveys often use different methods to probe different regions of the Universe, allowing their results to complement each other rather than be rendered redundant. In this sub-chapter we will briefly discuss a number of upcoming surveys and how their methodologies and results will complement each other to allow a a significant increase to our understanding of cosmological parameters.

The Euclid mission is an optical and infrared satellite telescope based mission that will probe both gravitational lensing and galaxy clustering to an apparent magnitude of approximately 24.5 mag, both of which are valid methods for measuring LSS, using a combination of visual imaging and near-infrared photometry. Euclid will image 1.5 billion galaxies. By correlating the shapes of the galaxies, lensing parameters can be inferred which can be used as a study of the matter field between the observed galaxies and the probe. By further studying the spectroscopic redshifts of 50 million galaxies, they can also calculate the correlators defining the galaxy field. Thus, Euclid will provide a probe of both the matter and galaxy fields to a high level of precision.

The SPHEREx mission is an infrared satellite telescope based mission that will measure the spectroscopic redshifts of over 500 million galaxies out to an apparent magnitude of approximately 18.5 mag. By mapping the redshifts of over ten times as many galaxies as Euclid over a larger redshift range, SPHEREx will provide significantly more information on galaxy clustering, though only in a shallower volume. One of SPHEREx's primary purposes will be to study inflationary effects such as primordial non-Gaussianity; it's datasets are expected to reduce the uncertainty on the magnitude of the bispectrum of primordial non-Gaussianities, f_{NL}, by an order of magnitude.

The LSST mission is a ground optical and infrared telescope based mission that seeks to image roughly 10 billion galaxies out to a depth of approximately 27.5 mag. Most of these galaxies will have too low a brightness for an accurate measurement of their spectroscopic redshift, such that they will primarily be useful for studies of weak lensing. However, the LSST mission also intends to spectroscopically survey a small subset of its observed

galaxies, measuring of the order of 10 thousand spectra, in order to provide information which can be cross-correlated with information from galaxy clustering to provide a significant improvement to the incomplete redshift studies that already exist.

The SKA mission is a ground radio telescope based mission that seeks to provide redshift surveys at higher redshifts than is possible with visible and infrared telescopes. Unlike the other surveys listed above, SKA has a broad mission scope and can be tailored to provide data for different physical questions; this is due to the fact that the array itself is a dispersed set of radio telescopes, rather than a single lensed telescope as is the case in LSST, SPHEREx, and Euclid, allowing for various configurations.

As each survey studies a different volume of the sky in varying wavelengths, the multiple datasets they will provide may be used to cross-check results and, whenever a degeneracy arises in parameter inference from one survey, the other surveys may be consulted to see if the degeneracy may be broken. For example, as well as providing the opportunity to measure correlators between sets of higher redshift galaxies, the SKA mission's large volume redshift survey will allow for cross-correlation with LSST, significantly improving the value of the redshift space datasets LSST will be gathering.

All of these missions are scheduled to have provided their data by the end of the current decade, making for a promising near future for large scale structure cosmology.

Connection to Theory

Gravity is best described by general relativity, but is more conveniently and quickly described by Newtonian gravity. On very large scales, the use of the full FLRW metric is required for accurate models of the Universe and of course when studying small scale dynamics, local metrics are necessary. On the intermediate scales that we study in LSS surveys, it is generally assumed that Newtonian gravity provides a good approximation for gravitational forces while resulting in significantly simpler equations than the full relativistic treatment would require. However, it is important to remember that this is just an approximation and that when studying high precision LSS surveys, a full analysis concerning the corrections relativistc gravity might lead to may be useful.

Fully modelling LSS requires one to take into account the two fluid nature of cosmic structure: dark matter underlies an observable baryonic matter galaxy field. Furthermore, one must take into account the fact that the distribution of density peaks in a study of the underlying dark matter density field might not perfectly match a study of the dark matter halo distribution; while halos are themselves density peaks, when studying density peaks on large enough scales that our peak may encompass multiple halos, we may find that, due to some halos being larger than others and their distribution being irregular, a simple direct

mapping of density peaks to halo distributions may lead to inaccurate predictions. Once a map of dark matter halos has been established, one must then account for the fact that, while baryonic galaxies are generally assumed to reside within halos, the centre of mass of any given galaxy is not necessarily going to correspond exactly to the centre of mass of the halo such that observations of galaxies which are taken to be observations of halos might lead to inaccurate results. The defining of new parameters to allow the mapping of the model of one of these distributions to another is known as biasing.

To define the halo biasing parameters, we begin by considering the halo distribution field to be a treatable as a power series expansion in the dark matter density field [21, 47], such that

$$\delta_{\rm h} = \bar{b}_0 + \bar{b}_1\delta + \frac{1}{2}\bar{b}_2\delta^2 + \bar{\gamma}_2\mathscr{G}_2(\Phi_{\rm v}|x^i) + \bar{\gamma}_{21}\mathscr{G}_2(-\Phi_{\rm v}^{(1)}, -\Phi_{\rm v}^{(2)}|x^i) + \bar{\beta}_1\nabla^2\delta(x^i) + \dots\,, \quad (4.55)$$

for free parameters $\bar{b}_{1,2,3}$, $\bar{\gamma}_{2,21}$, and $\bar{\beta}_1$, where the $\mathscr{G}_2$ are Galilean invariant operators representing the tidal stress tensor generated by the perturbatively estimable non-linear velocity potential $\Phi_{\rm v} = \sum_i \Phi_{\rm v}^{(i)}$. The $\bar{b}$ parameters model local biasing effects while the $\bar{\gamma}_{1,21}$ and $\bar{\beta}_1$ parameters model non-local effects, such as those caused by the large scale velocity and acceleration fields of dark matter. Note that this model can generically work for any biased tracer that can be modelled as a power series in the dark matter field; since we will be working with dark matter halos and incorporating galaxies via the HOD method, we will continue referring to these biasing parameters as applying to halos for the remainder of this proposal.

In order to translate these biasing terms into a format that can easily be incorporated into perturbation theory, we can then define a new set of renormalised biasing parameters [48] based upon the ensemble average of the derivative of the halo field with respect to the matter density field:

$$b_n \equiv \left\langle \frac{\partial^n \delta_{\rm h}}{\partial \delta^n} \right\rangle \equiv (2\pi)^3\delta^{(D)}(k^i - k_1^i - \dots - k_n^i)\Gamma_{\rm h}^{(n)}(k_1^i, \dots, k_n^i)\,, \quad (4.56)$$

where we have defined both the observable biasing parameters $b_{\rm n}$ and the nth order kernels $\Gamma_{\rm h}^{(n)}$, the exact forms of which are given in [47] up to third order. The non-local $\gamma_{1,21}$ and β_1 parameters can be defined in a number of ways using different approximations as is discussed in detail in [47] and [49]. With these new parameters, we can define the halo-halo

and halo-density field cross power spectra up to one-loop order as

$$P_{\rm hh}(k) = b_1^2 P_{\rm mm}(k) + b_1 b_2 P_{b_1 b_2}(k) + b_1 \gamma_2 P_{b_1\gamma_2}(k) + b_2^2 P_{b_2 b_2}(k) + b_2 \gamma_2 P_{b_2\gamma_2}(k) + \gamma_2^2 P_{\gamma_2\gamma_2}(k) + b_1 \gamma_{21} P_{b_1\gamma_{21}}(k) - 2 b_1 \beta_1 k^2 P_{11}(k) \,, \tag{4.57}$$

$$P_{\rm hm}(k) = b_1 P_{\rm mm}(k) + \frac{1}{2}\left[b_2 P_{b_1 b_2}(k) + \gamma_2 P_{b_1\gamma_2}(k) + \gamma_{21} P_{b_1\gamma_{21}}(k)\right] - \beta_1 k^2 P_{11}(k) \,, \tag{4.58}$$

where $P_{\rm mm}$ is the fully non-linear matter power spectrum, P_{11} is the tree level power spectrum, and $P_{b_1 b_2}$, $P_{b_1\gamma_2}$, and $P_{b_1\gamma_{21}}$ are functions of the dark matter density field. The cross power spectrum can be fitted to simulation results of halo and density field correlators in order to calibrate the biasing parameters, allowing the halo-halo power spectrum to be calculated and compared to observational data.

In [47], the halo-halo autocorrelation one-loop bispectrum was derived in terms of these new parameters, but they did not derive the halo-density field cross correlation bispectrum. The tree level and one-loop contributions of the halo auto-bispectrum are given by

$$\begin{aligned} B_{\rm hhh}(k_1,k_2,k_3) =& \Gamma_h^{(2)}(k_1^i,k_2^i)\Gamma_h^{(1)}(k_1)\Gamma_h^{(1)}(k_2)P_{11}(k_1)P_{11}(k_2) \\ &+ \int \frac{d^3q}{(2\pi)^3}\Gamma_h^{(2)}(k_1^i-q^i,q^i)\Gamma_h^{(2)}(k_2^i+q^i,-q^i)\Gamma_h^{(2)}(k_1^i-q^i,k_2^i+q^i) \\ &\times P_{11}(|k_1^i-q^i|)P_{11}(|k_2^i-q^i|)P_{11}(q)P_{11}(k_3) \\ &+ \int \frac{d^3q}{(2\pi)^3}\Gamma_h^{(3)}(k_3^i,k_2^i-q^i,q^i)\Gamma_h^{(2)}(k_2^i-q^i,q^i)\Gamma_h^{(1)}(k_3^i)P_{11}(|k_2^i-q^i|) \\ &\times P_{11}(q)P_{11}(k_3) \,. \end{aligned} \tag{4.59}$$

Furthermore one must take into account observational systematic errors, such as the distortion of light which may lead to inaccuracies in distance measurements made by observations. The peculiar velocity of galaxies leads to Doppler effects which can distort observed length scales along the line of sight of the telescope, making redshift surveys inherently inaccurate unless these Redshift Space Distortions (RSDs) are taken into account.

The relation between real space x^i and redshift space $x_{\rm r}^i$ is given by [50]

$$x_{\rm r}^i = x^i + \frac{\hat{z}^j v_j}{aH}\hat{z}^i, \tag{4.60}$$

where $\hat{z}^i$ is a unit vector in the direction of the observer's line of sight and v^i is the peculiar velocity of the object under observation. Of course, the number of objects observed will be

unaffected by a change from real to redshift space, so $\rho(x^i)d^3x^i = \rho_r(x^i r)d^3x^i r$, such that

$$\delta r(x^i r) = \left(1+\delta(x^i(x^i r))\right)\left|\frac{\partial x^i r}{\partial x^i}\right|^{-1}_{x^i(x^i r)} - 1 \,, \tag{4.61}$$

which can be converted into the more commonly used Fourier space to give

$$\delta_r(k^i r) = \delta(k^i) + \int d^3x e^{-\mathrm{i}k^j x_j}\left(e^{-i\frac{k_z}{aH}v_z(x^i)} - 1\right)\left(1+\delta(x^i)\right) \,. \tag{4.62}$$

This can be used to derive forms for observable galaxy correlation functions in redshift space, correcting for the differences that would otherwise exist between redshift space observations and real space theory. Previous studies [51, 52] have developed the analytic tools necessary to incorporate RSDs into the EFTofLSS correlators but precise calibration of the counterterms for higher order correlator loop corrections has not yet been performed.

In this thesis we concern ourselves solely with dark matter density fields in a Newtonian background. At the end of the description of the research conducted thus far, we offer a summary of near future research plans, which primarily relate to connecting our research to observables by taking into account relativistic corrections, biasing, and RSDs.

4.4.2 | The Linear Power Spectrum

As we currently understand it, at very early times the Universe was radiation dominated with subleading matter and cosmological constant terms. However, the effects of matter became more important with time as radiation gradually reduced in energy and the Universe entered a brief phase of matter-radiation equality before entering the era of matter domination.

We can define the dimensionless power spectrum, $\Delta^2(k)$, which measures the contribution of inhomogeneities per logarithmic interval to the variance in the matter density fluctuations, by

$$P(k) = \frac{2\pi^2}{k^3}\Delta^2(k) \,. \tag{4.63}$$

The power spectrum is unique among LSS correlators in that it contains a non-zero measurement of the convolution of only linear density fields; while $\bar{B}_{111} = \bar{T}_{1111} = 0$, $\bar{P}_{11}$ is an important observable and constitutes the dominant contribution to the power spectrum. This allows us to use the power spectrum to study the evolution of the linear fields in isolation. We will now review how the cosmological epochs whose dynamics were studied in Chapter 4 contribute to the form of the linear power spectrum that is visible today.

During radiation domination, the subhorizon density field remained relatively constant, as is described in Chapter 4.3.3, while the superhorizon scale density fields grew linearly

with time. During matter domination, the subhorizon density field evolved as $\delta(t) \approx t^{2/3}$. As such, density inhomogeneities which entered the horizon during the radiation dominated era will have grown as t before horizon crossing, remained constant after horizon crossing, and then begun growing as $t^{2/3}$ after matter-radiation equality, while perturbations which did not cross the horizon until after matter-radiation equality will have continuously grown, with their rate of growth changing from t to $t^{2/3}$ at the time of horizon crossing.

Focusing on the radiation dominated era, we can define a Hubble wavelength

$$k_{\mathrm{H}} = \frac{2\pi}{R_{\mathrm{H}}} \, , \tag{4.64}$$

where R_{H} is the distance to the horizon. Any evolving system will be dependent on its initial values so we can plainly see that the amplitude of the density perturbations at $k_{\mathrm{H}}(t)$ for any t will depend upon the initial slope of the power spectrum, n. The scale free power spectrum is defined as being the value of n such that $\Delta^2(k_{\mathrm{H}}(t))$ is a constant on superhorizon scales, defined in terms of Eq. (4.64) as being $k > k_{\mathrm{H}}$. This can be seen to imply that $n = 1$; remembering Eq. (4.63), we can see that during the radiation domination era,

$$P_{11}(k) \begin{cases} \sim k \text{ for } k > k_{\mathrm{H}} \, , \\ \sim k^{-3} \text{ for } k < k_{\mathrm{H}} \, . \end{cases} \tag{4.65}$$

Thus, by studying the turnaround at which the power spectrum changes from scaling roughly as k to k^{-3}, we can use the linear power spectrum as a probe of $\Omega_{\mathrm{r}}/\Omega_{\mathrm{m}}$ as a function of time, using it to ascertain when the transition from radiation to matter domination took place and how long the transition took.

See Fig. 4.3 for a logarithmic plot of the observed linear power spectrum as a function of k, as measured by WMAP.

In the past few billion years, the physics described by the cosmological constant term has become increasingly important, such that we now live in a Λ dominated universe with subleading but not insubstantial contributions from matter, which appears to be predominantly made up of cold dark matter (CDM), and negligible contributions from radiation and curvature.

Thus, the standard model of present time cosmology is referred to as the ΛCDM model, in which the universe is dominated primarily by Λ and to a lesser extent by matter with their exact ratio being constrained to increasing precision with time as new survey data becomes available, and this is the model we will be using for our calculations throughout this thesis.

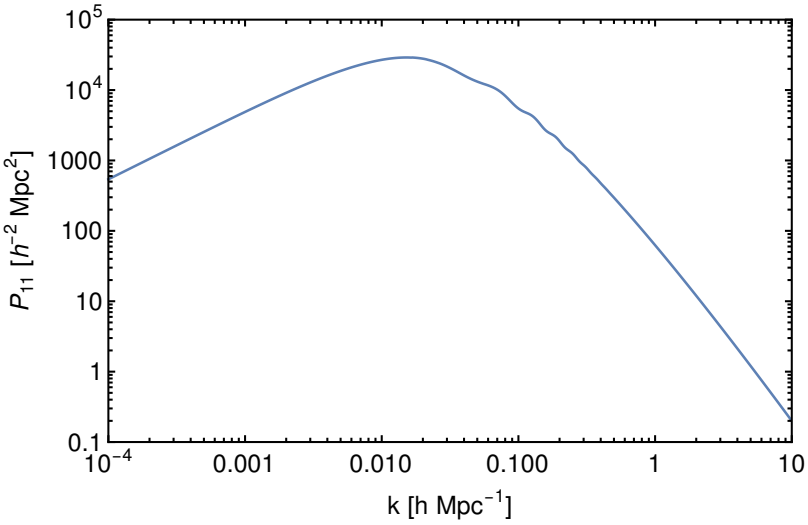

Figure 4.3: A logarithmic plot of the present time linear power spectrum of dark matter as measured by WMAP. Notice that at low k, the power spectrum scales as k; it then undergoes a period of transition due to matter-radiation equality before scaling as k^{-3}. Because $k \sim t$, we can use the power spectrum as a probe of $\Omega_{\rm r}/\Omega_{\rm m}$ as a function of time.

As future surveys measure the power spectrum and other measures of large scale structure to increasingly high precision, their various methods will allow each to estimate particular regions of the power spectrum, as each will probe its own set of wavenumbers. Surveys of galaxy clustering are generally most useful on scales ranging from roughly $0.01 < k < 0.5$, while measures of lensing allow measurement of the higher wavenumber components of the power spectrum. Additionally, measurements of higher redshifts permit exploration of larger wavenumbers, such that high redshift radio telescopes such as SKA should probe larger momentum scales than closer probes such as SPHEREx and Euclid, at the sacrifice of not being able to probe smaller wavenumbers.

4.5 | Summary

In this chapter, we have described the inflationary model, the most popular model for early time cosmology in contemporary physics and have described how it leads to the creation of inhomogeneities, beginning from a perfectly homogeneous pre-inflationary universe. We have described how these inhomogeneities can lead to the structures we observe around us today and have shown how they evolve in time as a function of the matter and radiation densities of the Universe. Specifically, we have shown that during matter dominated epochs of cosmological history, inhomogeneities grow with time as as $t^{2/3}$, while in radiation dominated epochs they grow as $\ln(t)$, which damping is often referred to as the Mészáros effect, and we

have derived the form for the linear perturbation growth factor in a Λ dominated universe which will be used extensively to model perturbations in a ΛCDM cosmology in Chapter 5. Finally, we have shown how the observable power spectrum demonstrates the effects of the Universe's historical eras of matter and radiation domination. In the following chapters we will discuss how to go beyond the linear approximation for the inhomogeneous equations of motion.

5

Perturbative Models of Large Scale Structure

In Chapter 4 we discussed dark matter density field inhomogeneities by studying the solutions to the linearised forms of Eqs. (4.20) and (4.21). These solutions provide approximate descriptions of the density inhomogeneity field on large scales, but become increasingly inaccurate as we look at density inhomogeneities on smaller scales, where δ and θ become larger such that the higher order terms can no longer be approximated as zero. SPT attempts to analytically model LSS inhomogeneities on smaller scales by assuming that the fully non-linear form of $\delta(k^i, \eta)$ can be approximated by a power series expansion around the linear solution [5, 6]:

$$\delta_{\mathrm{n}} \approx \delta_1 + \delta_2 + \delta_3 + \dots \,, \tag{5.1}$$

where each δ_i is a weighted product of i linear density fields.

Until the early 2010s, this was the primary analytic model of LSS available to cosmologists. However, it consistently provided predictions for LSS correlators that were at odds with observations and failed to converge as higher order terms in the expansion were added, making every order of the expansion unreliable. This is due to the fact that the density contrast of a matter field which contains regions that have undergone gravitational collapse cannot, in fact, be accurately modelled by a power series solution to Eqs. (4.20) and (4.21). This is due to the highly non-linear effects of small scale physics within gravitational wells; in order to accurately estimate δ_{n}, we would need to introduce a cutoff to prevent these small scales from being included in our linear expansion and add terms to the sum given in Eq. (5.1) that account for this small scale physics. This is why the EFTofLSS was developed in 2010; the EFTofLSS expands upon Eq. (5.1) by incorporating additional terms which do not come from the power series solution of δ for both Eqs. (4.20) and (4.21) but instead from the stress energy term τ^{ij} in Eq. (4.21) and which, due to the symmetries of the equations of

motion, can be shown to be products of the linear denstiy field and free parameters which are to be fitted to simulation data. Thus, we now have

$$\delta_{\rm n} \approx \delta_1 + \delta_2 + \delta_3 + \cdots + \tilde{\delta}_2 + \tilde{\delta}_3 + \dots \,, \tag{5.2}$$

where the $\tilde{\delta}$ terms are the corrective terms, which we label counterterms, which originate from the stress-energy tensor. While increasing the accuracy of our analytic solutions to the equations of motion, they are also cutoff dependent in a manner that cancels the cutoff dependence of the perturbative δ fields they are correcting, leading to a cutoff independent estimator of the non-linear density field.

In this chapter we will review the derivation of both SPT and the EFTofLSS before describing in more detail the time evolution of the individual contributions to the power series and how the perturbative contributions to LSS they represent can be used in simulations to measure correlation functions, ultimately allowing us to connect our models with reality in a manner that allows the models to be used for the testing of fundamental physics.

5.1 | Standard Perturbation Theory

We will now begin our derivation of SPT which, until the development of the EFTofLSS, constituted the most accurate available model of dark matter density perturbations across the Universe.

We wish to solve Eqs. (4.15) and (4.16) in a manner which will permit analytic estimations of the observables described by these equations. Furthermore, SPT begins by assuming that an accurate model of these perturbations can be found entirely within our definitions of δ; thus, since the terms in the stress-energy tensor do not correspond to any physical quantities,we may set $\tau^{ij} = 0$.

The perturbative approach to describing LSS begins with the assumption that we can model the non-linear density and velocity fields as expansion around the linear fields studied in Chapter 4,

$$\delta_{\rm n}(k^i, \eta) = \sum_{n=1}^{\infty} \delta_n(k^i, \eta) \,, \qquad \theta_{\rm n} = \sum_{n=1}^{\infty} \theta_n(k^i, \eta) \,, \tag{5.3}$$

where the terms δ_n and θ_n are weighted products of n linear density fields, themselves time evolutions of the initial density field.

This perturbative expansion in terms of δ_1 suggests a power series solution to the equations of motion. Expanding upon Eq. (4.31), we can split each element in the expansion into

time dependent and independent components to give

$$\hat{\delta}_n(k^i,\eta) = D_n(\eta)\delta_n(k^i)\ , \qquad \theta_n(k^i,\eta) = \dot{D}_1(\eta)D_{n-1}(\eta)\theta_n(k^i)\ . \tag{5.4}$$

In EdS cosmology, the higher order fields scale as $D_n = a^n$, making the model mathematically simple to implement. Indeed, even though ΛCDM values for D_1 are often used in the literature, it is not uncommon to approximate n-th order density fields as scaling as D_1^n; throughout this paper we refer to this as the EdS approximation.

Equating terms with the same time dependence allows us to find the n-th order time independent components. Specifically, for $n > 1$, substituting Eq. (5.4) into Eqs. (4.20) and (4.21) gives us the equations of motion for the n-th order power series terms:

$$n\delta_n(k^i) + \theta_n(k^i) = A_n(k^i)\ , \tag{5.5}$$

$$3\delta_n(k^i) + (1+2n)\theta_n(k^i) = B_n(k^i)\ , \tag{5.6}$$

where

$$A(k^i) = -\int_{q_1^i}^{\Lambda}\int_{q_2^i}^{\Lambda}\delta^{(\mathrm{D})}\left(k^i - q_1^i - q_2^i\right)\frac{k^j q_1^j}{q_1^2}\sum_{m=1}^{n-1}\theta_m(k_1^i)\delta_{n-m}(k_2^i)\ , \tag{5.7}$$

$$B(k^i) = -\int_{q_1^i}^{\Lambda}\int_{q_2^i}^{\Lambda}\delta^{(\mathrm{D})}\left(k^i - q_1^i - q_2^i\right)\frac{k^2 q_1^j q_{2,j}}{q_1^2 q_2^2}\sum_{m=1}^{n-1}\theta_m(k_1^i)\theta_{n-m}(k_2^i)\ . \tag{5.8}$$

If we now solve Eqs (5.6) for δ_n and θ_n, we find that

$$\delta_n(k^i) = \frac{(1+2n)A_n(k^i) - B_n(k^i)}{(2n+3)(n-1)}\ , \qquad \theta_n(k^i) = \frac{-3A_n(k^i) + nB_n(k^i)}{(2n+3)(n-1)}\ , \tag{5.9}$$

from which we can find that the n-th order density and velocity fields are given by

$$\delta_n(k^i) = \int_{q_1^i}^{\Lambda}\cdots\int_{q_{\mathrm{n}}^i}^{\Lambda}\delta^{(\mathrm{D})}\left(k^i - \sum_{m=1}^{n} q_m^i\right)F_n(q_1^i,...,q_{\mathrm{n}}^i)\prod_{m=1}^{n}\delta_1(q_m^i)\ , \tag{5.10}$$

$$\theta_n(k^i) = \int_{q_1^i}^{\Lambda}\cdots\int_{q_{\mathrm{n}}^i}^{\Lambda}\delta^{(\mathrm{D})}\left(k^i - \sum_{m=1}^{n} q_m^i\right)G_n(q_1^i,...,q_{\mathrm{n}}^i)\prod_{m=1}^{n}\delta_1(q_m^i)\ , \tag{5.11}$$

where $\int_{q^i} = \int \mathrm{d}^3 q^i/(2\pi)^3$ and the functions of momenta F_n and G_n are the gravitational coupling kernels of the fields, given by

$$F_n(k_1^i,...,k_\mathrm{n}^i) = \sum_{m=1}^{n-1} \frac{G_m(k_1^i,...,k_m^i)}{(2n+3)(n-1)}[(2n+1)\alpha(\kappa_1^m,\kappa_{m+1}^n)F_{n-m}(k_{m+1}^i,...,k_n^i) + 2\beta(\kappa_1^m,\kappa_{m+1}^n)G_{n-m}(k_{m+1}^i,...,k_n^i)] \,, \tag{5.12}$$

$$G_n(k_1^i,...,k_n^i) = \sum_{m=1}^{n-1} \frac{G_m(k_1^i,...,k_m^i)}{(2n+3)(n-1)}[3\alpha(\kappa_1^m,\kappa_{m+1}^n)F_{n-m}(k_{m+1}^i,...,k_n^i) + 2n\beta(\kappa_1^m,\kappa_{m+1}^n)G_{n-m}(k_{m+1}^i,...,k_n^i)] \,, \tag{5.13}$$

where $\kappa_a^b = \sum_{i=a}^b k_i$ and $F_1 = G_1 = 1$. These originate from the source terms and encapsulate coupling between LSS and smaller scale gravitational collapse. In clustering statistics these kernels are used in their symmetrised form referred to as $F_n^{(\mathrm{s})}$ and $G_n^{(\mathrm{s})}$.

5.2 | The Effective Field Theory

We begin our derivation of the EFTofLSS by acknowledging that the failing of SPT is its belief that modelling the Universe as perturbative even down to infinitesimal scales and that the best way to correct the associated errors is to introduce a cutoff, a scale below which we acknowledge our perturbative model does not work, and account for all of the sub-cutoff physics in additional terms defined by new free parameters. This subchapter will replicate the derivation of the equations of motion for a fluid in an expanding Universe with the cutoff and associated parameters being taken into account to highlight their effects on the perturbative model.

We coarse grain the phase space by introducing a smoothing function, $W_\Lambda(k)$. The presence of this function differentiates the EFTofLSS from SPT, and it is defined by

$$W_\Lambda(k) = e^{-\frac{1}{2}\frac{k^2}{\Lambda^2}} \,, \tag{5.14}$$

for some cutoff $\Lambda < k_\mathrm{n}$. Here k_n is the non-linear scale beyond which the physics is non-perturbative. Throughout this paper we choose $\Lambda = 0.3h$ Mpc^{-1} unless explicitly stated otherwise. Note that the theory is independent of the cutoff as the dependence of the counterterms counteracts the dependence of the perturbative terms.

$$\left[\frac{\mathrm{D}f}{\mathrm{D}t}\right]_\Lambda = \frac{\partial f}{\partial t} + \frac{p^i}{ma^2}\cdot\frac{\partial f}{\partial x^i} - m\int d^3y^i W_\Lambda(x^i - y^i)\frac{\partial \phi}{\partial x^i}\cdot\frac{\partial f}{\partial p^i} = 0 \,, \tag{5.15}$$

Taking the first three moments of Eq. (5.15) gives us definitions for the matter and momentum densities,

$$\rho(x^l,\eta) = \frac{m}{a^3}\int \mathrm{d}^3y^l \int d^3p^m\, W_\Lambda(x^i-y^i)\, f(y^l,p^m,\eta)\,, \tag{5.16}$$

$$\pi^i(x^l,\eta) = \frac{1}{a^4}\int \mathrm{d}^3y^l \int d^3p^m\, W_\Lambda(x^i-y^i)\, p^i\, f(y^l,p^m,\eta)\,, \tag{5.17}$$

$$\sigma^{ij}(x^l,\eta)+\tau^{ij}(x^l,\eta) = \frac{1}{ma^5}\int \mathrm{d}^3y^l \int d^3p^m\, W_\Lambda(x^i-y^i)\, p^ip^j\, f(y^l,p^m,\eta)\,, \tag{5.18}$$

which are set apart from their SPT analogues by the inclusion of the cutoff and the associated spatial integral. We can now rederive the equations of motion for this fluid which take the same form as Eqs (4.20) and (4.21), but with explicit cutoff dependence in every term which contains a sum over all scales, such as the fluid density and velocity divergence fields. We also take the stress-energy tensor, set to zero in SPT, and allow it to remain in our equations, imbuing it with its own cutoff dependence; given that it represented no physics in SPT, its components are free terms that we may use to regularise our cutoff dependent theory*. Specifically, we intend to expand the stress-energy tensor to obtain a series of new, cutoff dependent terms each of which will be dependent on one or more free parameter. We will then fit each of these free parameters to the fully non-linear density fields we record from simulations in order to obtain a new perturbative estimator for the non-linear field which both incorporates non-perturbative small scale physics into its power series and incorporates cancelling cutoff dependencies between the δ terms and the stress-energy terms such that the series will be cutoff independent†.

Given that this stress-energy tensor does not correspond to any of the physical properties of our fluid that such tensors usually describe but is instead being used as a free mathematical object from which new terms can be obtained without affecting the physical realism of our equations of motion, it is sometimes referred to in the literature as the *effective* stress-energy tensor. For the remainder of this thesis, however, we will refer to it simply as the stress-energy

*While the stress-energy terms treated in the EFTofLSS are generally regarded as being abstract mathematical quantities that simply make use of existing terms in the equations of motion, the regularisation that they represent could be interpreted as a form of pressure from small scale physics affecting scales beyond the cutoff, reimbuing the stress-energy tensor with its physical interpretations. It should be noted, however, that the effective pressure of this fluid that we are now interpreting our stress-energy tensor as representing does not behave in the same manner as conventional fluid pressure, which exerts a repulsive force; instead, it can take any value and affect the larger scale dynamics in any way.

†Of course, any cutoff dependence in the results would render all results unusable, as the cutoff is not a physical observable but an arbitrarily chosen point in k space which we decide to use as the minimal scale for our power series and all of the physics beyond which we choose to encapsulate in our new terms which arise from the stress-energy tensor; dependence in our prediction for the observable δ_{n} on this arbitrary cutoff would not correspond to dependence on any observable and there would be no motivation for deciding that any one cutoff was more physical than any other.

tensor, as no other stress-energy tensors are included in our calculations which could lead to confusion.

5.2.1 | The Stress-Energy Tensor

In SPT, the stress-energy tensor would be set to zero and the cutoff to infinity. This is what separates the EFTofLSS from SPT; in the EFTofLSS, we have a non-infinity cutoff and a non-zero stress-energy tensor. The question now is how can we construct the stress-energy tensor in a manner that is consistent with our physical model and is able to accurately regularise our cutoff dependence.

To satisfy the symmetries of the cosmological model, the components of the effective stress-energy tensor τ_{ij} must be compatible with homogeneity and isotropy as well as Galilean invariance. The only gravitational terms which are compatible with these symmetries are the second derivatives of the gravitational potential ϕ, and of the velocity potential u.

The various terms in the stress-energy tensor can be grouped into two categories: viscosity terms, which provide the correlated corrections to the perturbative terms, and noise terms, which account for the self-coupling of non-perturbative (strongly coupled) small scale modes analogous to the one-halo term in the halo model.

At cubic order, where the stress-energy tensor regularises δ_3, there are two EFTofLSS terms in Eq. (4.23):

$$\tau_\theta|_1 = -d_\phi^2 \partial^l \partial_l \phi + \frac{d_u^2}{\dot{a} f} \partial^l \partial_l u \,, \tag{5.19}$$

where u is the velocity potential such that $\partial^i u = v^i$, for free parameters d_ϕ^2 and d_u^2 which we combine in the new variable $d^2 \equiv d_\phi^2 + d_u^2$.

At quartic order, where we regularise δ_4, this expands to become

$$\tau_\theta^{ij}|_2 = -d^2 \delta^{ij} \delta_2 + c_1 \delta^{ij} (\partial^l \partial_l \phi)^2 + c_2 \partial^i \partial^j \phi \, \partial^l \partial_l \phi + c_3 \partial^i \partial_k \phi \partial^j \partial^k \phi \,. \tag{5.20}$$

We will find it useful to integrate these over time to define the counterterm density field at scale factor a as[‡]

$$\tilde{\delta}_n = \int \mathrm{d}a' G_\delta(a, a') \tau_\theta|_n \,. \tag{5.22}$$

[‡]By combining Equations (4.20) and (4.21) into a second order equation we can obtain the Green's function [53]

$$G_\delta(a, a') = \Theta(a - a') \frac{2}{5} \frac{1}{\dot{a}_0^2 \Omega_\mathrm{m}^0} \frac{D_1(a')}{a'} \left[\frac{D_{1-}(a)}{D_{1-}(a')} - \frac{D_1(a)}{D_1(a')} \right] \,, \tag{5.21}$$

for first order growing mode D_1 and decaying mode $D_{1-}(a) = H(a)$.

Defining the tidal tensor

$$s^{ij} \equiv \partial^i \partial^j \phi - \frac{1}{3}\delta^{ij}\partial^l \partial_l \phi \tag{5.23}$$

and its contract $s = s^{ij}s_{ij}$, one can obtain

$$\tau_\theta|_1 = -d^2 \partial^l \partial_l \delta_1 \ , \tag{5.24}$$

$$\tau_\theta|_2 = -d^2 \partial^l \partial_l \delta_2 - e_1 \partial^l \partial_l \delta_1^2 - e_2 \partial^l \partial_l s^2 - e_3 \partial_i \left[s^{ij} \partial_j \delta_1 \right] \ , \tag{5.25}$$

where e_i are functions of c_i and d_u^2, leaving us with four free parameters: d^2, e_1, e_2, and e_3.

We can define the counterterm density field analogously to Eq. (5.11) by defining a set of counterkernels $\tilde{F}$, such that

$$\tilde{\delta}_n(k^i) \equiv \int_{q_1^i} ... \int_{q_n^i} \delta^{(\mathrm{D})} \left(k^i - \sum_{i=1}^{n} q_i^i \right) \tilde{F}_n(q_1^i, ..., q_n^i) \prod_{i=1}^{n} \delta_1(q_i^i) \ . \tag{5.26}$$

5.2.2 | The Counterterms

We wish to define the nth-order counterkernels in terms of the free parameters of the nth order stress-energy tensor. The parameters d^2 and $e_{1,2,3}$ are time dependent; we can approximate them as scaling as $D_1^m(a)$ for m-dependent power series growth factors D^m. The value for m can be inferred from approximating the linear power spectrum by a power law k^{n_n} around the non-linear scale and assuming self similarity, leading to $m = (1 - n_\mathrm{n})/(n_\mathrm{n} + 3)$ [11, 14]. For the small-scale terms in the EFT, we estimate $n_\mathrm{n} \approx -3/2$, yielding $m = 5/3$. The part of the counterterm that is capturing the cutoff dependence of the SPT loop integrals needs to have $m = 1$ instead. We can therefore separate the time dependent and time independent components by defining the new parameters $\bar{d}^2$ and $\bar{e}_i$ as

$$d^2 \equiv D_1^m(a) \dot{a}_0^2 \Omega_\mathrm{m}^0 \bar{d} \ , \tag{5.27}$$

$$e_i^2 \equiv D_1^m(a) \dot{a}_0^2 \Omega_\mathrm{m}^0 \bar{e}_i \ . \tag{5.28}$$

In order to obtain the cubic order counterterm, we insert this definition of d^2 into the cubic order stress-energy tensor and insert the result into Eq. (5.22). The time dependency arising from the Green's function in the integral is [14]

$$g_1(a,m) = -\frac{2}{(m+1)(2m+7)} D_1^{m+1}(a) \ , \tag{5.29}$$

such that

$$\tilde{\delta}_1(k^i,a) = g_1(a,m)\vec{d}^2k^2\delta_1(k^i,a) \ , \tag{5.30}$$

which gives us

$$\tilde{F}_1(k^i,a) = g_1(a,m)\vec{d}^2k^2 \ . \tag{5.31}$$

In order to define a counterkernel from the quartic order stress-energy tensor, we will split it into three components [14]:

$$\tilde{F}_2(k_1^i,k_2^i) \equiv \tilde{F}_2^{\eta}(k_1^i,k_2^i) + \tilde{F}_2^{\alpha\beta}(k_1^i,k_2^i) + \tilde{F}_2^{\delta}(k_1^i,k_2^i) \ , \tag{5.32}$$

where $\tilde{F}_2^{\eta}$ stems from the three terms containing e_i, $\tilde{F}_2^{\alpha\beta}$ comes from inserting $\tilde{\delta}_1$ and $\tilde{\theta}_1$ into the source terms, and $\tilde{F}_2^{\delta}$ comes from replacing δ_1 with δ_2 in the d^2 term in Eq. (5.25). Solving the equations of motion with $k^2\delta_1$ as one of the source terms in the coupling kernel and considering $k^2\delta_2$ in the source terms and integrating these sources with the Green's function leads to

$$\tilde{F}_2(k_1^i,k_2^i) = \sum_{i=1}^{3} g_2^e\bar{e}_i E_i(k_1^i,k_2^i) + g_1\vec{d}^2\Gamma(k_1^i,k_2^i) \ , \tag{5.33}$$

where

$$g_2^{\mathrm{e}}(a,m) = -\frac{2}{(m+2)(2m+9)}D_1^{m+1}(a) \ , \tag{5.34}$$

and the E_i are shape functions which, combined with the free parameters e_i, regulate the shape dependence of the counterterms and arise from the symmetry inspired terms quadratic terms in the gravitational potential:

$$E_1(k_1^i,k_2^i) = (k_1^i+k_2^i)^2 \ , \tag{5.35}$$

$$E_2(k_1^i,k_2^i) = (k_1^i+k_2^i)^2\left(\frac{(k_1^jk_{2,j})^2}{k_1^2k_2^2} - \frac{1}{3}\right) \ , \tag{5.36}$$

$$E_3(k_1^i,k_2^i) = -\frac{1}{6}(k_1^i+k_2^i)^2 + \frac{1}{2}k_2^jk_{3,j}\left(\frac{(k_2^j+k_3^j)k_{3,i}}{k_3^2} + \frac{(k_2^j+k_3^j)k_{2,j}}{k_2^2}\right) \ . \tag{5.37}$$

Once integrated over time, the Γ function is given by

$$\Gamma(k_1^i,k_2^i) = \frac{g_2^e(a,m)}{g_1(a,m)}(k_1^i+k_2^i)^2F_2(k_1^i,k_2^i) + \tilde{F}_2^{\alpha\beta}(k_1^i,k_2^i) \ , \tag{5.38}$$

with

$$\begin{aligned}\tilde{F}_2^{\alpha\beta}(k_1^i,k_2^i) =& k_2^2\left[\frac{g_2^{\rm a}(a,m)}{g_1(a,m)}\alpha(k_2^i,k_1^i)+\frac{\tilde{g}_2^{\rm a}(a,m)}{g_1(a,m)}\alpha(k_1^i,k_2^i)+\frac{g_2^{\rm b}(a,m)}{g_1(a,m)}\beta(k_1^i,k_2^i)\right]\\ &+k_1^2\left[\frac{g_2^{\rm a}(a,m)}{g_1(a,m)}\alpha(k_1^i,k_2^i)+\frac{\tilde{g}_2^{\rm a}(a,m)}{g_1(a,m)}\alpha(k_2^i,k_1^i)+\frac{g_2^{\rm b}(a,m)}{g_1(a,m)}\beta(k_1^i,k_2^i)\right]\end{aligned} \tag{5.39}$$

where

$$g_2^{\rm a}(a,m) = -\frac{1}{(m+1)(m+2)(2m+9)}D_1^{m+1}(a)\ , \tag{5.40}$$

$$\tilde{g}_2^{\rm a}(a,m) = (m+2)g_2^{\rm a}(a,m)\ , \tag{5.41}$$

$$g_2^{\rm b}(a,m) = -\frac{4}{(m+1)(2m+7)(2m+9)}D_1^{m+1}(a)\ . \tag{5.42}$$

For simplicity, we can then define a new set of parameters

$$\gamma_1 \equiv -g_1(a,m)\bar{d}^2\ , \tag{5.43}$$

$$\gamma_2 \equiv -g_1(a,m)\bar{d}^2\ , \tag{5.44}$$

$$\varepsilon_i \equiv -g_2^e(a,m)\bar{e}_i\ , \tag{5.45}$$

where the two γ terms are defined identically in terms of the model's symmetries but are treated separately when calculating their values and where we have simply incorporated the time dependent terms into our definition of the parameters, giving us

$$\tilde{F}_1(k) = -\gamma_1 k^2\ , \tag{5.46}$$

$$\tilde{F}_2(k_1^i,k_2^i) = -\left[\sum_{i=1}^{3}\varepsilon_i E_i(k_1^i,k_2^i)+\gamma_2\Gamma(k_1^i,k_2^i)\right]\ . \tag{5.47}$$

According to convention, γ_1 is referred to as the speed of sound, $c_{\rm s}^2$, when calculated from the power spectrum. For the remainder of this thesis, we will refer to calculations of γ_1 made from the one loop power spectrum as c_s^2 and those made from the one loop bispectrum or trispectrum as γ_1.

5.3 | Time Evolution of Non-Linear Inhomogeneities

The n-th order growth factor D_n describes the growth of the density perturbation δ_n as the universe expands. It is common practice to assume EdS cosmology, such that $D_n = D_1^n$ to

simplify calculations. However, this approximation becomes increasingly inaccurate at lower redshifts as our universe is no longer dominated by matter but by dark energy. Here we review the ΛCDM growth factors, reproducing the work shown in [19].

From WMAP observations of the primordial power spectrum, we can infer the initial conditions from which we can generate the Gaussian density field δ_1. However, this of course does not accurately describe the density of dark matter we see around us as it takes no account of gravitational collapse. In order to generate fully non-linear fields we must simulate the evolution of this field until the present day in a manner that allows for the formation of halos; this gives us a representation of the real universe to which we can compare our theory.

One of the elements of our research which sets it apart from previous studies of EFTofLSS correlators is our use of ΛCDM growth factors in place of the more commonly used EdS approximation. We calculate the ΛCDM second order density field in Eq. (8.25) from the Gaussian initial condition δ_1 as

$$\delta_{2,\Lambda\mathrm{CDM}} = \frac{17}{21} D_{2A} \delta_1 \delta_1 - D_1^2 \Psi^j_{\delta_1} \delta_1 + \frac{2}{7} D_{2B} K_{\delta_1,ij} K_{\delta_1,ij} \,, \tag{5.48}$$

where the displacement fields are given by

$$\Psi^j_{\delta_m}(k^l) = \mathrm{i} \frac{k^l}{k^2} \delta_m(k^l) \tag{5.49}$$

and equivalently the tidal tensor is given by

$$K^{ij}_{\delta_m}(k^l) = \left(\frac{k^i k^j}{k^2} - \frac{1}{3} \delta^{(\mathrm{K})ij} \right) \delta_m(k^l) \,, \tag{5.50}$$

where we used that $5/7 D_{2A} + 2/7 D_{2B} = D_1^2$.

The second order solutions are found by solving

$$\begin{aligned} &\frac{\mathrm{d}^2}{\mathrm{d}\ln a^2} \frac{D_2}{a^2} + \left(6 + \frac{\mathrm{d}\ln H}{\mathrm{d}\ln a} \right) \frac{\mathrm{d}}{\mathrm{d}\ln a} \frac{D_2}{a^2} + \left[8 + 2 \frac{\mathrm{d}\ln H}{\mathrm{d}\ln a} - \frac{3}{2} \Omega_{\mathrm{m}}(a) \right] \frac{D_2}{a^2} \\ &= \begin{cases} \frac{7}{5} \left[\left(\frac{\mathrm{d}D_1}{\mathrm{d}a} \right)^2 + \frac{3}{2} \Omega_{\mathrm{m}}(a) \left(\frac{D_1}{a} \right)^2 \right] & \text{for } D_{2A} \,, \\ \frac{7}{2} \left(\frac{\mathrm{d}D_1}{\mathrm{d}a} \right)^2 & \text{for } D_{2B} \,, \end{cases} \end{aligned} \tag{5.51}$$

with initial conditions

$$a(t_0) = 0, \ \frac{D_{2A,B}}{a^2} = 1, \ \text{and} \ \frac{\mathrm{d}}{\mathrm{d}a} \frac{D_{2A,B}}{a^2} = 0 \,. \tag{5.52}$$

This gives two solutions, D_{2A} and D_{2B}, such that

$$\delta_2(k^i,a) = D_{2A}(a)A(k^i) + D_{2B}(a)B(k^i)\ . \tag{5.53}$$

By inserting the linear density field into Eqs. 4.20 and 4.21, one can derive the explicit terms for the higher order fields. The solution for the second order field is given by

$$A(k^i) = \frac{5}{7}\int \mathrm{d}^3q^i\ \alpha(q^i,k^i-q^i)\delta_1(q^i)\delta_1(k^i-q^i), \tag{5.54}$$

$$B(k^i) = \frac{2}{7}\int \mathrm{d}^3q^i\ \beta(q^i,k^i-q^i)\delta_1(q^i)\delta_1(k^i-q^i)\ . \tag{5.55}$$

Taking this to third order, we have

$$\begin{aligned}
\delta_{3,\Lambda\mathrm{CDM}} =& \delta_1\delta_2\left[2\left(\frac{5D_{3AA,1}}{18}+\frac{D_{3AA,2}}{6}+\frac{2D_{3BA}}{63}\right)\right.\\
&\left.-\frac{3}{2}\left(\frac{D_{3\mathrm{AB},1}}{9}+\frac{2D_{3\mathrm{AB},2}}{9}+\frac{8D_{3BB}}{189}\right)\right]\\
&+\delta_1\theta_2\left[-\frac{5D_{3AA,1}}{18}-\frac{D_{3AA,2}}{6}\right.\\
&\left.+\frac{5}{2}\left(\frac{D_{3\mathrm{AB},1}}{9}+\frac{2D_{3\mathrm{AB},2}}{9}+\frac{8D_{3BB}}{189}\right)-\frac{2D_{3BA}}{63}\right]\\
&-\Psi^j_{\theta_1}\partial_j\delta_2\left[2\left(\frac{5D_{3AA,1}}{18}+\frac{D_{3BA}}{21}\right)-\frac{3}{2}\left(\frac{D_{3\mathrm{AB},1}}{9}+\frac{4D_{3BB}}{63}\right)\right]\\
&-\Psi^j_{\theta_1}\partial_j\theta_2\left[-\frac{5D_{3AA,1}}{18}+\frac{5}{2}\left(\frac{D_{3\mathrm{AB},1}}{9}+\frac{4D_{3BB}}{63}\right)-\frac{D_{3BA}}{21}\right]\\
&-\Psi^j_{\delta_2}\partial_j\delta_1\left[2\left(\frac{D_{3AA,2}}{6}+\frac{D_{3BA}}{21}\right)-\frac{3}{2}\left(\frac{2D_{3\mathrm{AB},2}}{9}+\frac{4D_{3BB}}{63}\right)\right]\\
&-\Psi^j_{\theta_2}\partial_j\theta_1\left[-\frac{D_{3AA,2}}{6}+\frac{5}{2}\left(\frac{2D_{3\mathrm{AB},2}}{9}+\frac{4D_{3BB}}{63}\right)-\frac{D_{3BA}}{21}\right]\\
&+K_{\delta_1,ij}K_{\delta_2,ij}\left(\frac{4D_{3BA}}{21}-\frac{4D_{3BB}}{21}\right)+K_{\delta_1,ij}K_{\theta_2,ij}\left(\frac{20D_{3BB}}{63}-\frac{2D_{3BA}}{21}\right)\ .
\end{aligned} \tag{5.56}$$

where δ_2 and θ_2 refer to the normal EdS second order terms.

The third order growth factors can be found by solving

$$\begin{aligned}
&\frac{\mathrm{d}^2}{\mathrm{d}\ln a^2}\frac{D_3}{a^3}+\left(8+\frac{\mathrm{d}\ln H}{\mathrm{d}\ln a}\right)\frac{\mathrm{d}}{\mathrm{d}\ln a}\frac{D_3}{a^3}+\left[15+3\frac{\mathrm{d}\ln H}{\mathrm{d}\ln a}-\frac{3}{2}\Omega_{\mathrm{m}}(a)\right]\frac{D_3}{a^3}\\
&=\begin{cases}
\frac{18}{7}\left[2\frac{\mathrm{d}D_1}{\mathrm{d}a}+\frac{3}{2}\Omega_{\mathrm{m}}(a)\frac{D_1}{a}\right]\frac{D_{2A,B}}{a^2}+\frac{18}{7}a\frac{\mathrm{d}D_1}{\mathrm{d}a}\frac{\mathrm{d}}{\mathrm{d}a}\frac{D_{2A,B}}{a^2} & \text{for } D_{3AA,3AB}\ ,\\
15\frac{\mathrm{d}D_1}{\mathrm{d}a}\left[a\frac{\mathrm{d}}{\mathrm{d}a}\frac{D_{2A}}{a^2}+2\frac{D_{2A}}{a^2}-\frac{7}{5}\frac{D_1}{a}\frac{\mathrm{d}D_1}{\mathrm{d}a}\right] & \text{for } D_{3BA}\ ,\\
\frac{9}{2}\frac{\mathrm{d}D_1}{\mathrm{d}a}\left[a\frac{\mathrm{d}}{\mathrm{d}a}\frac{\mathrm{d}D_{2B}}{a^2}+2\frac{D_{2B}}{a^2}\right] & \text{for } D_{3BB}\ ,
\end{cases}
\end{aligned} \tag{5.57}$$

in combination with the consistency conditions

$$D_{3AA,2}=3D_1^3-\frac{2}{3}D_{3AB,1}-\frac{4}{7}D_{3BA}-\frac{16}{21}D_{3BB} \tag{5.58}$$

$$D_{3AB,2}=\frac{9}{4}D_1^3-\frac{5}{4}D_{3AA,1} \tag{5.59}$$

with initial conditions

$$\frac{D_3}{a^3}=1,\ \frac{\mathrm{d}}{\mathrm{d}a}\frac{D_3}{a^3}=0\ . \tag{5.60}$$

This gives the solution

$$\begin{aligned}
\delta_3(k^i,a)=&D_{3AA,1}(a)C_{AA,1}(k^i)+D_{3AA,2}(a)C_{AA,2}(k^i)+D_{3AB,1}(a)C_{AB,1}(k^i)\\
&+D_{3AB,2}(a)C_{AB,2}(k^i)+D_{3BA}(a)C_{BA}(k^i)+D_{3BB}(a)C_{BB}(k^i)\ ,
\end{aligned} \tag{5.61}$$

where

$$C_{AA,1}(k^i)=\frac{7}{18}\int d^3q^i\ \alpha(q^i,k^i-q^i)\delta_1(q^i)A(k^i-q^i), \tag{5.62}$$

$$C_{AA,2}(k^i)=\frac{7}{30}\int d^3q^i\ \alpha(q^i,k^i-q^i)\delta_1(k^i-q^i)A(q^i), \tag{5.63}$$

$$C_{AB,1}(k^i)=\frac{7}{18}\int d^3q^i\ \alpha(q^i,k^i-q^i)\delta_1(q^i)B(k^i-q^i), \tag{5.64}$$

$$C_{AB,2}(k^i)=\frac{7}{9}\int d^3q^i\ \alpha(q^i,k^i-q^i)\delta_1(k^i-q^i)B(q^i), \tag{5.65}$$

$$C_{BA}(k^i)=\frac{2}{15}\int d^3q^i\ \beta(q^i,k^i-q^i)\delta_1(q^i)A(k^i-q^i), \tag{5.66}$$

$$C_{BB}(k^i)=\frac{4}{9}\int d^3q^i\ \beta(q^i,k^i-q^i)\delta_1(k^i-q^i)B(q^i)\ . \tag{5.67}$$

The differences between the EdS and ΛCDM growth factors is small, but may be large enough to cause percent scale errors in calculations. In Chapters 8.2.1 and 8.2.2 we compare results for the second and third order density fields with both growth factors and show that

the differences can be significant for quantifying the sub-leading corrections induced by one-loop perturbation theory.

For EdS we would have $D_3 \equiv D_1^3$, leading to

$$\delta_{3,\mathrm{EdS}} = \frac{7\delta_1\delta_2}{18} + \frac{25\delta_1\theta_2}{54} + \frac{2K_{\delta_1,ij}K_{\theta_2,ij}}{9} - \frac{7\Psi^j_{\delta_1}\partial_j\delta_2}{18} - \frac{\Psi^j_{\delta_1}\partial_j\theta_2}{9} - \frac{\Psi^j_{\theta_2}\partial_j\delta_1}{2} \tag{5.68}$$

at $z = 0$.

5.4 | Correlation Functions

When studying perturbation theory, we will normally study the correlators of various combinations of perturbative density fields. As such, we will find ourselves interested in the linear power spectrum, P_{11}, the Fourier space correlator of two linear density fields, and perturbative corrections to it such as the correlator of one linear and one third order density field, P_{31}, and so on.

In surveys and simulations, the observed correlators will of course always be fully non-linear, such that we will be observing P_{nn}, B_{nnn}, and T_{nnnn} and comparing these to our perturbative predictions. SPT is built upon the assumption that the non-linear correlators can be constructed through the summation of all such relavent perturbative correlators; as such, one would assume that

$$P_{\mathrm{nn}} \approx P_{11} + P_{12} + P_{21} + P_{22} + P_{13} + P_{31} + \dots \,, \tag{5.69}$$

$$B_{\mathrm{nnn}} \approx B_{111} + B_{112} + B_{121} + B_{211} + B_{122} + B_{221} + \dots \,, \tag{5.70}$$

$$T_{\mathrm{nnnn}} \approx T_{1111} + T_{1112} + T_{1121} + T_{1211} + T_{2111} + T_{1122} + \dots \,. \tag{5.71}$$

Many of these terms may be shown to have a vanishing mean but a non-zero variance; as such, they are usually ignored but may lead to systematic errors in simulation results. In Chapters 8 and 9 we highlight this by showing the non-zero measured values of these correlators from our simulations and develop a method for removing them and, by extension, a large part of the variance, from our calculations.

When making comparisons between measured non-linear fields and calculated perturbative fields, we will often also make use of partially non-linear correlators, which are formed of the convolution of a combination of non-linear and perturbative density fields; the simplest such example is the power spectrum relating one non-linear field to one linear field, P_{n1}, which we will discuss further in Chapter 7.

5.4.1 | Feynman Diagrams

In order to represent the mathematical form of a perturbative correlator in a concise and easily interpreted way, it is common to illustrate them as Feynman diagrams. These are figures made up of a series of connected lines, which we refer to as legs, and vertices, each leg and vertex of which represents a particular component of the convolution that defines the correlator.

Of course, any representation of a function is valid as long as it consistently communicates the correct form of the function; in the standard formulation of Feynman diagrams for SPT and the EFTofLSS, we begin by deciding that each perturbative field δ_n can be represented by a single line which branches at a vertex which represents a kernel F_n into n lines, with the linear field simply taking the form of a straight line.

In order to illustrate a correlator between multiple perturbative fields, we create all possible diagrams in which the various legs of the fields are connected together, both to other legs from the same field and from the legs of other fields, while doing so noting that for an m-point correlator, there must be m legs free, that meaning not connected to any other, which are referred to as the diagrams external legs. Legs which are connected in such a way that they form a closed circle, which may nor may not contain kernels of higher order than F_1, are labelled loops and their kernels contain the momenta q which account for UV effects; these are the terms that will be affected by the introduction of our cutoff and which must be regularised by the introduction of counterterms.

Counterterms are represented by emulating every Feynman diagram that contains a loop but with $\tilde{\delta}_{n-2}$ replacing the appropriate δ_n; the resulting diagram will lack the loop on account of having fewer legs, and the vertex which would otherwise be associated with the loop represents the counterkernel, $\tilde{F}_{n-2}$.

While constructing these diagrams it is important to remember to maintain momentum conservation throughout; the momentum of the external legs must sum to zero as must the sum of the momenta of ever leg entering a given vertex.

Feynman diagrams are used extensively in Chapters 7, 8, and 9 to represent the power spectra, bispectra, trispectra, and their counterterms that are under consideration in our research.

5.4.2 | Theoretical Errors

We wish to develop an estimator which will allow us to gauge the order of magnitude of the corrections made by each loop order as a function of scale. This is important in the study of perturbation theory; without an understanding of at which scales n-loop effects become

important, we may make estimations for clustering at those scales using only $(n-1)$-loop calculations, which will invariably lead to errors in our predictions. We do this by developing the work presented in [53], in which such an estimator is derived based upon the notion that the only meaningful reference scale in perturbative models of the universe is the non-linear scale, $k_{\rm n}$. Defining all k scalings in terms of this reference scale and remembering that n-loop correlators scale as their respective linear correlators multiplied by k^n, we may estimate the magnitude of loop terms by noting that they will scale as $(k/k_{\rm n})^{3+n_{\rm n}}$, where $n_{\rm n}$ is the slope at the non-linear scale. Thus, we can extrapolate that the theoretical errors for the power spectrum, which will correspond in order of magnitude to their expected values to the perturbative expansion, may be given by:

$$\Delta P_l(k) = P_{11}(k)\left(\frac{k_T}{k_{\rm n}}\right)^{(3+n_{\rm n})l}. \tag{5.72}$$

Expanding upon this, in [53] the following is suggested for the bispectrum error:

$$\Delta B_l(k_1,k_2,k_3) = 3B_{211}(k_1,k_2,k_3)\left(\frac{k_T}{k_{\rm n}}\right)^{(3+n_{\rm n})l}, \tag{5.73}$$

where $k_{\rm T} = (k_1+k_2+k_3)/3$. The spectral slope of the power spectrum at the non-linear wavenumber $k_{\rm n} = 0.3h$ Mpc^{-1} is roughly $n_{\rm n} \approx -3/2$.

Extrapolating from Eq. (5.73), we can generate an estimator for the theoretical error of the trispectrum at l-loops in

$$\Delta T_l(k_1^i,k_2^i,k_3^i,k_4^i) = T_{\rm tree}(k_1^i,k_2^i,k_3^i,k_4^i)\left[\frac{k_{\rm ext}}{k_{\rm n}}\right]^{(3+n_{\rm n})l}. \tag{5.74}$$

5.5 | Summary

In this chapter we have shown how to formulate both SPT and the EFTofLSS to solve the equations of motion presented in Chapter 4 and in doing so describe the statistical distributions of dark matter inhomogeneities. We have discussed the differences between the models, namely the improvements inherent in the EFTofLSS through the incorporation of a cutoff and a non-zero stress-energy tensor.

We have derived the cosmology independent growth factors for the individual contributions to the power series solutions around which both SPT and the EFTofLSS are based and have shown how these allow us to model the Universe as having ΛCDM cosmology, in contrast to the more commonly used approximation in which the Universe is treated as being

an EdS universe. The EdS approximation dramatically simplifies calculations of higher order density fields but introduces a source of potential error as it is not a truly accurate way of estimating the observable $\delta_{\rm n}$; in Chapters 8 and 9, we test the limit of this approximation by comparing perturbative correlators and counterterm constraints using both the EdS approximation and the individually derived n-th order growth factors presented in Chapter 5.3 in our tree level correlators.

We have then discussed how we can use our power series solution for the dark matter density inhomogeneity field $\delta(k^i, \eta)$ to generate correlation functions and how these correlators can be connected to the observable non-linear correlators studied by sky surveys and how these correlators can be represented diagrammatically. Furthermore, given that we are only studying the correlators up to one-loop order in this thesis, the unaccounted for contributions of higher order terms will lead to increasing variance at larger momenta. As such, we have described the method of estimating theoretical errors, whereby we use the notion that the loop corrections scale as a function of their perturbative order and use this to generate curves which should represent the maximal and minimal values the contributions from each order would be expected to hold; by comparing these curves to our calculations, we will be able to determine at what scales it becomes essential to take into account higher order corrections in order to obtain satisfactorally precise results and use this to set limits on the results we obtain in Chapters 7, 8, and 9.

The study of the EFTofLSS will be continued in more detail in Chapters 7, 8, and 9, in which we will explore the perturbative formulations and counterterm corrections to the two, three, and four point correlation functions for dark matter density inhomogeneities, respectively.

6

Numerical Measures of Large Scale Structure

In this chapter we review the various methods used to develop N-body simulations in the field of LSS research before describing GADGET-II, the simulation suite used for this thesis. We then describe how we impose a grid over a timeslice of our simulated volume and use it to measure the correlation functions of the modelled dark matter density perturbations, specifying in detail how various configurations of the bispectrum and trispectrum may be estimated on this grid. We then describe the method of perturbation theory on the grid, a technique which allows the error bars of perturbative models of LSS to be reduced that has been used in prior studies of SPT but, until the research presented in this thesis was published, had not been used in constraints of the EFTofLSS counterterms.

6.1 | N-Body Simulations

Numerical simulations allow us to simulate the fully non-linear dynamics of the universe as accurately as modern technology allows [54]. Of course, modelling the entire observable universe would require computational resources beyond any present day research group; as such, approximations have to be made. Namely, simulations only model a relatively small region of the universe, which is taken to be representative of the whole due to the approximate homegeneity of structure on large scales. These volumes are divided into what are called particles, each representing the centre of mass of a dark matter density inhomogeneity. In order to model cosmological volumes large enough to represent LSS and with enough precision to give robust results, we generally want to use simulations with $\mathcal{O}(10^9)$ such particles [55].

In this subchapter, we will briefly review a number of the most common methods used in cosmological N-body simulations before moving on to discuss GADGET-II, the simulation

used for this thesis, and corrections that can be made to the model in order to improve upon its results.

6.1.1 | N-Body Methods

We will briefly review the most common methods used by N-body simulations in order to provide the background necessary for understanding GADGET-II, which will be described in the next subchapter.

The PP Method

The method of calculating each gravitational interaction between every particle directly and summing the resultant particle velocities is called the Particle-Particle (PP) method [56]. This provides accurate results for small gravitating systems but becomes computationally unfeasible when dealing with cosmological volumes that contain $\mathcal{O}(10^9)$ partices. As such, methods which approximate large numbers of particles as smaller numbers of larger gravitating regions are used to increase efficiency. There are a number of such methods, each with its own advantages and disadvantages, and modern simulations often rely upon hybrid techniques that attempt to maximise the advantages and minimise the disadvantages of their constituent methods.

The Tree Method

A tree code works by modelling objects that are distant from a given body as being a single gravitating object, with the body in question experiencing a single force directed towards the distant group of bodies' centre of mass [57]. Closer objects are modelled on an individual basis with farther objects being more and more merged.

A tree code such as the Barnes-Hut algorithm divides the simulation space into equally sized cubic cells. Each cell is sampled for the presence of dark matter particles; if no particles are present, the cell is disregarded and takes no further place in the calculations. If the cell contains a single particle, it is registered and if the cell contains multiple particles it is divided into equally sized, smaller cubes until each particle is within a cell of its own.

When calculating the forces on a given particle, the particles nearby are sampled individually, emulating the PP method. At greater distances, usually defined as being distances in which the width of the cell is greater than the distance to the centre of mass of the cell from the object in question, the centre of mass of the cell is used without subcells being explicitly studied.

This results in an algorithm that only calculates forces from individual particles over a small fraction of the simulated space and calculates most of the forces involved through the centre of mass approximation. This reduces the number of required calculations by orders of magnitude and results in a significantly faster algorithm than one that simply uses the PP method on all scales.

The PM Method

A particle mesh (PM) code works by dividing the space into cells which are often then divided into further subcells [58]. The particles in each cell have their masses summed to give the a mass to the overall cell and the forces each cell exerts on each other cell is then calculated. Each particle is then treated as having felt the forces that affected the cell it is contained within. This method significantly reduces the required computational resources compared to a PP algorithm and is effective at long range but produces increasingly inaccurate results at increasingly short ranges, making it unsuitable for anything but studies of the very largest scales.

The CIC Method

The Cloud in Cell (CIC) scheme is an improvement upon the PM method which allows each dark matter particle to contribute mass to a number of cells [59]. Rather than a particle's mass simply being added to the mass of the cell it is contained within, if it is located near the boundaries of the cell then a fraction of its mass will be given instead to the nearby cells, the fraction of its mass being aloted to each cell being a function of its proximity to that cell.

The P^3M Method

A Particle-Particle Particle-Mesh (P^3M) algorithm uses a PM on large scales and PP on smaller, sub-mesh scales, combining the computational efficiency of the PM method with the small scale accuracy of the PP method [60]. Such methods are signficantly more accurate than PM algorithms and significantly faster to run than PP algorithms, making them a popular choice for modern N-body simulations.

The TreePM Method

A TreePM algorithm uses PM for long range forces and a tree code for close range forces [61]. The advantage of using the tree method on small scales instead of the PP method is increased computational efficiency; the tree method is significantly faster to run than the

PP method while remaining accurate down to the scales of individual particles. While the PM component of P^3M algorithms significantly speeds up their run time, replacing the PP method with the tree method for the smaller scale calculations speeds it up even more without a significant reduction in the accuracy or precision of the results.

6.1.2 | GADGET II

To generate the data to which our theory could be compared we employed GADGET II [26]. GADGET II is a combined gravitational and hydrodynamical simulation suite. The gravitational aspect of the simulation suite describes collisionless dark matter while the hydrodynamical aspect describes collisional baryonic matter. Throughout the research presented in this thesis, we studied only dark matter, such that the hydrodynamical aspect of the simulation has been unused and will not be mentioned again.

The gravitational aspect of GADGET II describes collisionless dark matter as an ensemble of particles, each representing a large mass of dark matter. The gravitational potential at a point in momentum space k^i will be the sum of the forces from the other particles, given by

$$\phi(k^i) = \sum_i m_i \psi(k^i - k_i^i) \ , \tag{6.1}$$

where the interaction potential ψ is given by the solution of

$$\partial^j \partial_j \psi(k^i) = 4\pi G \left[-\frac{1}{L^3} + \sum_n \tilde{\delta}(k^i - n^i L) \right] \ , \tag{6.2}$$

where the sum over $n^i = (n^1, n^2, n^3)$ covers all integer triplets. The algorithm solves these equations on the principles of a TreePM hybrid N-body simulation code. The large scale PM calculations and the smaller scale tree calculations can be done using different time steppings for increased efficiency, as smaller scale effects require greater precision than is necessary for larger scale effects to obtain the same level of accuracy in the results. As such, the gravitational field at any point is divided into short and long range componeonts, $\phi(k^i) = \phi^l(k^i) + \phi^s(k^i)$ where the long range component is calculated using the PM method and is given by

$$\phi^l(k^i) = \phi(k^i) e^{-k^2 r_s^2} \ , \tag{6.3}$$

where r_s describes the spatial scale of the method splitting, while the short range component is computed using the tree method and is given by

$$\phi^s(k^i) = -\frac{2G}{\sqrt{\pi}} \sum_i \frac{m_i}{r_i} \int_0^{\frac{r_i}{2r_s}} dt e^{-t^2} \ , \tag{6.4}$$

where r_i is the smallest distance from any of the images of particle i to the point k^i.

6.1.3 | Growth Factor Corrections

The time evolution in the simulations has finite precision due to the non-infinitesimal time stepping that any N-body routine must implement. While the time steps are small enough that they can usually be taken to approximate a continuous flow of time, these imprecisions can lead to sub-percent level inaccuracies in the density fields measured at a given timeslice. Due to the subleading nature of loop correction terms, we expect the inaccuracies introduced into them by time-stepping imprecisions to be minimal and do not treat them in this thesis; however, we predict that the inaccuracies introduced into the tree-level terms may be large enough to interfere with the one-loop corrections we are hoping to analyse.

To account for these numerical errors, we introduce corrective terms into our model. These take the form of k^0 corrections which multiply the density fields that contribute to the tree-level correlators and we fit for them as independent parameters of the model, giving us the following non-linear density field up to second order:

$$\delta_{\rm n}(x^i,t) = (1+\Delta D_1)\delta_1(x^i,t) + (1+\Delta D_2)\delta_2(x^i,t)\ . \tag{6.5}$$

These parameters are fitted for alongside the counterterm parameters discussed in Chapter 5. They allow for the fact that the present time $\delta_{\rm n}$ measured in the simulations might be slightly inaccurate and allow for the density fields in the tree level terms to slightly correct their contributions to the perturbative sum to match, allowing the counterterm parameters to be fitted without interference from these inaccuracies.

6.2 | Grid Measurements

Once the simulations have been run, we sample the resulting density fields on a grid of 256^3 cells. Each grid cell is labelled with a momentum space coordinate, allowing us to measure the momentum space correlators between two respective density peaks by sampling their respective cells and accounting for the distances between those cells. Of course, real space is not divided neatly into cubic cells and treating it as though it were would lead to the unrealistic scenario in which all particles within a given cell would contribute their mass wholly to that cell, even if they are located on the border with neighbouring cells. In order to account for this, we impose the Cloud-In-Cell (CIC) mass assignment scheme to the results of our simulation. This distributes the dark matter density field in such a way that each particle can contribute fractions of its mass to neighbouring cells rather than contributing

only to the cell that contains its centre of mass. On this grid, we then measure correlators by averaging the complex products of density fields in spherical shells $i = 1, \ldots, N_{\mathrm{bin}}$ with momentum magnitudes ranging from a chosen $k_{i,\mathrm{min}}$ to a chosen $k_{i,\mathrm{max}}$. We refer to our choices of minimum and maximum momenta for these shells as the momentum binning.

The bispectra of various combinations of fully non-linear and perturbative matter density fields are estimated using the algorithm previously employed in [14]. We are estimating the bispectrum in linearly binned shells in k-space using [62]

$$\hat{B}_{\mathrm{ABC}}(k_i, k_j, k_l) = \frac{V_{\mathrm{f}}}{V_{ijl}} \int_{[q_1^m]_i} \int_{[q_2^m]_j} \int_{[q_3^m]_l} \delta_{\mathrm{A}}(q_1^m) \delta_{\mathrm{B}}(q_2^m) \delta_{\mathrm{C}}(q_3^m) (2\pi)^3 \delta^{(\mathrm{D})}(q_1^m + q_2^m + q_3^m)\,, \tag{6.6}$$

where V_{f} is the volume of the fundamental cell $V_{\mathrm{f}} = (2\pi/L)^3$, A, B and C designate the nature of the density field in question, and The square brackets describe a linear bin (k-space interval) around k_i and

$$V_{ijl} = \int_{[q_1^m]_i} \int_{[q_2^m]_j} \int_{[q_3^m]_l} (2\pi)^3 \delta^{(\mathrm{D})}(q_1^m + q_2^m + q_3^m) \approx \frac{8\pi^2}{(2\pi)^6} k_i k_j k_l \Delta k^3 \tag{6.7}$$

is the volume of the corresponding Fourier-space shell.

The naive implementation of the above estimator would require a pass through all N_{c}^3 cells for each of the N_{c}^3 cells of the grid to ensure the triangle condition, but this quickly becomes unfeasible. By rewriting the delta function in Eq. (6.6) as an integral over plane waves, we may select density field Fourier modes from a shell in k-space, Fourier transform these shells to real space and sum over the product of the Fourier transforms of the three shells. This results in a grid measurement of

$$\begin{aligned}
\hat{B} &= \frac{1}{\mathscr{N}} \int \mathrm{d}^3 x^i \int \frac{\mathrm{d}^3 k_1^i}{(2\pi)^3} \int \frac{\mathrm{d}^3 k_2^i}{(2\pi)^3} \int \frac{\mathrm{d}^3 k_3^i}{(2\pi)^3}\, e^{\mathrm{i} x_j (k_1^j + k_2^j + k_3^j)} \\
&\qquad \times \delta(k_1^i) \delta(k_2^i) \delta(k_3^i) \\
&= \frac{1}{\mathscr{N}} \int \mathrm{d}^3 x^i \int \frac{\mathrm{d}^3 k_1^i}{(2\pi)^3}\, e^{\mathrm{i} x_i k_1^i} \delta(k_1^i) \int \frac{\mathrm{d}^3 k_2^i}{(2\pi)^3}\, e^{\mathrm{i} x_i k_2^i} \delta(k_2^i) \int \frac{\mathrm{d}^3 k_3^i}{(2\pi)^3}\, e^{\mathrm{i} x_i k_3^i} \delta(k_3^i) \\
&\equiv \frac{1}{\mathscr{N}} \int \mathrm{d}^3 x^i\, f_1(x^i) f_2(x^i) f_3(x^i),
\end{aligned} \tag{6.8}$$

where the normalisation factor $\mathscr{N}$ is the volume of the space being integrated over and f is the Fourier transform of δ restricted to a momentum bin. In practice this means setting the field to zero everywhere but in a shell in Fourier space and then Fourier transforming the resulting field and provides a significant improvement in the number of measurements that may be made within a given amount of computer time.

For the trispectrum, studying the full configuration space would be numerically non-trivial and we leave such a study to a future paper. We choose to focus on configurations in which the external four legs are specified and the diagonals are allowed to vary, as this allows us to explore a relatively large fraction of the trispectra's shape spaces without becoming computationally unfeasible. In our CUBA calculations of the SPT contributions to the EFTofLSS, this takes the form of inputting the k-binning of three momenta, integrating over all possible values of the three angles, and calculating the resultant vectors k_1^i, k_2^i, and k_3^i within the integrand. We use these and Eq. (4.52) to calculate k_4^i and its magnitude, k_4. An if-statement then determines whether or not k_4 is within the desired bin; if it is, we calculate the trispectrum with those external leg parameters and add it to the integral; if not, we simply do not. In our analysis on the grid, we rely upon Dirac delta functions and their integral representations to ensure the validity of the configurations. In both cases, the diagonal legs are implicitly integrated over as they are not required to fit into any particular k-bin.

We use a trispectrum estimator, rather than relying upon calculations of the covariance matrix of measured power spectra. Naively, one might try to measure the trispectrum by directly summing density fields in momentum space [63]:

$$\hat{T} = \frac{1}{\mathscr{N}} \int \frac{\mathrm{d}^3 k_1^i}{(2\pi)^3} \int \frac{\mathrm{d}^3 k_2^i}{(2\pi)^3} \int \frac{\mathrm{d}^3 k_3^i}{(2\pi)^3} \int \frac{\mathrm{d}^3 k_4^i}{(2\pi)^3} \, (2\pi)^3 \delta^{(\mathrm{D})}(k_1^i + k_2^i + k_3^i + k_4^i) \times \delta(k_1^i)\delta(k_2^i)\delta(k_3^i)\delta(k_4^i) \tag{6.9}$$

where the integrals run through the appropriate momentum bins for our chosen configurations $|k^i| \in [k_i, k_{i+1}]$. Here we are binning the magnitudes of k_1, k_2, k_3, k_4 and leave the diagonals unconstrained. We hereafter refer to this trispectrum estimator as the direct summation method.

However, this requires studying the entire 3D volume of the sampled space for each of three legs, giving a total of N_c^9 measurements, where N_c is the number of cells per dimension. The Dirac function would then give us k_4^i. This is of course numerically intensive to the point of being unfeasible. Instead, we use the integral representation of the Dirac function to give

us

$$\begin{aligned}\hat{T} &= \frac{1}{\mathscr{N}}\int \mathrm{d}^3x^i \int \frac{\mathrm{d}^3k_1^i}{(2\pi)^3}\int \frac{\mathrm{d}^3k_2^i}{(2\pi)^3}\int \frac{\mathrm{d}^3k_3^i}{(2\pi)^3}\int \frac{\mathrm{d}^3k_4^i}{(2\pi)^3}\, e^{\mathrm{i}x_j(k_1^j+k_2^j+k_3^j+k_4^j)} \\ &\quad\times \delta(k_1^i)\delta(k_2^i)\delta(k_3^i)\delta(k_4^i) \\ &= \frac{1}{\mathscr{N}}\int \mathrm{d}^3x^i \int \frac{\mathrm{d}^3k_1^i}{(2\pi)^3}\, e^{\mathrm{i}x_ik_1^i}\delta(k_1^i)\int \frac{\mathrm{d}^3k_2^i}{(2\pi)^3}\, e^{\mathrm{i}x_ik_2^i}\delta(k_2^i)\int \frac{\mathrm{d}^3k_3^i}{(2\pi)^3}\, e^{\mathrm{i}x_ik_3^i}\delta(k_3^i) \\ &\quad\times \int \frac{\mathrm{d}^3k_4^i}{(2\pi)^3}\, e^{\mathrm{i}x_ik_4^i}\delta(k_4^i) \\ &\equiv \frac{1}{\mathscr{N}}\int \mathrm{d}^3x^i\, f_1(x^i)f_2(x^i)f_3(x^i)f_4(x^i).\end{aligned} \tag{6.10}$$

As was found with the bispectrum, our routine based upon this method works significantly faster than the direct summation routine and allows us to average over the diagonal legs of our configurations with minimal computational cost. In Appendix D we show how this method can be extended to account for configurations with fixed length diagonals.

6.3 | Perturbation Theory on the Grid

To get to the level of precision required to measure the EFTofLSS counterterms on large scales, we need to subtract the leading perturbative orders from the measurements. If perturbation theory is calculated from the loop integrals, the predictions correspond to the infinite volume limit and would require enormous simulation volumes to beat cosmic variance. We choose instead to rely on a modest simulation volume and to beat cosmic variance by evaluating the theory for the very modes used to seed the simulation realisation. This approach has previously been used to test SPT [64, 20, 65], but not to our knowledge been used to constrain the EFTofLSS parameters.

To enact this method, we take advantage of the fact the fact that the recursion relations Eqs. (5.12) and (5.13) for the perturbative density and velocity dispersion fields can be rewritten in terms of configuration space fields as*

$$\begin{aligned}\delta_{\mathrm{n}} = \sum_{m=1}^{n-1}\frac{1}{(2n+3)(n-1)}&[(2n+1)(\theta_m\delta_{\mathrm{n}-m}-\Psi^j_{\theta_m}\partial_j\delta_{\mathrm{n}-m})+ \\ &2(-\Psi^j_{\theta_m}\partial_j\theta_{\mathrm{n}-m}/2-\Psi^j_{\theta_{\mathrm{n}-m}}\partial_j\theta_m/2+K^{ij}_{\theta_m}K^{ij}_{\theta_{\mathrm{n}-m}}+\theta_m\theta_{\mathrm{n}-m}/3)]\end{aligned} \tag{6.11}$$

*Note that in what follows, the velocity divergence is rescaled by $-1/\mathscr{H}f$, such that $\theta_1 \equiv \delta_1$.

and

$$\theta_{\rm n} = \sum_{m=1}^{n-1} \frac{1}{(2n+3)(n-1)} [3(\theta_m \delta_{{\rm n}-m} - \Psi^j_{\theta_m} \partial_j \delta_{{\rm n}-m}) + 2n(-\Psi^j_{\theta_m} \partial_j \theta_{{\rm n}-m}/2 - \Psi^j_{\theta_{{\rm n}-m}} \partial_j \theta_m/2 + K^{ij}_{\theta_m} K^{ij}_{\theta_{{\rm n}-m}} + \theta_m \theta_{{\rm n}-m}/3)] \,. \tag{6.12}$$

Starting from the initial Gaussian field $\delta_1 = \theta_1$, we can use these relations to generate the higher order density fields one-by-one. For numerical efficiency, spatial derivatives and inverse Laplacians are calculated in Fourier space and the fields are then transformed to configuration space where the products are evaluated. This ultimately allows us to measure the perturbative correlators on the same numerical grid used to measure the non-linear fields in a method known as perturbation theory on the grid or gridPT.

The major advantage of working with grid based perturbation theory is that it removes cosmic variance, thus acting as a cosmic variance cancellation (CVC) method. Another issue that the realisation perturbation theory helps with is the dependence of unequal time correlators on the low wavenumber or infrared modes. Equal time correlators do not suffer from this IR-sensitivity [66, 67]. Propagators, such as correlators of the non-linear field with a number of linear fields, are IR-sensitive. Since both the fully non-linear field and perturbation theory share the very infrared modes, this sensitivity is accounted for in gridPT.

We are also implementing the operators $F_{4,\rm UV}, \Gamma$, and E_i at the realisation level in analogy to what has been done in [68] for bias parameters. We have confirmed that their clustering statistics are consistent with the analytical implementation for the counterterms. The parameter fittings obtained in the following chapters are, however, mostly performed with analytical implementations of the counterterms to simplify the error estimation.

6.4 | Summary

In this chapter we have discussed a number of commonly used methods for N-body simulations with a particular focus on the operation of GADGET-II, the simulation suite used throughout the research described in this thesis. We also pointed out that the discretisation of time in N-body simulations introduces a new source of imprecision which will be a function of the scale of the time steps, and propose a modification to our model to correct for this by incorporating new parameters which scale as k^0 and will allow the perturbative density fields to be fitted to the simulated non-linear density fields in spite of these time stepping errors. This method is used in Chapters7 and 8, where we find that it leads to a significant improvement in our ability to calibrate the bispectral counterterms.

We have also described how the results of a simulation can be placed onto a grid and their correlation functions measured. Furthermore, we have described the method of gridPT, whereby perturbation theory is conducted upon the same numerical grid. GridPT allows us to reduce the systematic errors usually associated with fitting a perturbative model to non-linear data as well as providing us with the novel opportunity to study partially non-linear correlators, such as P_{n1}, as was mentioned in Chapter 4 and will be discussed further in Chapters 7, 8, and 9.

7

The Power Spectrum

In this chapter we discuss the estimation of the non-linear power spectrum in the EFTofLSS. In Chapter 7.1 we review existing results on the perturbative descriptions of the terms relevant to understanding the non-linear power spectrum up to one loop order. In Chapter 7.2 we recreate known results regarding the counterterm parameter of the one-loop power spectrum but introduce the original notion of growth factor correction terms, as discussed in Chapter 6.1.3, and discuss how the incorporation of these corrections affects the results of the regularisation. These growth factor dependent results were first published in [27].

7.1 | Perturbation Theory

There are two non-linear power spectra of interest to this analysis, the auto power spectrum $P_{\rm nn}$, and the propagator $P_{\rm n1}$, given by

$$P_{\rm nn} = P_{11} + P_{22} + 2P_{31} + 2P_{\tilde{1}1} \,, \tag{7.1}$$

$$P_{\rm n1} = P_{11} + P_{31} + P_{\tilde{1}1} \,, \tag{7.2}$$

where all power spectra are functions of the magnitude $k = \sqrt{k^i k_i}$ of the wavevector only. Here P_{11} is the linear power spectrum, i.e. the correlator of two Gaussian fields δ_1 and fully describes the initial conditions in the absence of primordial non-Gaussianity. The one-loop contributions are given in perturbation theory by

$$P_{31}(k) = 3P_{11}(k) \int_{q^i} F_3^{(\rm s)}(k^i, q^i, -q^i) P_{11}(q) \,, \tag{7.3}$$

$$P_{22}(k) = 2 \int_{q^i} F_2^{(\rm s)}(k^i - q^i, q^i)^2 P_{11}(|k^i - q^i|) P_{11}(q) \,. \tag{7.4}$$

The term P_{31} is regularised by the counterterm

$$P_{\tilde{1}1} = \tilde{F}_1 P_{11} \,, \tag{7.5}$$

the diagram for which is shown alongside those for P_{11} and the one-loop terms in Fig. 7.1. Following from Eq. (5.46), $\tilde{F}_1 = -c_s^2 k^2$, leaving one free parameter, the speed of sound.

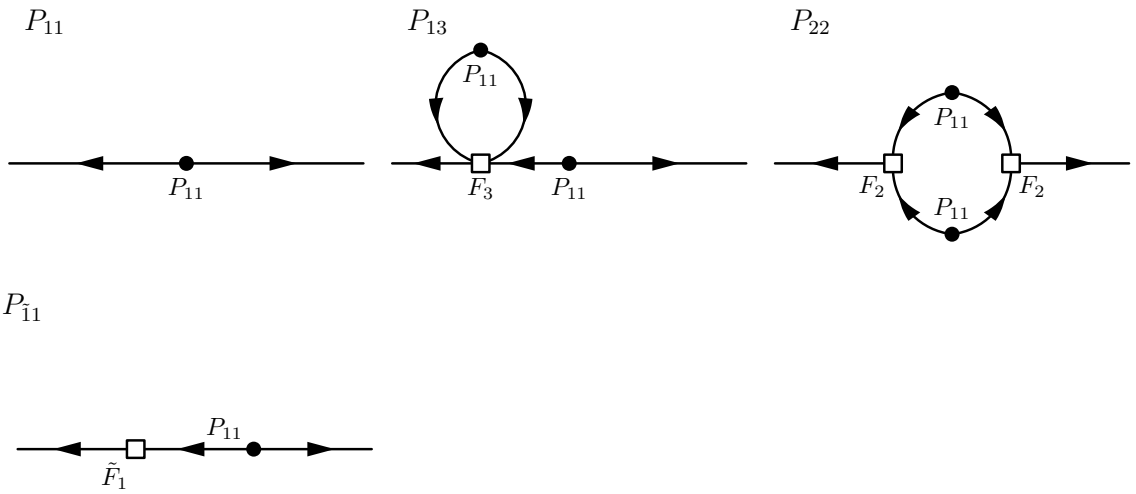

Figure 7.1: Feynman diagram representations of the linear and one-loop contributions to the power spectra of large-scale structure together with the one-loop counterterm $P_{\tilde{1}1}$.

7.1.1 | UV-sensitivity

The P_{31} term in the one-loop matter power spectrum at small external wavenumbers can be expanded as

$$\lim_{q/k\to\infty} P_{31}(k) = -\frac{61}{630} k^2 P_{11}(k) \int_{q^i} \frac{P_{11}(q)}{q^2} = -\frac{61}{210} k^2 P_{11}(k) \sigma_{\rm d}^2 \,, \tag{7.6}$$

where the displacement dispersion $\sigma_{\rm d}^2$ is given by

$$\sigma_{\rm d}^2(\Lambda) = \frac{1}{6\pi^2} \int_0^\Lambda {\rm d}q P_{11}(q) \,. \tag{7.7}$$

This term scales exactly as the counterterm $P_{\tilde{1}1}$, allowing it to be used as an alternative estimator for that counterterm. Due to the fact that Eq. (7.6) differs only from Eq. (7.5) by a constant factor, the regularisation of the propagator term $P_{31} \to P_{31} + P_{\tilde{1}1}$ suggests the

replacement [12]

$$\sigma_{\rm d}^2 \to \sigma_{\rm d}^2 + \frac{210}{61} c_{\rm s}^2 \,. \tag{7.8}$$

For the cosmology considered in this study we have the displacement dispersion of modes up to our cutoff $\sigma_{\rm d}^2(\Lambda = 0.3h\ {\rm Mpc}^{-1}) = 32.9h^{-2}\ {\rm Mpc}^2$. The displacement dispersion of all modes would be $\sigma_{\rm d}^2(\Lambda \to \infty) = 36.56h^{-2}\ {\rm Mpc}^2$. The difference between the two corresponds to the running of the EFTofLSS counterterm amplitude:

$$\Delta c_{\rm s}^2 = \frac{61}{210}\left[\sigma_{\rm d}^2(\Lambda \to \infty) - \sigma_{\rm d}^2(\Lambda = 0.3h\ {\rm Mpc}^{-1})\right] = 1.054h^{-2}\ {\rm Mpc}^2 \,. \tag{7.9}$$

For the calculations made in Chapter 7.2, we will use the UV limit of P_{31} as an estimator for the counterterm $P_{\tilde{1}1}$; in Chapter 8, we test the hypothesis that the one-loop bispectrum counterterms can also be estimated from the UV limit of their corresponding one-loop terms and discuss the results in detail, taking them into account when calibrating the bispectral counterterms.

7.1.2 | ΛCDM Growth Factors

In Fig. 7.2 we reproduce the ΛCDM forms of P_{31} and P_{22} from [19] and compare them to the same terms estimated with the EdS approximation, both through analytic PT and gridPT. We find a good agreement between the analytic and grid perturbative estimators, with both sets of results producing the same ratios of $P_{\rm EdS}/P_{\Lambda{\rm CDM}}$.

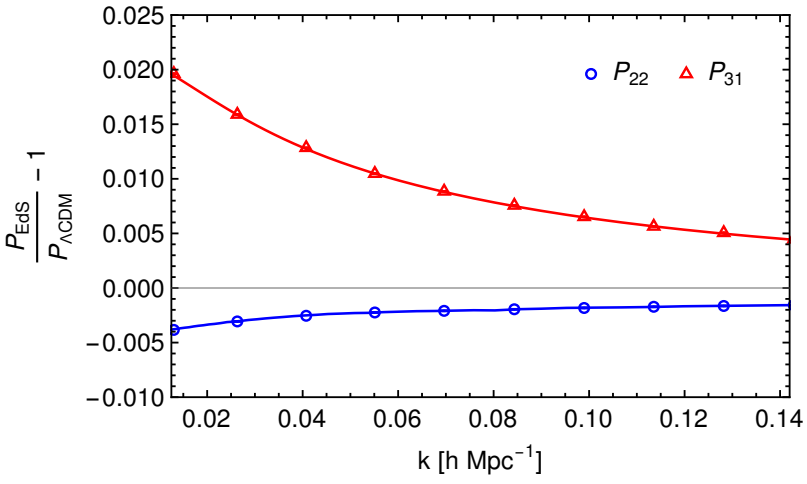

Figure 7.2: The ratio of the power spectrum contributions at one-loop with EdS and ΛCDM growth factors as estimated both through analytic perturbation theory (lines) and gridPT (points). Note that the change in P_{31} leads to a shift in the inferred $c_{\rm s}^2$ as shown in Fig. 7.4.

When estimating the amplitude of the power spectrum counterterm, the 2% corrections to P_{31} leads to a $\Delta c_s^2 = 0.2h^{-2}$ Mpc^2 change in the inferred value of of the one-loop power spectrum counterterm.

7.1.3 | Grid Measurements

In Fig. 7.3 we show the analytic and gridPT calculations of P_{11}, P_{31}, and P_{22}. They consistently estimate the same values as each other on the scale of interest, showing that our implementation of perturbation theory on the grid allows accurate calculations of the perturbative correlators. Given that the gridPT correlators are not only accurate but have the same momentum binning as the measured non-linear correlators that are measured on the same grid, they will allow higher precision counterterm calibrations than standard analytic perturbation theory.

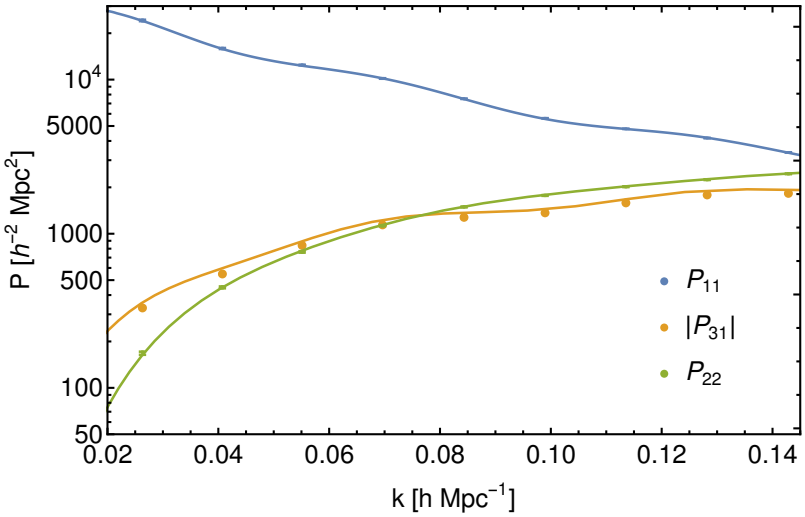

Figure 7.3: The realisation grid based (points) and analytic (lines) calculations of the one-loop power spectrum contributions. As P_{31} is negative, the absolute values are shown. The negigible error bars show the variance of the mean over the fourteen realisations. The agreement is very good at the scales of interest, with the analytic and gridPT calculations consistently overlapping.

7.2 | Parameter Calibration

We will now fit the free parameters of our model by comparing the one-loop perturbative estimator of the power spectrum to the non-linear power spectrum measured in the simulations. We will conduct this at a wide range of k values, but emphasise that our calculations did not

take into account two-loop effects and will therefore only be valid on the scales at which two and higher loop effects are negligible.

7.2.1 | Counterterms

As a first step we present the inference of the power spectrum low-energy constant c_s^2 from the auto power spectrum and propagator. This measurement has been previously presented in [12], but their constraints were based on the EdS assumption. We are measuring the clustering statistics from a numerical simulation. One of the assumptions employed in the discussion so far is that the N-body solver correctly reproduces linear growth in the power spectrum on large scales. If the leading order growth in the simulation were inaccurate, even by a small amount, this would affect our measurements of the one-loop EFTofLSS counterterms. As code comparison studies have shown [69], large-scale linear growth deviations are present due to time stepping and round off errors. To account for the possibility of the leading order linear power spectrum being slightly inaccurate, we allow for a correction term $(1+2\Delta D_1)$ in front of the leading-order P_{11} contribution and fit for the free parameter. The full χ^2 for the auto power spectrum is thus given by

$$\begin{aligned}\chi^2_{\rm nn} = \sum_{k=k_{\rm min}}^{k_{\rm max}} \frac{1}{\Delta P^2_{\rm nn}(k)} \big[P_{\rm nn}(k) - (1+2\Delta D_1)P_{11}(k) \\ -2P_{31}(k) - 2P_{21}(k) - P_{22}(k) + 2c_s^2 k^2 P_{11}(k)\big]^2 \ ,\end{aligned} \tag{7.10}$$

where $\Delta P^2_{\rm nn}(k)$ is the variance of the residual $P_{\rm nn} - 2P_{31} - 2P_{21} - P_{22} - P_{11}$. All the terms in the above equation are evaluated using realisation perturbation theory and so share their initial conditions with the simulations. The variance of the estimator is reduced both due to the subtraction of the odd correlator P_{21} that would vanish in the infinite volume limit and due to the variance in the even correlators like P_{11} that matches the associated terms in $P_{\rm nn}$.

In the propagator we have fixed one of the linear fields that we are cross-correlating with, thus the correction factor reduces to $(1+\Delta D_1)$. To constrain the speed-of-sound from the propagator, we minimise

$$\chi^2_{\rm n1} = \sum_{k=k_{\rm min}}^{k_{\rm max}} \frac{\big[P_{\rm n1}(k) - (1+\Delta D_1)P_{11}(k) - P_{31}(k) - P_{21}(k) + c_s^2 k^2 P_{11}(k)\big]^2}{\Delta P^2_{\rm n1}(k)} \ , \tag{7.11}$$

where $\Delta P^2_{\rm n1}(k)$ is the variance of the residual $P_{\rm n1} - P_{31} - P_{21} - P_{11}$. The two calculations of c_s^2 are shown in Fig. 7.4.

As discussed in detail in [12], the oscillating $k_{\rm max}$ dependence seen in $c_{\rm s}^2$ as calculated from $P_{\rm nn}$ is removed when one takes into account two-loop terms which play a larger role at increasingly small physical scales (higher wavenumbers). The power spectrum and propagator constraints asymptote to the same value on large scales, roughly $k < 0.06h$ Mpc^{-1}, where the one-loop approximation is sufficiently accurate. Note that without CVC, it would have been impossible to constrain the counterterm from our simulations on large scales before the loop corrections become important [12]. In the same figure, we also show the constraints that would have been obtained if we had made the EdS approximation employed in [12]. We see that the inferred value of $c_{\rm s}^2$ is reduced by $\Delta c_{\rm s}^2 = 0.2h^{-2}$ Mpc^2. In Fig. 7.4, we show the counterterm amplitude corresponding to our cutoff $\Lambda = 0.3h$ Mpc^{-1}. According to Eq. (7.9), the extrapolation to infinite cutoff requires a subtraction of $\Delta c_{\rm s}^2 \approx 1h^{-2}$ Mpc^2. Thus we have $c_{\rm s,\infty}^2 = 1.27h^{-2}$ Mpc^2, which is 20% higher than the value reported in [12] due to the ΛCDM corrections which were not considered in that study.

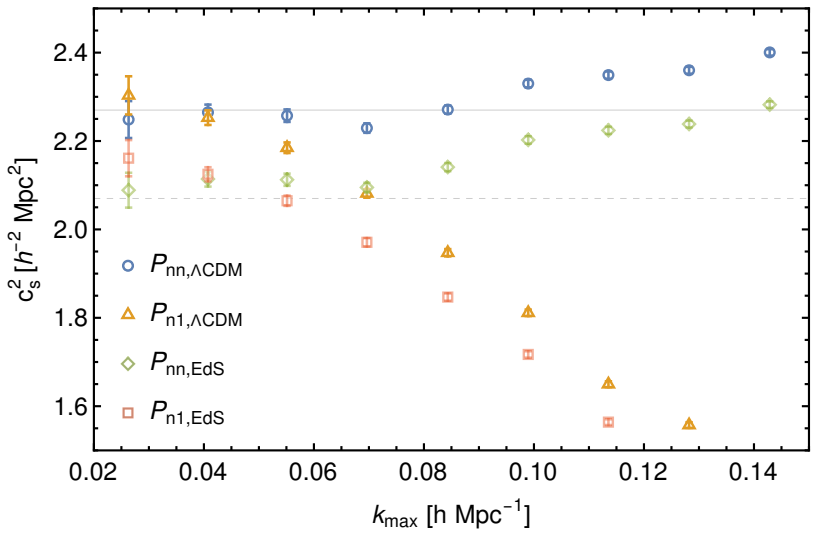

Figure 7.4: The speed-of-sound parameter $c_{\rm s}^2$ as measured from both the non-linear power spectrum $P_{\rm nn}$ and the propagator $P_{\rm n1}$. We show constraints using the EdS approximation for perturbation theory (diamonds and squares) and using the correct ΛCDM growth factors (circles and triangles). The best fit low-energy constant is $c_{\rm s}^2 = 2.27h^{-2}$ Mpc^2 (horizontal line). The difference between P_{31} with exact and EdS growth factors causes a $\Delta c_{\rm s}^2 \approx 0.2h^{-2}$ Mpc^2 shift to the value indicated by the horizontal dashed line. The value shown here is for cutoff $\Lambda = 0.3h$ Mpc^{-1}, and thus needs to be rescaled by Eq. (7.9) for comparison with values reported for $\Lambda \to \infty$. The apparent scale dependence of the counterterms beyond $k \sim 0.05h$ Mpc^{-1} is due to higher order contributions which are not explicitly taken into account in our estimator; for an explicit two-loop calculation of $c_{\rm s}^2$, see [12].

7.2.2 | Growth Factor Corrections

Setting the ΔD_1 terms to zero leads to deviations from the asymptotically flat behaviour of the estimator on large scales. We find that the ΔD_1 constraints themselves asymptote to -2.5×10^{-4} on large scales and start to deviate past $k_{\mathrm{max}} = 0.07h$ Mpc^{-1} similar to the c_{s}^2 constraints. Note that this constraint is specific for our simulations and dependent on settings of the N-body code. The measured values of δD_1 with both ΛCDM and EdS growth factors is shown in Fig. 7.5.

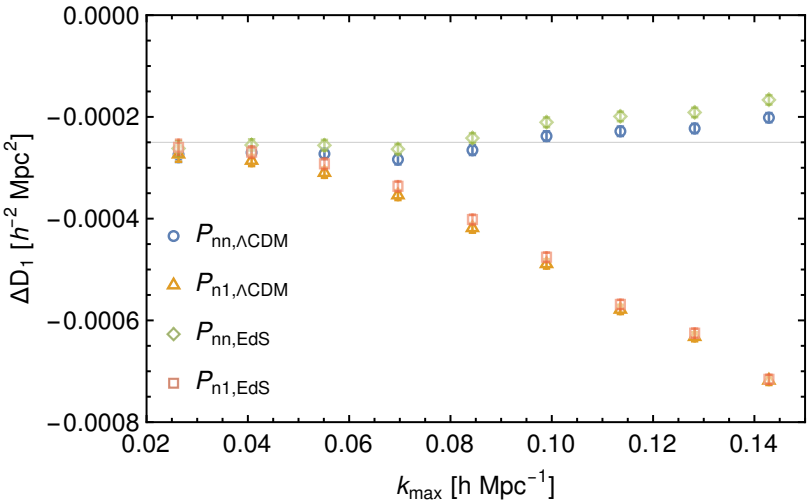

Figure 7.5: The growth factor correction ΔD_1 as calculated from the power spectra with both ΛCDM and EdS growth factors.

7.3 | Summary

In this chapter, we have discussed the power spectrum of dark matter and have calibrated the counterterms necessary to fit the one-loop EFTofLSS power spectrum to the non-linear power spectrum measured from fourteen GADGET-II simulations. We have recreated the result that the UV limit of the one-loop term P_{31} can be used as an estimator for that terms own counterterm, $P_{\tilde{1}1}$ and have calibrated this counterterm using the method of gridPT.

8

The Bispectrum

In this chapter we discuss the non-linear bispectrum in the context of the EFTofLSS. In sections of Chapter 8.1 we review existing results on the perturbative description of the non-linear up to one loop and the relevant counterterms introduced by the stress-energy tensor and in the subsequent sections we present original research that was first published in [27]. Specifically, in Chapter 8.1.2 we discuss the relevance of using ΛCDM growth factors instead of the simpler EdS growth factors for the perturbative density fields and conclude that it is important that ΛCDM growth factors be used for the remainder of the analysis. In Chapter 8.1.3 we estimate the magnitude of the one-loop corrections to the linear bispectrum based upon the methods outlined in Chapter 5.4.2 and show that the measured one-loop contributions from our simulation results fits within these expectated limits. In Chapter 8.2 we discuss and implement a number of procedures to fit the free counterterm parameters of the EFTofLSS to the results of measurements of perturbative bispectra made using the results of a GADGET-II simulation. Following from Chapter 6.1.3, we implement growth factor corrections to account for the time stepping imprecisions inherent to the simulations and demonstrate their importance by comparing results to those obtained without such corrections. Finally, in Chapter 8.3 we place constraints on the counterterms and create a regularised one-loop bispectrum.

8.1 | Perturbation Theory

The bispectrum is the correlator of three fields, $(2\pi)^3\delta^{(\mathrm{D})}(k_1^i+k_2^i+k_3^i)B_{\mathrm{ABC}}(k_1,k_2,k_3) = \langle\delta_A(k_1^i)\delta_B(k_2^i)\delta_C(k_3^i)\rangle$, and vanishes in a Gaussian universe. As such, it intrinsically encapsulates information about cosmic non-Gaussianities. We will be studying three non-linear bispectra: i) the auto bispectrum B_{nnn}, the correlator of three non-linear fields; ii) the propagator B_{n11}, the correlator of one non-linear and two linear fields; and iii) a term which we

informally also refer to as a propagator, B_{n21}, the correlator of a non-linear, a second-order, and a linear field. These can be described perturbatively as:

$$B_{\mathrm{nnn}} = B^{\mathrm{s}}_{211} + B^{\mathrm{s}}_{411} + B^{\mathrm{s}}_{321} + B_{222} + B^{\mathrm{s}}_{\tilde{2}11} + B^{\mathrm{s}}_{\tilde{1}21} \tag{8.1}$$

$$B_{\mathrm{n11}} = B_{211} + B_{411} + B_{\tilde{2}11} \tag{8.2}$$

$$B_{\mathrm{n21}} = B_{321} + B_{\tilde{1}21} \tag{8.3}$$

where all bispectra are functions of (k_1, k_2, k_3) and

$$B_{211}(k_1,k_2,k_3) = 2F_2^{(\mathrm{s})}(k_2^i,k_3^i)P_{11}(k_2)P_{11}(k_3)\ , \tag{8.4}$$

$$B_{411}(k_1,k_2,k_3) = 12\int_{q^i} F_4^{(\mathrm{s})}(q^i,-q^i,-k_2^i,-k_3^i)P_{11}(q)P_{11}(k_2)P_{11}(k_3)\ , \tag{8.5}$$

$$\begin{aligned} B_{321a}(k_1,k_2,k_3) = 6\int_{q^i} & F_3^{(\mathrm{s})}(-q^i,q^i-k_2^i,-k_3^i)F_2^{(\mathrm{s})}(q^i,k_2^i-q^i) \\ & \times P_{11}(q)P_{11}(|k_2^i+q^i|)P_{11}(k_3)\ , \end{aligned} \tag{8.6}$$

$$B_{321b}(k_1,k_2,k_3) = 6\int_{q^i} F_3^{(\mathrm{s})}(q^i,-q^i,k_3^i)F_2^{(\mathrm{s})}(k_2^i,k_3^i)P_{11}(q)P_{11}(k_2)P_{11}(k_3)\ , \tag{8.7}$$

$$\begin{aligned} B_{222}(k_1,k_2,k_3) = 8\int_{q^i} & F_2^{(\mathrm{s})}(-q^i,k_3^i+q^i)F_2^{(\mathrm{s})}(k_2^i-q^i,k_3^i+q^i))F_2^{(\mathrm{s})}(k_2^i-q^i) \\ & \times P_{11}(q)P_{11}(|k_2^i-q^i|)P_{11}(|k_3^i-q^i|)\ , \end{aligned} \tag{8.8}$$

with $B_{321} = B_{321a} + B_{321b}$. These perturbative contributions to the bispectra are represented diagrammatically in Fig. 8.1.

Up to one-loop, two connected three-field correlators can be constructed which include the viscosity terms from the stress-energy tensor:

$$\langle\tilde{\delta}_1(k_1^i)\delta_2(k_2^i)\delta_1(k_1^i)\rangle, \text{ and } \langle\tilde{\delta}_2(k_1^i)\delta_1(k_2^i)\delta_1(k_3^i)\rangle\ , \tag{8.9}$$

which correspond to the bispectra

$$\begin{aligned} B_{\tilde{1}21}(k_1^i,k_2^i,k_3^i;\gamma_1) &= 2F_2(k_1^i,k_3^i)P_{\tilde{1}1}(k_1^i)P_{11}(k_3^i)\ , \\ &= 2\tilde{F}_1(k_1^i;\gamma_1)F_2(k_1^i,k_3^i)P_{11}(k_1^i)P_{11}(k_3^i)\ , \end{aligned} \tag{8.10}$$

$$B_{\tilde{2}11}(k_1^i,k_2^i,k_3^i;\gamma_2,\varepsilon_i) = 2\tilde{F}_2(k_2^i,k_3^i;\gamma_2,\varepsilon_i)P_{11}(k_2^i)P_{11}(k_3^i)\ , \tag{8.11}$$

where $\tilde{F}_1$ and $\tilde{F}_2$ are defined in Eqs. (5.46) and (5.47), respectively.

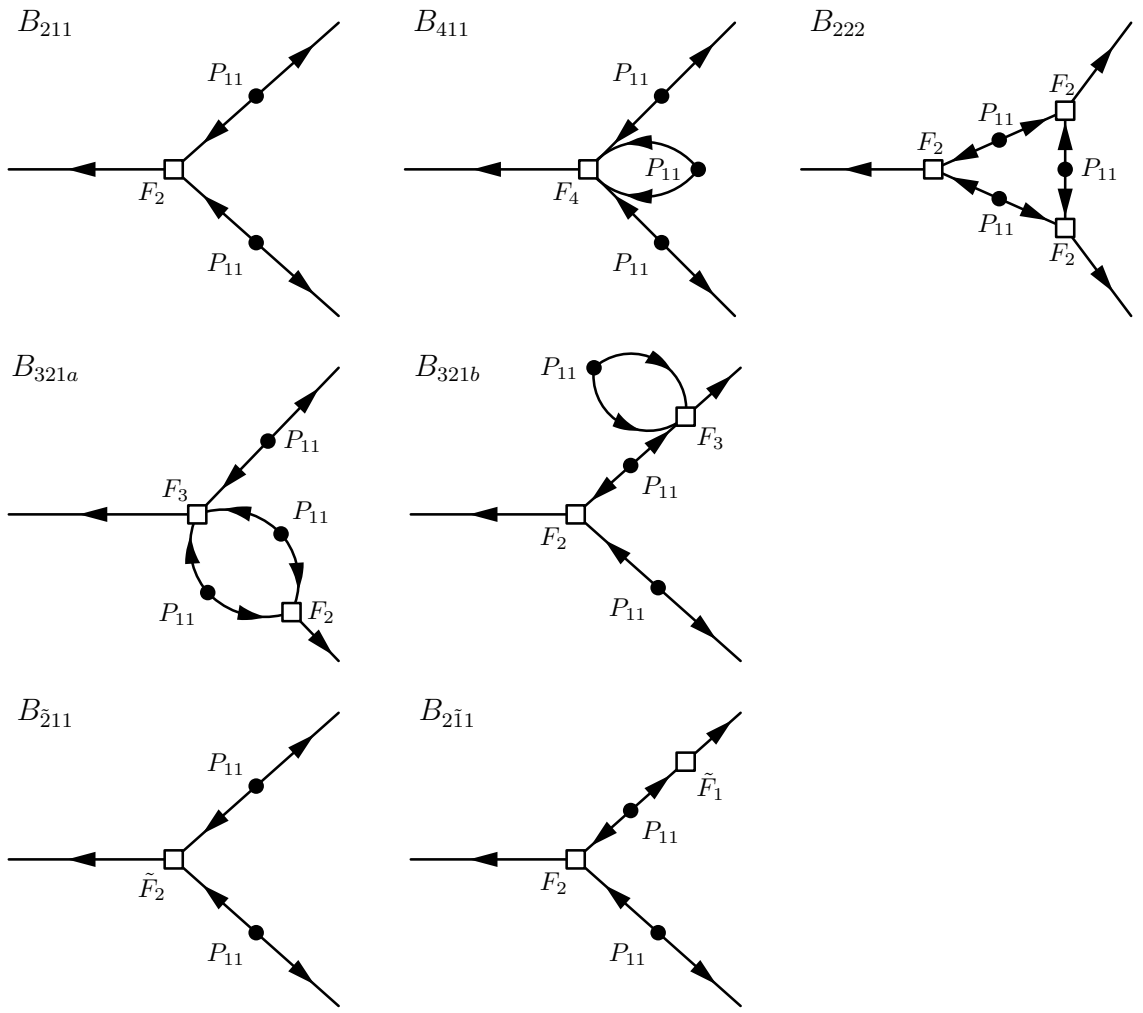

Figure 8.1: Feynman diagram representations of the contributions to the tree-level and one-loop bispectrum together with the one-loop counterterms.

For the auto bispectrum, B_{nnn}, we symmetrise over the permutations*

$$B^{\text{s}}_{211}(k_1,k_2,k_3) = B_{211}(k_1,k_2,k_3) + 2 \text{ permutations} , \tag{8.12}$$

$$B^{\text{s}}_{411}(k_1,k_2,k_3) = B_{411}(k_1,k_2,k_3) + 2 \text{ permutations} , \tag{8.13}$$

$$B^{\text{s}}_{321}(k_1,k_2,k_3) = B_{321}(k_1,k_2,k_3) + 5 \text{ permutations} , \tag{8.14}$$

$$B^{\text{s}}_{\tilde{2}11}(k_1,k_2,k_3) = B_{\tilde{2}11}(k_1,k_2,k_3) + 2 \text{ permutations} , \tag{8.15}$$

$$B^{\text{s}}_{\tilde{1}21}(k_1,k_2,k_3) = B_{\tilde{1}21}(k_1,k_2,k_3) + 5 \text{ permutations} . \tag{8.16}$$

*Cyclic permutations are given by $[\{k_1,k_2,k_3\},\{k_2,k_3,k_1\},\{k_3,k_1,k_2\}]$ and all permutations by $[\{k_1,k_2,k_3\},\{k_2,k_3,k_1\},\{k_3,k_1,k_2\},\{k_2,k_1,k_3\},\{k_1,k_3,k_2\},\{k_3,k_2,k_1\}]$.

To retain the configuration dependence we do not perform a symmetrisation for $B_{\rm n11}$ and $B_{\rm n21}$ or their perturbative contributions.

8.1.1 | UV-sensitivity

The bispectrum term $B_{321,b}$, defined in Eq. (8.7), can be written in terms of P_{31} as

$$B_{321,b}(k_1^i,k_2^i) = 2F_2^{(\rm s)}(k_1^i,k_2^i)P_{31}(k_1)P_{11}(k_2)\,. \tag{8.17}$$

In analogy to Eq. (7.6), this leads to the UV-limit

$$\begin{aligned} B_{321,\rm UV}(k_1^i,k_2^i) &\equiv \lim_{q/k\to\infty} B_{321,b}(k_1^i,k_2^i) \\ &= -2\frac{61}{210}k_1^2\sigma_{\rm d}^2 F_2^{(\rm s)}(k_1^i,k_2^i)P_{11}(k_1)P_{11}(k_2) \\ &= -\frac{61}{210}k_1^2\sigma_{\rm d}^2 B_{211}(k_1^i,k_2^i)\,, \end{aligned} \tag{8.18}$$

based on which we can suggest the UV ansatz for the counterterm

$$\begin{aligned} B_{\tilde{1}21,\rm UV}(k_1^i,k_2^i;\gamma_1) &\equiv -2\gamma_1 k_1^2 F_2(k_1^i,k_2^i)P_{11}(k_1)P_{11}(k_2) \\ &= -\gamma_1 k_1^2 B_{211}(k_1^i,k_2^i)\,, \end{aligned} \tag{8.19}$$

where the fact that we are simply taking the UV-limit of F_3 as we did for P_{31} means that we expect this γ_1 to be identical to $c_{\rm s}^2$ from the power spectrum. Thus the UV inspired ansatz agrees with the full symmetry inspired counterterm, $F_{3,\rm UV} = \tilde{F}_1$. The contribution from B_{411} has a strong UV-sensitivity that is given by the limit of the F_4 kernel,

$$\int \frac{{\rm d}\Omega_{q^i}}{4\pi} \lim_{q/k\to\infty} F_4(k_1^i,k_2^i,q^i,-q^i) = \frac{1}{18q^2}F_{4,\rm UV}(k_1^i,k_2^i)\,, \tag{8.20}$$

giving us

$$\begin{aligned} B_{411,\rm UV}(k_1^i,k_2^i) = \lim_{q/k\to\infty} B_{411}(k_1^i,k_2^i) &= 2F_{4,\rm UV}(k_1^i,k_2^i)P(k_1)P(k_2)\frac{1}{3}\int_{q^i}\frac{P(q)}{q^2} \\ &= 2\sigma_{\rm d}^2 F_{4,\rm UV}(k_1^i,k_2^i)P(k_1)P(k_2)\,, \end{aligned} \tag{8.21}$$

with [14]

$$F_{4,\mathrm{UV}}(k_1^i,k_2^i) = -\frac{9552}{18865}(k_1^2+k_2^2)\mu_{12}^2 - \frac{61}{420}\mu_{12}\left(\frac{k_2^3}{k_1}+\frac{k_1^3}{k_2}\right) \\ -\frac{12409\mu_{12}^3 k_1 k_2}{56595} - \frac{115739\mu_{12}k_1k_2}{113190} - \frac{4901}{18865}(k_1^2+k_2^2)\,. \tag{8.22}$$

Together with Eq. (7.8), this suggests the UV-ansatz

$$B_{\tilde{2}11,\mathrm{UV}}(k_1^i,k_2^i;\gamma_2) = 2\frac{210}{61}\gamma_2 F_{4,\mathrm{UV}}(k_1^i,k_2^i)P(k_1)P(k_2)\,. \tag{8.23}$$

If we were to focus entirely upon the stress-energy tensor inspired by symmetry and ignore these UV limits, we would treat γ_2, ε_1, ε_2, and ε_3 in Eq. (5.47) as four independent parameters. Alternatively, we could fix the ratio of the parameters to match the above UV-limit of F_4 and approximate $\tilde{F}_2 \approx 210/61\ F_{4,\mathrm{UV}}$ by setting [14]

$$\varepsilon_1 = \frac{3466}{14091}\gamma_2,\ \ \varepsilon_2 = \frac{7285}{32879}\gamma_2,\ \ \varepsilon_3 = \frac{41982}{32879}\gamma_2\,. \tag{8.24}$$

We will consider both the UV inspired and the more general symmetry motivated counterterm parametrisations in our constraints to follow.

8.1.2 | ΛCDM Growth Factors

While in the power spectrum the leading order term is unaffected by changes in growth factor due to its containing only the linear δ_1, for the bispectrum the tree-level result is affected by the ΛCDM corrections to δ_2. These corrections to the tree-level bispectrum can be encoded by the second order gravitational coupling kernel

$$F_{2,\Lambda\mathrm{CDM}}(k_1^i,k_2^i) = \frac{5}{7}\frac{D_{2A}(a)}{D_1^2(a)}\alpha(k_1^i,k_2^i) + \frac{2}{7}\frac{D_{2B}(a)}{D_1^2(a)}\beta(k_1^i,k_2^i)\,. \tag{8.25}$$

For the cosmology under consideration we have at $z=0$ that $D_{2A}(a)/D_1^2(a)-1 \approx 2.7\times10^{-3}$ and $D_{2B}(a)/D_1^2(a)-1 \approx -7\times10^{-3}$. As can be seen in the right panel of Fig. 8.2, the difference between the EdS and ΛCDM tree-level bispectra exceeds the amplitude of the one-loop bispectrum contribution from B_{411} for $k < 0.02h\ \mathrm{Mpc}^{-1}$ and the typical size of the EFTofLSS counterterms from $B_{\tilde{2}11}$ for $k < 0.08h\ \mathrm{Mpc}^{-1}$. The data points show that our grid implementation of the ΛCDM second order density field agrees with the analytical calculation. We thus implemented the exact ΛCDM versions of the F_2 and F_3 kernels on the grid and will be using them throughout this study. The details of this implementation are

discussed below in Eqs. (5.48) and (5.56). We have validated that the grid implementations of the kernels with the correct growth factors do indeed reproduce the expected deviations from the EdS approximation in the power and bispectrum, as shown in Fig. 8.3. In the left panel we can see that while the corrections for the B_{211} and B_{222} terms are of order 0.5%, the corrections around the zero crossing of the combined B_{321} term are significant.

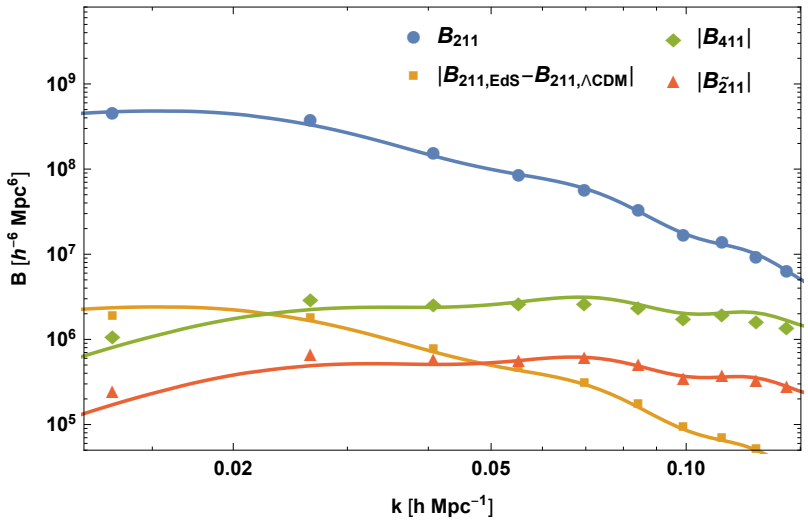

Figure 8.2: Equilateral bispectrum contributions to the propagator $B_{\mathrm{n}11}$. The difference between the EdS and ΛCDM tree-level bispectra (orange) exceeds the amplitude of the one-loop bispectrum contribution from B_{411} for $k < 0.02h$ Mpc^{-1} and the typical size of the EFTofLSS counterterms from $B_{\tilde{2}11}$ for $k < 0.08h$ Mpc^{-1}. The orange data points show that our grid implementation of the ΛCDM second order density field agrees with the analytical calculation.

Based on results for the one-loop power spectrum [19, 67] in ΛCDM, and the above results, it seems plausible to expect $< 1\%$ corrections for the one-loop bispectrum as well. This makes these corrections typically a factor of 10 smaller than the expected counterterms, such that we can ignore the ΛCDM corrections for the one-loop contributions. When pushing the accuracy to the next loop order, i.e. the two-loop bispectrum, these corrections might indeed matter. We will thus evaluate the exact ΛCDM tree level bispectrum, but use the EdS approximation in the one-loop power spectrum and leave the study of the full one-loop ΛCDM bispectrum for future work.

8.1.3 | Grid Measurements

In Fig. 8.4 we show a comparison of analytic perturbation theory calculated using the CUBA Vegas numerical integrator and grid calculations of the contributions to the tree-level and one-

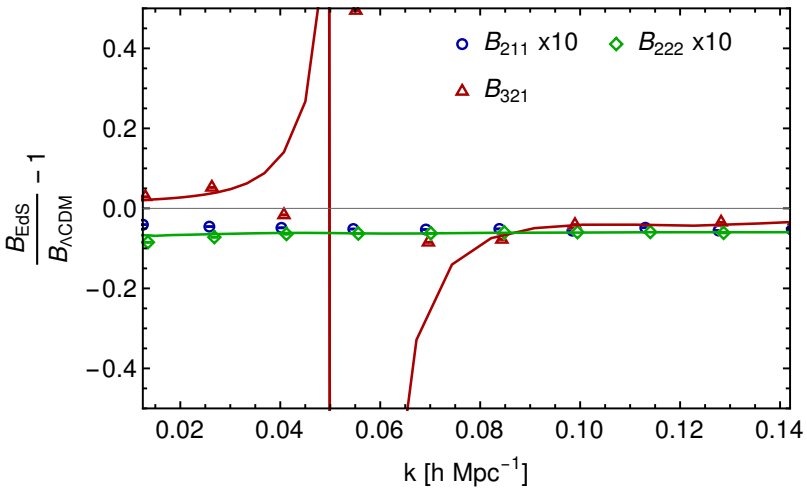

Figure 8.3: Ratio of the bispectrum contributions up to one-loop in the equilateral configuration with EdS and ΛCDM growth factors, where the relative deviation of B_{211} and B_{222} has been multiplied by ten to improve visibility. The pole is due to the sign-change of the sum of the two contributions, B_{321a} and B_{321b}.

loop bispectrum. We find good agreement on all but the largest scales, where the discreteness of the simulation modes leads to minor deviations from the continuous loop calculations.

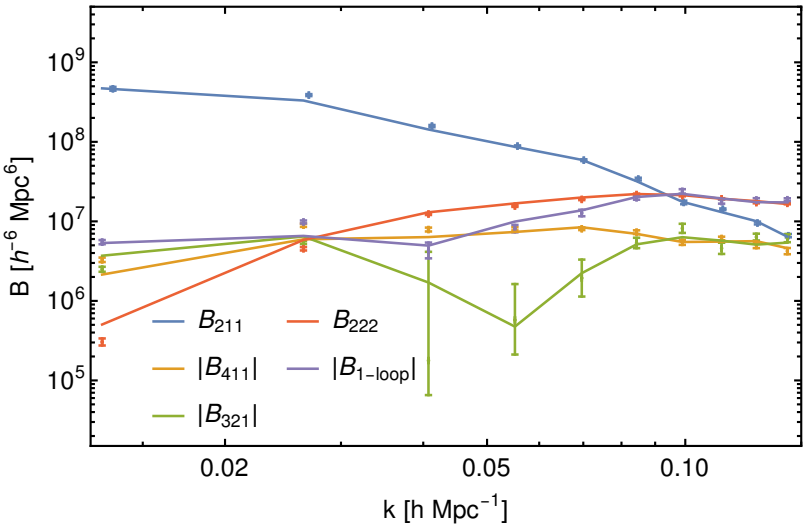

Figure 8.4: The realisation grid based (points) and analytic (lines) calculations of the one-loop bispectrum contributions together with their sum. As B_{411} and parts of B_{321} and $B_{1-\mathrm{loop}}$ are negative, the absolute values are shown. The error bars show the variance of the mean over the fourteen realisations. The agreement is very good with some small deviations on large scales due to the finite bin width and discrete nature of large-scale modes.

8.1.4 | Theoretical Errors

Figure 8.5 shows the extent of the two loop theoretical errors in the bispectrum. We can see that two loop effects become significant at about $k \sim 0.07$, so it is at roughly this momentum that we shall take our calibrations.

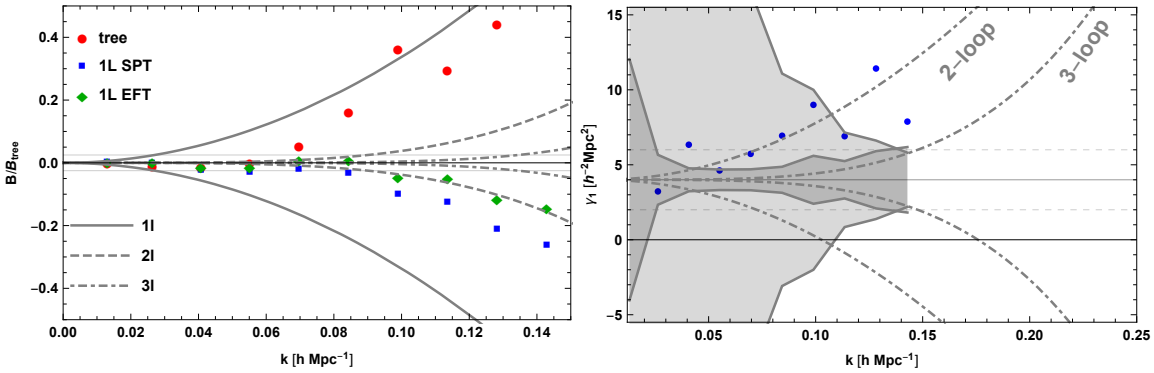

Figure 8.5: *Left panel:* Ratio of the residual bispectra and the tree-level bispectrum in the equilateral configuration. We show the difference between non-linear bispectrum and tree-level (red), one-loop SPT (blue), and one-loop EFTofLSS (green). We overplot the theoretical errors defined in Eq. (5.73). We see that the one-loop theoretical error (solid grey) does indeed form an appropriate envelope for the residual corrections once the tree-level prediction has been subtracted from the data. *Right panel:* Scale dependence of the bispectrum counterterm amplitude γ_2 in the equilateral configuration. We show the statistical errors without CVC (light shaded) and with CVC (dark shaded). Only with CVC can we get close to the true large scale limit before the theoretical error bars induced by two-loop terms take over. The scale dependence of the inferred counterterms arises from the fact that at whichever order they are estimated, higher order effects are not taken into account and these effects will play an increasingly large role on smaller physical scales.

8.2 | Fitting Procedures

We employ a number of procedures for calculating the parameters that go into the counterkernel calculations. Firstly, we decide upon a bispectrum contribution from which to do the calculations:

B_{nnn}. Employing the full non-linear bispectrum, we minimise

$$\begin{aligned}\chi^2_{\mathrm{nnn}}(k_{\mathrm{max}}) = \sum_{k_{1,2,3}=k_{\mathrm{min}}}^{k_{\mathrm{max}}} & \frac{1}{\Delta B^2_{\mathrm{nnn}}(k_1,k_2,k_3)} \\ & \times \Big[B_{\mathrm{nnn}}(k_1,k_2,k_3) - B^{\mathrm{s}}_{\mathrm{SPT}}(k_1,k_2,k_3;\Delta D_1,\Delta D_2) \\ & - B^{\mathrm{s}}_{\tilde{2}11}(k_1,k_2,k_3;\gamma_2,\varepsilon_i) - B^{\mathrm{s}}_{\tilde{1}21}(k_1,k_2,k_3;\gamma_1)\Big]^2\end{aligned} \tag{8.26}$$

with respect to γ_1, γ_2, ε_1, ε_2, ε_3, and the growth factor corrections ΔD_1 and ΔD_2, where

$$\begin{aligned}B^{\mathrm{s}}_{\mathrm{SPT}} = (1+3\Delta D_1)B^{\mathrm{s}}_{111} + (1+2\Delta D_1+\Delta D_2)B^{\mathrm{s}}_{211} + (1+2\Delta D_1)B^{\mathrm{s}}_{311} \\ +(1+2\Delta D_1)B^{\mathrm{s}}_{411} + (1+\Delta D_1+2\Delta D_2)B^{\mathrm{s}}_{221} \\ +(1+\Delta D_1+\Delta D_2)B^{\mathrm{s}}_{321} + (1+3\Delta D_2)B^{\mathrm{s}}_{222}\,.\end{aligned} \tag{8.27}$$

The terms on the right hand side of Eq. (8.26) are symmetrised with respect to their external momenta.

B_{n11}. Employing the bispectrum propagator, we minimise

$$\begin{aligned}\chi^2_{\mathrm{n11}}(k_{\mathrm{max}}) = \sum_{k_{1,2,3}=k_{\mathrm{min}}}^{k_{\mathrm{max}}} & \frac{1}{\Delta B^2_{\mathrm{n11}}(k_1,k_2,k_3)} \left[B_{\mathrm{n11}}(k_1,k_2,k_3)\right. \\ & \left. -B_{\mathrm{SPT}}(k_1,k_2,k_3;\Delta D_1,\Delta D_2) - B_{\tilde{2}11}(k_1,k_2,k_3;\gamma_2,\varepsilon_i)\right]^2,\end{aligned} \tag{8.28}$$

where

$$B_{\mathrm{SPT}} = (1+\Delta D_1)B_{111} + (1+\Delta D_2)B_{211} + B_{311} + B_{411}\,, \tag{8.29}$$

with respect to γ_2, ε_1, ε_2, ε_3. The terms on the right hand side of Eq. (8.28) are not symmetrised with respect to their external momenta.

B_{n21}. Employing our second propagator, we minimise

$$\begin{aligned}\chi^2_{\mathrm{n21}}(k_{\mathrm{max}}) = \sum_{k_{1,2,3}=k_{\mathrm{min}}}^{k_{\mathrm{max}}} & \frac{1}{\Delta B^2_{\mathrm{n21}}(k_1,k_2,k_3)} \left[B_{\mathrm{n21}}(k_1,k_2,k_3)\right. \\ & \left. -B_{\mathrm{SPT}}(k_1,k_2,k_3;\Delta D_1,\Delta D_2) - B_{\tilde{1}21}(k_1,k_2,k_3;\gamma_1)\right]^2\end{aligned} \tag{8.30}$$

with respect to γ_1, where

$$B_{\mathrm{SPT}} = (1+\Delta D_1)B_{121} + (1+\Delta D_2)B_{221} + B_{321}\,. \tag{8.31}$$

The terms on the right hand side of Eq. (8.30) are not symmetrised with respect to their external momenta.

These functions can be differentiated with respect to the counterparameters γ_1, γ_2, ε_1, ε_2, ε_3 to give linear functions of said parameters. This makes constraining the parameters by finding the minima of the χ^2 functions a simple case of solving a system of linear equations.

Ordinarily, the errors in the denominators of Equations (8.26), (8.28), and (8.30) would be the variance of the non-linear bispectrum and the SPT would be analytically calculated through perturbation theory. However, we make use of gridPT such that the SPT components subtracted from the non-linear bispectrum come from perturbation theory on the grid and the denominator is the variance of the ensuing residual. This will reduce the overall variance of the measured parameters as it will remove the variance induced by the individual perturbative contributions to the non-linear bispectrum without affecting the measurements' abilities to constrain the counterparameters.

In addition to choosing which non-linear bispectrum to study, we can define the following fitting procedures to constrain γ_1 and γ_2:

1. Fitting for a joint EFTofLSS parameter γ after setting $\gamma_1 = \gamma_2$.
2. Fitting $\gamma_1 = c_s^2$ from the power spectrum and using this value in the counterterm $B_{\tilde{1}21}$ while fitting independently for γ_2 in $B_{\tilde{2}11}$.
3. Fitting for γ_1 and γ_2 independently.
4. Replacing the analytic counterterms with grid implementations of the counterterms $B_{\tilde{2}11,\mathrm{UV}}$ defined in Eq. (8.23) and $B_{\tilde{1}21,\mathrm{UV}}$ Eq. (8.19) and fitting for the contained γ_1 and γ_2.
5. Replacing the analytic counterterms with grid implementations of the counterterms $B_{\tilde{2}11,\mathrm{UV}}$ defined in Eq. (8.23) and $B_{\tilde{1}21,\mathrm{UV}}$ Eq. (8.19) and fitting for a joint γ after setting $\gamma_1 = \gamma_2$.

With fittings $1-3$ for γ_2 we can then we can use the following parametrisations for the ε parameters:

U. Inspired by UV sensitivity such that we assume $F_{4,\mathrm{UV}} \approx \frac{61}{210}\tilde{F}_2$, we can use the definitions given in Equations (8.24) and fit $B_{\tilde{2}11}$ only for γ_2 [14].

S. Inspired by symmetries, we can fit $B_{\tilde{2}11}$ for all four of its free parameters independently.

This provides us with a wide range of methods with which to constrain the same parameters, allowing us to cross-check the results and to compare the different procedures and comment upon their respective accuracies with reference to their assumptions. Inclusion of a free ε_1 parameter in Eqs. (8.26) and (8.28) results in all parameters being heavily degenerate at most values of $k_{\rm max}$, as can be quantified from the Fisher matrices of the χ^2 functions (see Appendix B). For this reason, for the remainder of the analysis, the UV inspired parametrisations remain unchanged while the symmetry inspired parametrisations only minimise for γ_1, γ_2, ε_2, and ε_3, with ε_1 set to zero.

8.2.1 | Propagator Terms

Using the propagator terms, we are able to calculate γ_2 and γ_1 in isolation and compare these results to those we obtain when studying them simultaneously in the auto bispectrum below. In the case of γ_2, we did this with both the UV inspired and symmetry inspired parametrisations. Naturally, for the propagator terms we are limited to methods 3 and 4 owing to the isolated nature of the γ parameters.

In Fig. 8.6 we compare the propagator measurements of γ_1 with both UV and symmetry inspired parametrisations for both suggested values of m, as well as with both CVC and without. These show that there are small but not negligible differences between the values obtained with different values of m and that CVC greatly reduces the error bars of the measurements. The UV inspired parametrisation replicate the UV limit of the one-loop terms when $m = 1$ and the symmetry inspired model represents the symmetries of the EFTofLSS irrespective of m. Given that there was a measurable difference between the constraints made with the two choices of m, albeit a small one, we have elected to perform all future calculations in the propagator with $m = 1$ for UV inspired fittings and $m = 5/3$ for symmetry inspired fittings, and in all cases we introduce CVC.

For the growth factor corrections with the propagators, we find $\Delta D_1 \approx -0.003$ and $\Delta D_2 \approx 0.005$ on large scales. The ΔD_1 constraint seems larger than the one obtained from the power spectrum above, but it has to be noted that it comes primarily from the noise term B_{111}. In App. C we validate our fitting procedure on the difference of B_{411} evaluated on the grid for two different cutoffs. By definition this reference field can be fit by the UV-parametrisation of $B_{\tilde{2}11}$, but we also checked its ability to recover the full symmetry inspired parametrisation.

8.2.2 | Auto Bispectrum

Using the full bispectrum $\chi^2_{\rm nnn}$, we are able to calculate γ_1 and γ_2 together, or equate them and calculate a joint γ. As we did for the propagator, we will begin by assessing the importance

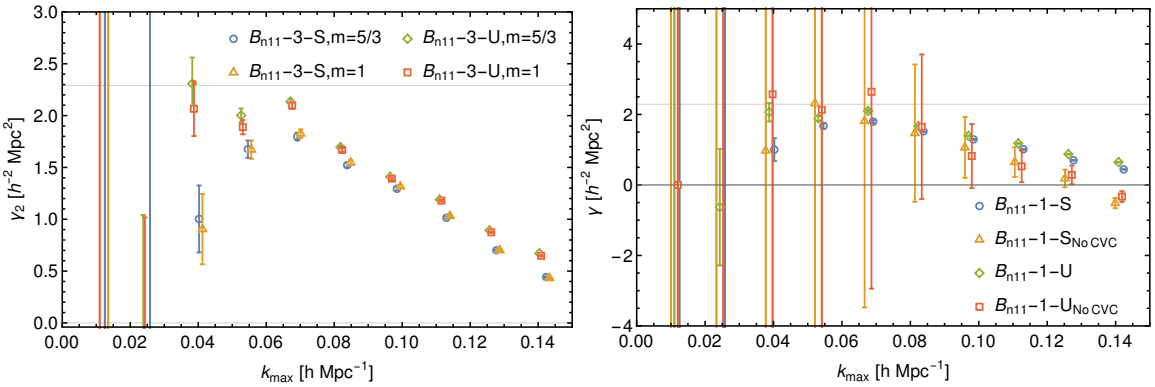

Figure 8.6: *Left panel:* Constraints on γ_2 from $B_{\rm n11}$ with both symmetry and UV inspired parametrisations for both suggested values of the parameter m. The differences are at the percent level; small, particularly compared to the corrections and errors we would expect from other factors such as the unmodelled contribution of the higher loop terms, but non-zero, such that for the remainder of the study of the propagator we set $m = 1$ for the UV inspired parametrisation and $m = 5/3$ for the symmetry inspired parametrisation. Note that on large scales the measurements asymptote to the power spectrum $c_{\rm s}^2$ measurement shown by the horizontal line. *Right panel:* Constraints on γ_2 from $B_{\rm n11}$ with both symmetry and UV inspired parametrisations with and without cosmic variance cancellation. In the non-CVC calculations, we continued to use the residuals with subtracted grid perturbation theory and removed CVC only from the variance in the denominator of the χ^2 to avoid issues with IR sensitivities of the propagator that are resolved by the subtraction of grid PT from the measured bispectrum propagator. The results without CVC clearly show significantly larger error bars than those without.

of CVC, the choice of the value of m, and of our decision to use ΛCDM growth factors for δ_2 and δ_3 instead of the more commonly used EdS approximation. The effects of incorporating cosmic variance cancellation into the denominator of the χ^2 for the full bispectrum are shown in the right hand panel of Fig. 8.9. We see that the error bars are significantly reduced in size, as they were for the propagator. As such, we use CVC in all future fittings of the auto bispectrum. In the left hand panel of the same figure we compare the $B_{\rm nnn}$-1 fitting for both UV and symmetry inspired parametrisations for both $m = 5/3$ and $m = 1$. While the differences between measurements with different values of m are small, they are non-zero, and we choose to set $m = 1$ when studying the UV inspired parametrisation and $m = 5/3$ when studying the symmetry inspired parametrisations, as we did for the propagator.

The calculated joint γ from $B_{\rm nnn}$-1-S and $B_{\rm nnn}$-1-U are plotted in Fig. 8.10 with both EdS and ΛCDM growth factors for δ_2 and δ_3. As can clearly be seen, the EdS results deviate quite significantly from the more accurate ΛCDM results. As such, it is clear that the use of ΛCDM growth factors is essential for high precision regularisation of the one-loop bispectrum.

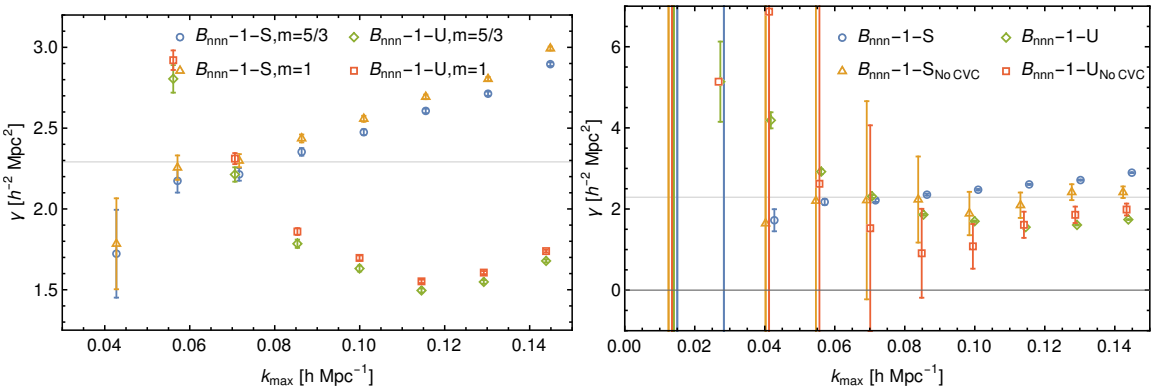

Figure 8.7: *Left panel:* Constraints on a joint γ from the auto bispectrum with both symmetry and UV inspired parametrisations for both suggested values of the parameter m. As with the propagator, the differences are at the percent level. We set $m = 1$ for the UV inspired studies of the auto bispectrum and $m = 5/3$ for the symmetry inspired studies. *Right panel:* Constraints on the joint γ from $B_{\rm nnn}$ with both symmetry and UV inspired parametrisations with and without cosmic variance cancellation. In the non-CVC case, we continued to use the residual with subtracted grid PT contributions and only changed the variance in the denominator, to avoid issues with IR divergences. The results without CVC clearly show larger error bars than those without.

For the growth factor corrections with the auto bispectrum, we again find that $\Delta D_1 \approx -0.003$ and $\Delta D_2 \approx 0.005$ on large scales. However, the corrections begin to deviate strongly from those of the propagator at $k \sim 0.07h$ Mpc^{-1}.

Using the full bispectrum $\chi^2_{\rm nnn}$, we are able to calculate γ_1 and γ_2 together, or equate them and calculate a joint γ. As we did for the propagator, we will begin by assessing the importance of CVC, the choice of the value of m, and of our decision to use ΛCDM growth factors for δ_2 and δ_3 instead of the more commonly used EdS approximation. The effects of incorporating cosmic variance cancellation into the denominator of the χ^2 for the full bispectrum are shown in the right hand panel of Fig. 8.9. We see that the error bars are significantly reduced in size, as they were for the propagator. As such, we use CVC in all future fittings of the auto bispectrum. In the left hand panel of the same figure we compare the $B_{\rm nnn}$-1 fitting for both UV and symmetry inspired parametrisations for both $m = 5/3$ and $m = 1$. While the differences between measurements with different values of m are small, they are non-zero, and we choose to set $m = 1$ when studying the UV inspired parametrisation and $m = 5/3$ when studying the symmetry inspired parametrisations, as we did for the propagator.

The calculated joint γ from $B_{\rm nnn}$-1-S and $B_{\rm nnn}$-1-U are plotted in Fig. 8.10 with both EdS and ΛCDM growth factors for δ_2 and δ_3. As can clearly be seen, the EdS results deviate quite

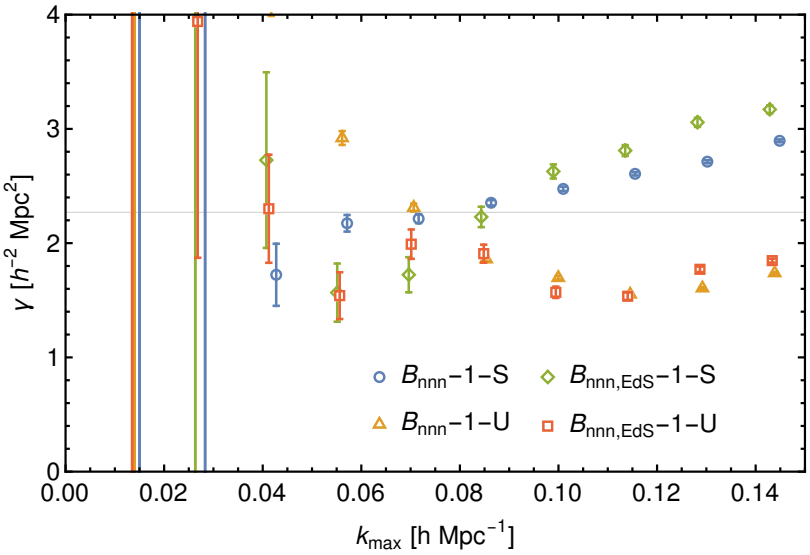

Figure 8.8: The joint γ as calculated from the auto bispectrum using methods $B_{\rm nnn}$-1-S and $B_{\rm nnn}$-1-U with ΛCDM and EdS growth factors.

significantly from the more accurate ΛCDM results. As such, it is clear that the use of ΛCDM growth factors is essential for high precision regularisation of the one-loop bispectrum.

For the growth factor corrections with the auto bispectrum, we again find that $\Delta D_1 \approx -0.003$ and $\Delta D_2 \approx 0.005$ on large scales. However, the corrections begin to deviate strongly from those of the propagator at $k \sim 0.07h$ Mpc^{-1}.

8.3 | Parameter Calibration

With our growth factors, our use of CVC, and our values of the m parameter chosen for both propagators and the auto bispectrum, we performed a number of different fittings for our various free parameters. By comparison to the results of Chapter 8.1.4, we emphasise that these results are only valid on the scales at which two and higher loop effects are negligible, but show that they do produce a good estimator for the non-linear correlators on those scales.

8.3.1 | Counterterms

The calculations of γ, γ_1, and γ_2 from our various fitting procedures are plotted in Fig. 8.11. In the left hand panel we present all of the calculations of the isolated γ_1 and γ_2 from the propagator terms. The values for the various fitting procedures for γ_2 from $B_{\rm n11}$ and the $B_{\rm n21}$-4 fitting for γ_1 all agree with one another for most values of $k_{\rm max}$, mimicking the shape of the value of $c_{\rm s}^2$ calculated from $P_{\rm n1}$, while the $B_{\rm n21}$-3 calculation of γ_1 differs from this

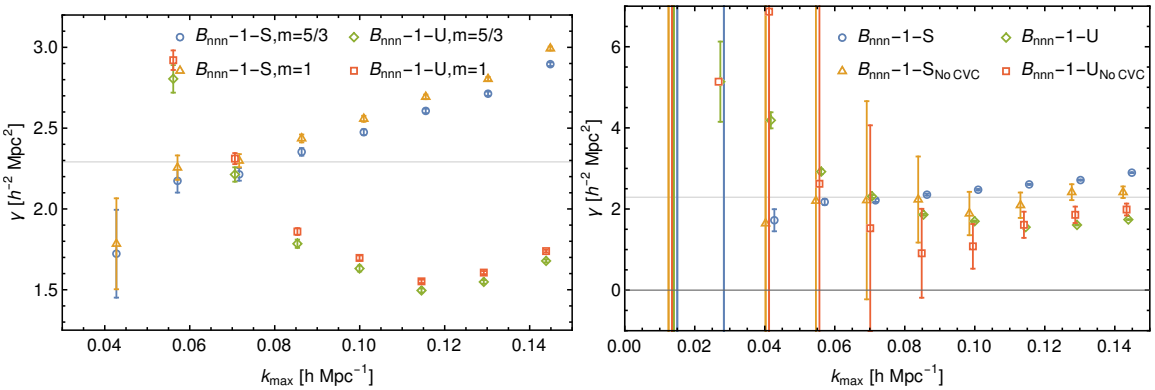

Figure 8.9: *Left panel:* Constraints on a joint γ from the auto bispectrum with both symmetry and UV inspired parametrisations for both suggested values of the parameter m. As with the propagator, the differences are at the percent level. We set $m = 1$ for the UV inspired studies of the auto bispectrum and $m = 5/3$ for the symmetry inspired studies. *Right panel:* Constraints on the joint γ from $B_{\rm nnn}$ with both symmetry and UV inspired parametrisations with and without cosmic variance cancellation. In the non-CVC case, we continued to use the residual with subtracted grid PT contributions and only changed the variance in the denominator, to avoid issues with IR divergences. The results without CVC clearly show larger error bars than those without.

curve but is of roughly the same value as $c_{\rm s}^2$ at $k_{\rm max} < 0.07h$ Mpc^{-1}. In the right hand panel we present the fittings for γ made with the auto bispectrum. We found that while the joint γ tended to give roughly the same result for all fittings, the independent γ_1 and γ_2 sometimes gave results less in keeping with the value we would have expected by comparison with the speed of sound and were omitted from the figure. The Fisher matrix for the routine $B_{\rm nnn}$-3 shows γ_1 and γ_2 have a cross-correlation of -0.98, making them almost completely degenerate; it is possible that at higher loop order the degeneracy would be broken. As will be discussed in the next subchapter, while the degeneracy between the two γ terms resulted in differing results for the individual counterparameters when they were allowed to vary independently, the overall counterterms still gave good fits to the residuals of the measured bispectra.

As expected, the $k_{\rm max}$ dependence of the results from the auto bispectrum more closely match the $k_{\rm max}$ dependence of $c_{\rm s}^2$ calculated from $P_{\rm nn}$, while those from the propagator are more similar to those of $P_{\rm n1}$. On the very large scales where the $c_{\rm s}^2$ measurements from the two power spectra agree with one another due to the small contribution from higher loop terms, we also find that our calculations from the auto and propagator bispectra begin to agree, though in both cases we begin to see results from a number of our fitting procedures that differ from those of other procedures. In theory, the counterterm amplitudes or low-energy-constants should not be scale dependent. However, any estimator for these amplitudes will

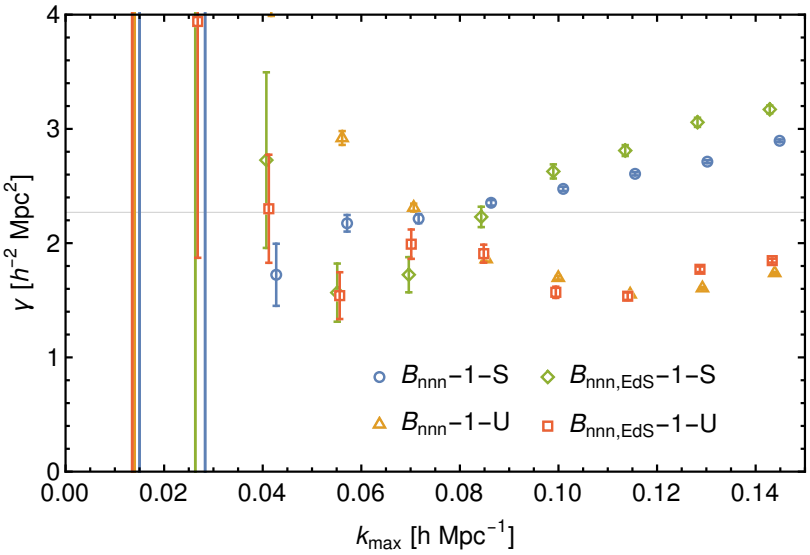

Figure 8.10: The joint γ as calculated from the auto bispectrum using methods $B_{\rm nnn}$-1-S and $B_{\rm nnn}$-1-U with ΛCDM and EdS growth factors.

explicitly include terms only up to a given perturbative order and will exclude contributions from higher order terms, which invariably make larger contributions on smaller physical scales. On large scales the constraints should asymptote to a constant and we restrict our final constraints to this asymptotic scale-independent regime. The behaviour is qualitatively the same that is observed in the power spectrum as mentioned in the caption of Figs. 8.5 and 7.4.

In Fig. 8.12 we plot the inferred values of the counterterm amplitudes ε_2 and ε_3 as measured with the symmetry inspired fittings for both the auto bispectrum and the propagator. The values constrained with the symmetry-inspired ansatz have the opposite sign to those used in the UV inspired fitting.

The complete set of reduced χ^2 calculations made with ΛCDM growth factors is plotted in Fig. 8.13. The reduced χ^2 of the UV-based ansatz is significantly greater than one in all cases for both the propagator and the auto bispectrum excepting $B_{\rm nnn}$-3-U and $B_{\rm nnn}$-4, which both feature UV inspired counterterms with two free parameters rather than one. The multiple parameter results, those being the symmetry based calculations as well as the two parameter UV inspired parametrisations, provided good fits at the momentum ranges of interest. We take this as evidence that single parameter models are not sufficiently flexible to regularise the one-loop bispectrum.

The performance of the fitted models can also be assessed by comparing the value of $B_{\rm SPT} + B_{\rm counterterms}$ to the measured residuals; this is shown for the equilateral configuration in Figs. 8.14 and 8.15. In the top left panels of Figs. 8.14 and 8.15, we plot $B^{\rm s}_{\rm nnn} - B^{\rm s}_{221} - B^{\rm s}_{311} - B^{\rm s}_{111}$ against the PT calculations of $B^{\rm s}_{211} + B^{\rm s}_{411} + B^{\rm s}_{321} + B^{\rm s}_{222} + B^{\rm s}_{\bar{1}21} + B^{\rm s}_{\bar{2}11}$ with

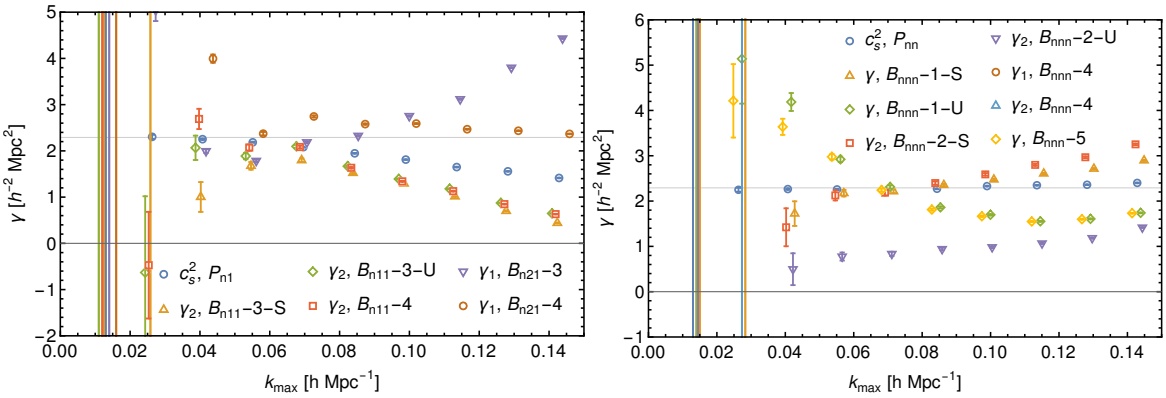

Figure 8.11: *Left panel:* Propagator measurements of γ_1 and γ_2 alongside the speed of sound measured from $P_{\rm n1}$. The results for γ_2 and the $B_{\rm n21}$-4 fitting for γ_1 closely mimic those of $c_{\rm s}^2$ from the power spectrum propagator while those of γ_1 from $B_{\rm n21}$-3 follow a different curve, holding similar values to the speed of sound at $k < 0.1h$ Mpc^{-1}. *Right panel:* Constraints on γ_1, γ_2, and the joint γ from the auto bispectrum alongside the speed of sound calibrated from $P_{\rm nn}$. The calculated values of γ_1 and γ_2 from the $B_{\rm nnn}$-3 procedures are omitted as the degeneracy of the two parameters made their results differ from the other fits.

counterkernels calculated according to a number of fitting procedures. The panel in Fig. 8.14 shows the total values of these calculations while those shown in the panel in Fig. 8.15 are normalised by the tree-level bispectra, to highlight the effects of the counterterms. Note that the parameters were constrained using the full bispectrum whereas only the equilateral configuration is shown in this figure. The top right panels show the equivalent calculations for the unsymmetrised $B_{\rm n11}$ and the bottom panels for $B_{\rm n21}$. From these figures, we can see that the results for the UV fitting procedures, 1-U, 2-U, 3-U, and 5 produce results that are at odds with the symmetry inspired procedures; method 4 is the only UV inspired fitting procedure to produce results which are in keeping with the symmetry inspired fits and closely match the residual at low k, due to the independent fitting of γ_1 on a measurement of $B_{\tilde{1}21,{\rm UV}}$ with modes corresponding exactly to those of the residual. Together with the results discussed above with reference to Fig. 8.12, this could be taken to mean that the approximation $B_{411,{\rm UV}} \approx B_{\tilde{2}11}$ is not sufficient and that the counterkernel $\tilde{F}_2$ must be given the full parameter freedom indicated by the symmetries of the EFTofLSS in order to accurately regularise the one-loop bispectrum. Noticeably, in the top left and bottom panels of Figs. 8.14 and 8.15, which incorporate the regularisation of $\tilde{F}_1$, the limit at which regularisation becomes impossible at one-loop order is at $k \sim 0.1h$ Mpc^{-1}, while in the top right panels we can see that for an isolated $\tilde{F}_2$ the limit is much lower, at $k \sim 0.05h$ Mpc^{-1}, indicating that this estimator is much more sensitive to two loop effects.

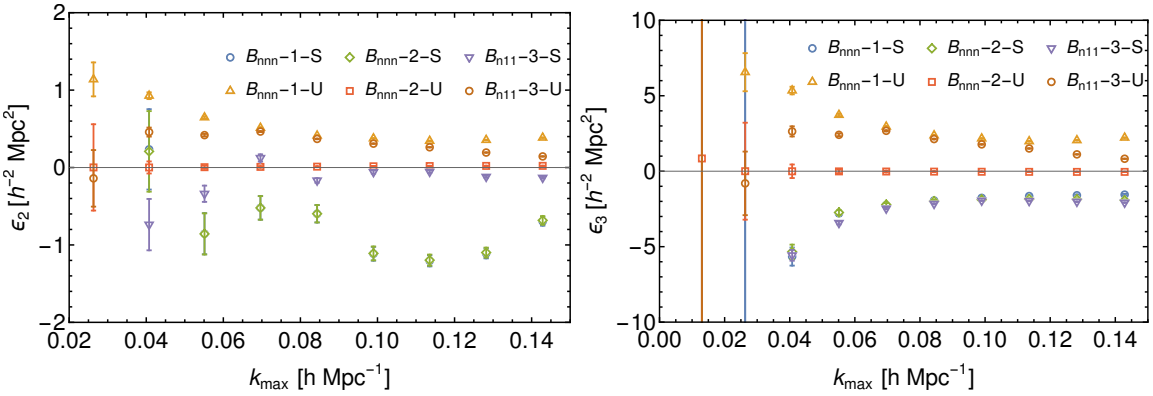

Figure 8.12: *Left panel:* The counterparameter ϵ_2 as measured from both the propagator and the auto bispectrum with the symmetry inspired parametrisation. In the case of UV inspired fits, it is simply a linear function of γ_2. *Right panel:* The counterparameter ϵ_3 as measured from both the propagator and auto bispectrum with symmetry inspired fittings. In the case of UV inspired fits, it is a linear function of γ_2. As in Fig. 8.11, the results from the B_{nnn}-3 fitting procedures are omitted as the degeneracy of the γ terms led to results that differed strongly from those of the other fits.

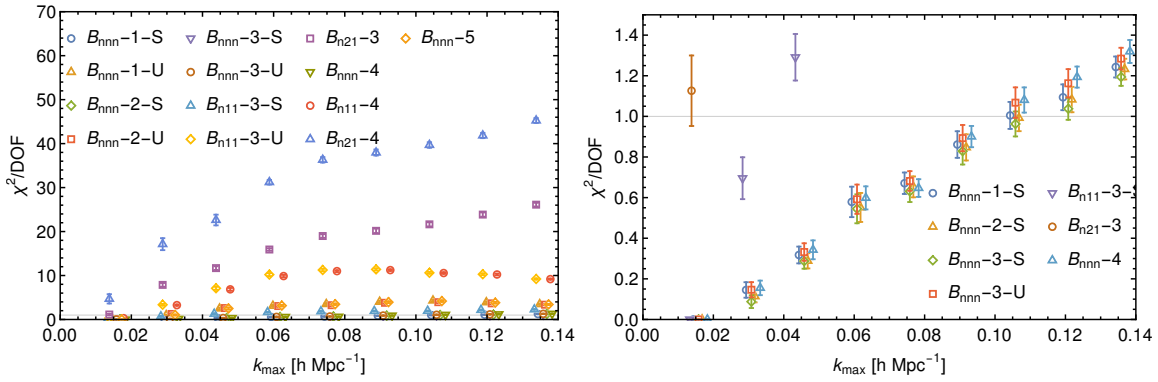

Figure 8.13: *Left panel:* The reduced χ^2 for all fitting procedures of the counterterms with ΛCDM growth factors for δ_2 and δ_3. Noticeably, the one-parameter fittings of isolated γ_1 and γ_2 all produce reduced χ^2 values an order of magnitude larger than those of the multiple parameter fittings. *Right panel:* The same with a focus on the values close to 1. The procedures which make use of more than one counterparameter provide better fits than those that rely upon only one, particularly at $k \sim 0.07h$ Mpc^{-1}.

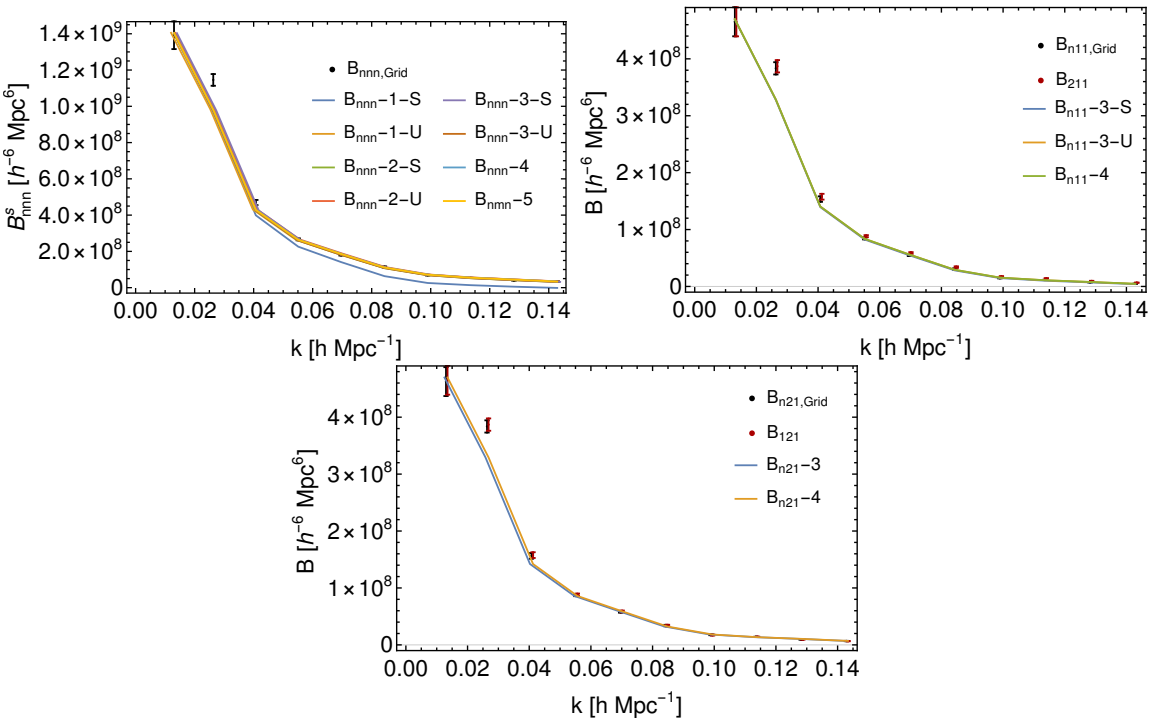

Figure 8.14: *Top left panel:* The measured equilateral $B^{\rm s}_{\rm nnn}$ minus the noise terms against the auto bispectrum up to one-loop calculated from perturbation theory using the values of the counterkernels taken from a variety of fitting procedures. *Centre left panel:* The measured equilateral $B_{\rm n11}$ minus the noise terms against the one-loop bispectrum propagator calculated from perturbation theory using the values of the counterkernels calculated with a number of fitting procedures, together with B_{211}. *Bottom left panel:* The measured equilateral $B_{\rm n21}$ minus the noise terms against its one-loop perturbation theory estimator using the counterkernels calculated using methods $B_{\rm n21}$-3 and $B_{\rm n21}$-4, together with the SPT up to one loop without counterterms.

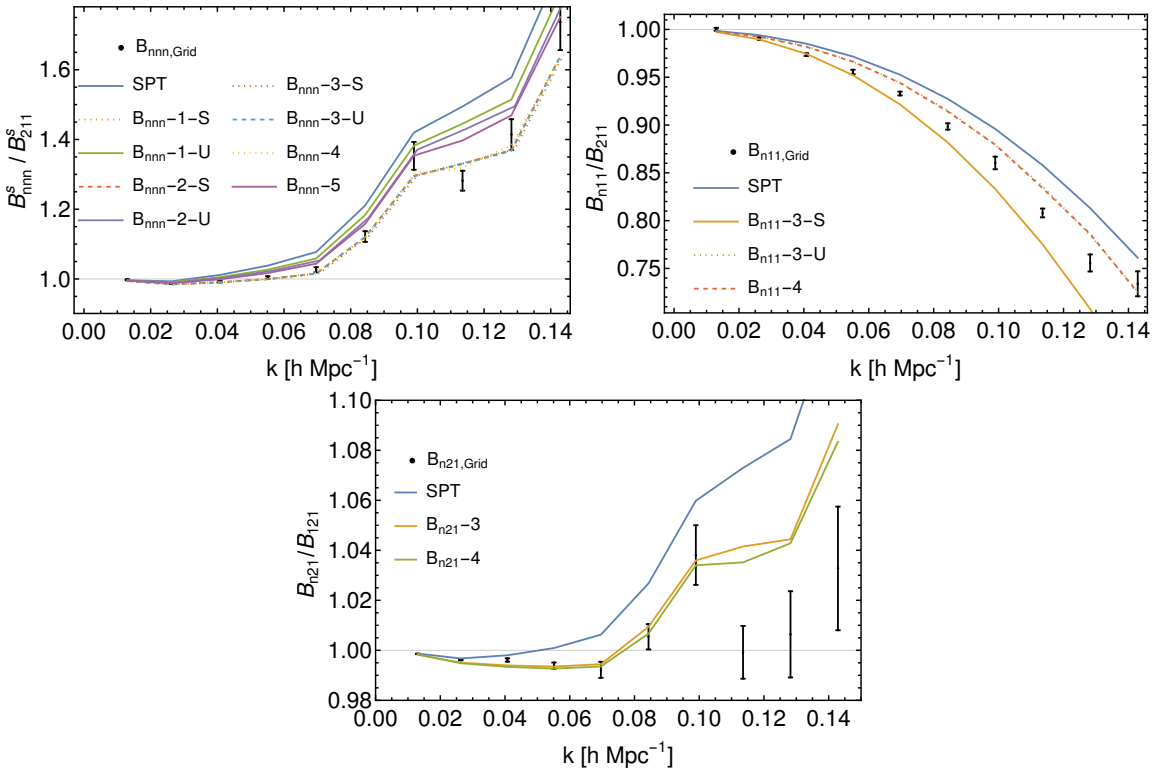

Figure 8.15: *Top right panel:* The ratio $B^{\mathrm{s}}_{\mathrm{nnn}}/B^{\mathrm{s}}_{211}$ for both the measured equilateral residual and the calculated equilateral bispectra with a number of fitting procedures as well as the SPT up to one-loop without counterterms. Many of the fits are good at lower momenta, where the tree-level and one-loop terms dominate, and begin to diverge from the residual at around $k \sim 0.1h$ Mpc^{-1}, roughly the limit where two-loop terms would be expected to come to dominate the bispectrum. *Centre right panel:* The ratio B_{n11}/B_{211} for both the measured and calculated equilateral bispectra with $k_{\mathrm{max}} = 0.084h$ Mpc^{-1} together with the SPT up to one-loop without counterterms. The fit works up until roughly this k, at which point there becomes a noticeable deviation between the residual and the counterterms due to the increasing involvement of higher loop terms. *Bottom right panel:* The ratio B_{n21}/B_{211} for both the measured and calculated equilateral bispectra together with the SPT up to one loop without counterterms. The fit works until $k = 0.1h$ Mpc^{-1}, indicating that this is the limit at which the exclusion of two-loop terms makes accurate regularisation impossible.

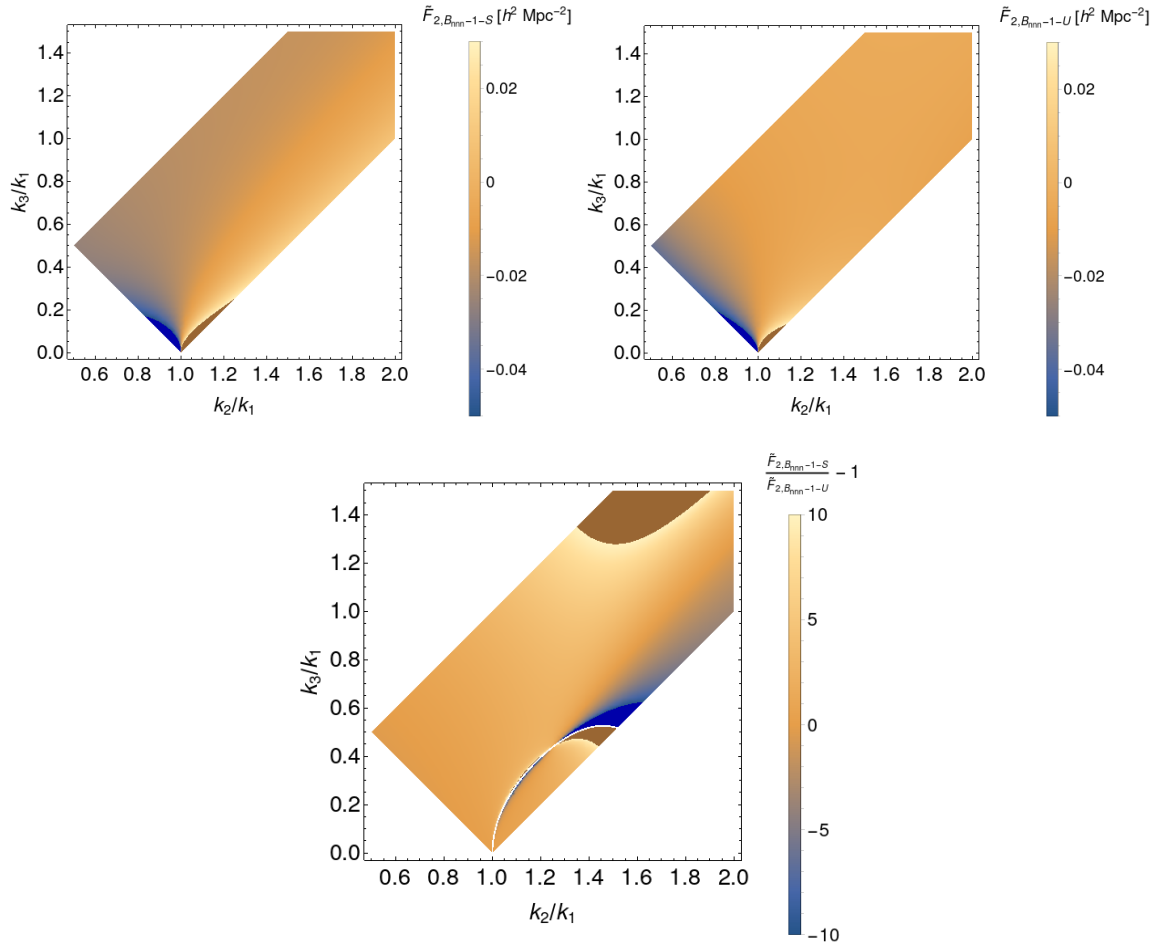

Figure 8.16: *Top left panel:* The value of $\tilde{F}_2$ as a function of the ratios k_2/k_1 and k_3/k_2 with the B_{nnn}-1-S parametrisation. There is a strong configuration dependence to the calculated counterterms, the sign crossing occurring in the isosceles case and becoming more prominent in the squeezed limit, that being when $k_3 \to 0$, when $k_1 > k_2$ and increasingly positive values in the squeezed limit as $k_1 < k_2$. The dark blue regions show clipping for negative values and the brown regions show clipping for positive values. *Top right panel:* The value of $\tilde{F}_2$ as a function of the ratios k_2/k_1 and k_3/k_2 with the B_{nnn}-1-U parametrisation. As before, there is a noticeable configuration dependence with the value of $\tilde{F}_2$ tending towards increasingly negative values as it descends into the squeezed limit with $k_1 > k_2$ and increasingly positive values as it descends into the same limit with $k_1 < k_2$. However, the configuration dependence seems to be less strong than that of the symmetry inspired fit, with a much shallower gradient visible throughout most of the plot. We can clearly see that the UV inspired fitting shows less configuration dependence than the symmetry inspired fit; this is the result of the fixing of the shape functions to be linear functions of γ, where it is important to remember that the shape functions encode the configuration dependence of the counterterm. The dark blue regions show clipping for negative values and the brown regions show clipping for positive values. *Bottom panel:* The fractional deviation of the above two calculations, $\tilde{F}_{2,\mathrm{B_{nnn}-1-S}}/\tilde{F}_{2,\mathrm{B_{nnn}-1-U}} - 1$. The dark blue regions show clipping for negative values and the brown regions show clipping for positive values.

Interestingly, the results from the B_{nnn}-3 fitting procedure give a good fit to the simulations according to Fig. 8.13 and regularise the one-loop auto bispectrum approximately as well as those from the B_{nnn}-1-S fitting, in spite of the differing results these procedures gave for their individual counterparameters. This indicates that the degeneracy did not affect the ability of the minimisation to give a good fit for the counterterm, merely that allowing the degenerate parameters to vary independently allowed a variety of combinations of counterparameter values to be sampled which were all still able to accurately regularise the auto bispectrum up to $k_{\text{max}} \sim 0.1h\,\text{Mpc}^{-1}$. It is notable that even the B_{nnn}-3-U produced accurate results, in contrast to those of B_{nnn}-1-U, indicating that allowing the γ parameters to vary separately compensated for the inaccuracy introduced by fixing the ε_i terms.

While Fig. 8.14 gave us a clear test of the accuracy of the various fittings, we also wish to compare the configuration dependence of the UV and symmetry inspired parametrisations. In Fig. 8.16 we plot the calculated values of $\tilde{F}_2$ as a function of the ratios of the momentum magnitudes k_3/k_1 and k_2/k_1 for both fitting procedures B_{nnn}-1-S and B_{nnn}-1-U, together with the relative deviation between the shape dependence of the two operators. As can be seen, the UV approximation shows less configuration dependence, only noticeably decreasing in the squeezed limit as k_3 becomes much smaller than the other two momentum magnitudes. As well as producing a less accurate fit to the simulation residuals, the ultraviolet approximation appears to produce less shape dependence in its results, which is understandable as the approximation consists of setting the shape function parameters to be linear functions of γ_2, preventing the counterterm from independently fitting to any given configuration.

8.3.2 | Growth Factor Corrections

Fig. 8.17 shows the calculated value of the growth factor corrections from both the measured bispectra and the power spectra. Both the auto power spectrum and propagator measurements asymptote to $\Delta D_1 \approx -2.5 \times 10^{-4}$ on large scales. The range over which the ΔD_1 measurements agree conforms with the range over which the c_{s}^2 measurements agree. The clear detection of this linear growth correction indicates that the linear growth in the simulations has a fractional systematic error of the same magnitude. While an offset this small might not be of any relevance for survey analysis, our ability to detect this offset proves the power of our realisation based perturbation theory approach. It can in fact be used to diagnose the accuracy of the N-body code on large scales.

The constraints on ΔD_1 from the bispectrum are much less coherent than those from the power spectrum which were illustrated in Fig. 7.5, but this follows from the fact that they are dominated by an odd correlator, the noise term B_{111}. The constraints on ΔD_2 are much

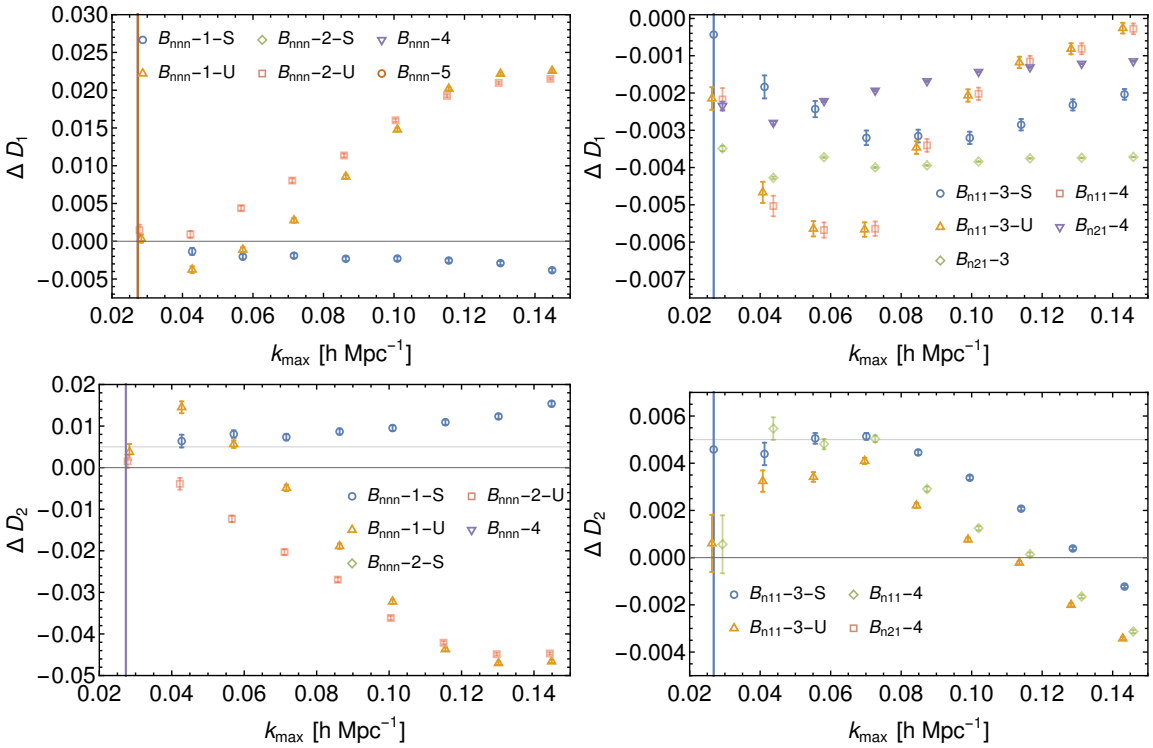

Figure 8.17: *Top left panel:* The growth factor correction ΔD_1 from the auto bispectrum. *Top right panel:* The growth factor correction ΔD_1 from the propagators. *Bottom left panel:* The growth factor correction ΔD_2 from the auto bispectrum. The results for fitting procedure $B_{\rm nnn}$-5 are omitted as they were significantly larger than the others. *Bottom right panel:* The growth factor correction ΔD_2 from the propagators.

tighter and point towards $\Delta D_2 \approx 0.005$ on large scales, with the constraints from the B_{n11} propagator being the most decisive.

8.4 | Summary

In this chapter we have investigated and calibrated the one-loop bispectrum of the EFTofLSS by comparing it to the non-linear bispectra measured from fourteen GADGET-II simulations. We have shown that, while the UV limit of the one-loop term B_{311} can be used as an estimator for its own counterterm, equivalently to how we showed the same for the one-loop power spectrum contribution P_{31} in Chapter 7, the remaining one-loop terms' UV limits cannot be assumed to constitute valid estimators for their own counterterms and can only be used as such estimators when the parametrisation of the model provides alternative free parameters which can account for beyond cutoff physics that does not scale as those UV terms. We have shown that it is important to use the correct ΛCDM growth factors when studying

bispectral perturbation theory and that the errors introduced by using the more common and simple EdS approximation cannot be accounted for by changing the counterterm, as could be done with the power spectrum. We also showed that the growth factor corrections, initially discussed in Chapter 6.1.3, take statistically significant and non-trivial values when fitted against our data, making it important to incorporate them into the model in order to account for the associated errors. With all of these sources of error accounted for, we have calibrated the counterterms for the one-loop bispectrum using a number of parametrisations and have compared their results, showing that treating γ_1 and γ_2 as separate parameters leads to degeneracy between the two but still permits accurate overall calibrations of the model, and that UV approximations of the counterterms taken from the grid are insufficient to accurately model the non-linear bispectrum. These results constitute a significant improvement over previous attempts at calibrating the perturbative bispectrum up to one-loop, which did not take into account any of the corrections we have made in this chapter, and we use our results in Chapter 9 to calibrate the one-loop trispectrum counterterms which feature the same counterkernels.

9

The Trispectrum

In this chapter we discuss and regularise the one-loop trispectrum in the EFTofLSS. In the opening part of Chapter 9.1, we review existing results regarding the perturbative description of the one-loop trispectrum and its counterterms. The subsequent subchapters consist of original research that was first presented in [28]. In Chapter 9.1.1, we discuss methods for reducing the measured error bars of our simulation results in order to obtain more precise calibrations of our counterterm parameters. In Chapter 9.1.3 we present the theoretical errors for the trispectrum and discuss how they relate to the magnitude of the measured loop corrections. In Chapter 9.2.1 we present counterterm calibrations for the parameters defining the counterkernels $\tilde{F}_1$ and $\tilde{F}_2$, and in Chapter 9.2.2 we present calibrations of the parameters defining the counterkernel $\tilde{F}_3$.

9.1 | Perturbation Theory

The trispectrum contains the non-Gaussian information in the covariance matrix of the power spectrum. As the covariance matrix of the power spectrum is a key component of cosmological parameter inference and the power spectrum is already well understood up to two-loop level, it is important to develop our understanding of the trispectrum in preparation for upcoming surveys.

Up to one-loop order the trispectrum is given by

$$\begin{aligned} T_{\text{tree+1-loop}} = {} & T_{3111} + T_{2211} + T_{5111} + T_{4211a} + T_{4211b} + T_{3221a} + T_{3221b} + T_{3221c} \\ & + T_{3311a} + T_{3311b} + T_{2222} \,, \end{aligned} \tag{9.1}$$

where T_{3111} and T_{2211} are the tree-level contributions. The contribution are given by

$$T_{3111}(k_1^i,k_2^i,k_3^i,k_4^i) = 3!F_3^{(s)}(k_2^i,k_3^i,k_4^i)P_{11}(k_2)P_{11}(k_3)P_{11}(k_4)\ , \tag{9.2}$$

$$\begin{aligned}T_{2211}(k_1^i,k_2^i,k_3^i,k_4^i) &= (2!)^2F_2^{(s)}(-k_3^i-k_4^i,k_4^i)F_2^{(s)}(k_3^i+k_4^i,k_2^i)\\ &\quad\times P_{11}(|k_3^i+k_4^i|)P_{11}(k_2)P_{11}(k_3)\ ,\end{aligned} \tag{9.3}$$

$$T_{5111}(k_1^i,k_2^i,k_3^i,k_4^i) = \frac{5!}{2!}\int_{q^i}F_5^{(s)}(q^i,-q^i,k_2^i,k_3^i,k_4^i)P_{11}(q)P_{11}(k_2)P_{11}(k_3)P_{11}(k_4)\ , \tag{9.4}$$

$$\begin{aligned}T_{4211a}(k_1^i,k_2^i,k_3^i,k_4^i) &= 4!\int_{q^i}F_4^{(s)}(q^i,-q^i,k_2^i+k_3^i,k_4^i)F_2^{(s)}(-k_2^i-k_3^i,k_3^i)\\ &\quad\times P_{11}(q)P_{11}(|k_2^i+k_3^i|)P_{11}(k_3)P_{11}(k_4)\ ,\end{aligned} \tag{9.5}$$

$$\begin{aligned}T_{4211b}(k_1^i,k_2^i,k_3^i,k_4^i) &= 4!\int_{q^i}F_4^{(s)}(k_1^i+q^i,-q^i,k_3^i,k_4^i)F_2^{(s)}(-q^i-k_1^i,q^i)P_{11}(|q^i+k_1^i|)\\ &\quad\times P_{11}(q)P_{11}(k_3)P_{11}(k_4)\ ,\end{aligned} \tag{9.6}$$

$$\begin{aligned}T_{3221a}(k_1^i,k_2^i,k_3^i,k_4^i) &= 3!2!\int_{q^i}F_3^{(s)}(q^i,-q^i,-k_1^i)F_2^{(s)}(k_1^i,k_3^i+k_4^i)F_2^{(s)}(-k_3^i-k_4^i,k_4^i)\\ &\quad\times P_{11}(q)P_{11}(k_1)P_{11}(|k_3^i+k_4^i|)P_{11}(k_4)\ ,\end{aligned} \tag{9.7}$$

$$\begin{aligned}T_{3221b}(k_1^i,k_2^i,k_3^i,k_4^i) &= 3!2!\int_{q^i}F_3^{(s)}(q^i+k_1^i,-q^i,k_3^i+k_4^i)F_2^{(s)}(-k_1^i-q^i,q^i)\\ &\quad\times F_2^{(s)}(-k_3^i-k_4^i,k_4^i)P_{11}(q)P_{11}(|k_1^i+q^i|)P_{11}(|k_3^i+k_4^i|)P_{11}(k_4)\ ,\end{aligned} \tag{9.8}$$

$$\begin{aligned}T_{3221c}(k_1^i,k_2^i,k_3^i,k_4^i) &= 3!(2!)^2\int_{q^i}F_3^{(s)}(q^i,-k_1^i-k_4^i-q^i,k_4^i)F_2^{(s)}(-q^i,q^i-k_2^i)\\ &\quad\times F_2^{(s)}(k_2^i-q^i,k_1^i+k_4^i+q^i)P_{11}(q)P_{11}(|k_1^i+k_4^i+q^i|)P_{11}(|q^i-k_2^i|)P_{11}(k_4)\ ,\end{aligned} \tag{9.9}$$

$$\begin{aligned}T_{3311a}(k_1^i,k_2^i,k_3^i,k_4^i) &= \frac{(3!)^2}{2!}\int_{q^i}F_3^{(s)}(q^i,-q^i,-k_1^i)F_3^{(s)}(k_1^i,k_3^i,k_4^i)P_{11}(q)\\ &\quad\times P_{11}(k_2)P_{11}(k_3)P_{11}(k_4)\ ,\end{aligned} \tag{9.10}$$

$$\begin{aligned}T_{3311b}(k_1^i,k_2^i,k_3^i,k_4^i) &= \frac{(3!)^2}{2!}\int_{q^i}F_3^{(s)}(q^i,-q^i-k_1^i-k_4^i,k_4^i)F_3^{(s)}(-q^i,q^i+k_1^i+k_4^i,k_3^i)\\ &\quad\times P_{11}(q)P_{11}(|q^i+k_1^i+k_4^i|)P_{11}(k_3)P_{11}(k_4)\ ,\end{aligned} \tag{9.11}$$

$$\begin{aligned}T_{2222}(k_1^i,k_2^i,k_3^i,k_4^i) &= (2!)^4\int_{q^i}F_2^{(s)}(q^i,-k_1^i-q^i)F_2^{(s)}(-q^i,q^i-k_2^i)\\ &\quad\times F_2^{(s)}(k_2^i-q^i,q^i-k_2^i-k_3^i)F_2^{(s)}(k_2^i+k_3^i-q^i,q^i+k_1^i)\\ &\quad\times P_{11}(q)P_{11}(|q^i-k_2^i|)P_{11}(|q^i-k_2^i-k_3^i|)P_{11}(|q^i+k_1^i|)\ ,\end{aligned} \tag{9.12}$$

each of which is shown diagrammatically in Fig. 9.1.

As with other correlators, each one-loop term requires regularisation. However, the counterterms for T_{2222}, T_{4211b}, T_{3221b}, T_{3221c}, and T_{3311b} are subleading noise terms and we

focus on the remaining four, which are given by

$$T_{\tilde{3}111}(k_1^i,k_2^i,k_3^i,k_4^i) = 3!\tilde{F}_3^{(s)}(k_2^i,k_3^i,k_4^i)P_{11}(k_2)P_{11}(k_3)P_{11}(k_4)\ , \tag{9.13}$$

$$\begin{aligned} T_{\tilde{2}211}(k_1^i,k_2^i,k_3^i,k_4^i) &= (2!)^2\tilde{F}_2^{(s)}(k_2^i+k_3^i,k_4^i)F_2^{(s)}(-k_2^i-k_3^i,k_3^i) \\ &\quad\times P_{11}(|k_2^i+k_3^i|)P_{11}(k_3)P_{11}(k_4)\ , \end{aligned} \tag{9.14}$$

$$T_{\tilde{1}311}(k_1^i,k_2^i,k_3^i,k_4^i) = 3!\tilde{F}_1^{(s)}(-k_1^i)F_3^{(s)}(k_2^i,k_3^i,k_4^i)P_{11}(k_2)P_{11}(k_3)P_{11}(k_4)\ , \tag{9.15}$$

$$\begin{aligned} T_{\tilde{1}221}(k_1^i,k_2^i,k_3^i,k_4^i) &= (2!)^2\tilde{F}_1^{(s)}(-k_1^i)F_2^{(s)}(k_1^i,k_3^i+k_4^i)F_2^{(s)}(-k_3^i-k_4^i,k_4^i) \\ &\quad\times P_{11}(k_1)P_{11}(|k_3^i+k_4^i|)P_{11}(k_4)\ , \end{aligned} \tag{9.16}$$

Feynman diagrams for each of which are shown in Fig. 9.2. Notice that each counterterm depends upon one counterkernel and three of them depend upon $\tilde{F}_1$ and $\tilde{F}_2$, the same counterkernels found in the counterterms to the one-loop bispectrum which we studied in Chapter 8. This gives us the opportunity to model $T_{\tilde{2}211}$, $T_{\tilde{1}311}$, and $T_{\tilde{1}221}$ using the amplitudes of the counterparameters calibrated from the bispectrum. This leaves only $T_{\tilde{3}111}$ left to be calibrated, which we shall discuss in Chapter 9.2.2. It is also notable that the UV limit of T_{5111} scales as $k_1^2P_{11}(k_2)P_{11}(k_3)P_{11}(k_4)$ implying that, when fitted to an amplitude, it could be used as an estimator for $T_{\tilde{3}111}$. We do not use explicitly use the UV limit of T_{5111} as an estimator for $T_{\tilde{3}111}$ in this paper but do define two one-parameter estimators that scale as $k_1^2P_{11}(k_2)P_{11}(k_3)P_{11}(k_4)$, which in theory should differ from $T_{5111,\mathrm{UV}}$ only by a constant that will be accounted for in the fitted parameter.

In order to perform an analysis of the one-loop trispectrum we must create both a perturbative calculation and a non-perturbative measurement of the trispectrum. Employing gridPT, we measure the individual contributions to the trispectrum such as T_{3111} and T_{5111} on the same grid used to analyse the simulation results; this allows much greater precision than could have been achieved by comparing the measured fully non-linear trispectrum to analytically calculated one-loop PT, both because it ensures that there is identical momentum shell averaging between the perturbative and non-linear density fields and because it allows us to reduce the noise by comparing perturbative and non-linear modes that arise from the same seeds. This leads to a number of interesting results which affect the counterterm calculations, as detailed in Secs. 9.1.1 and 9.2.2. We also evaluate regular numerical PT using a routine that relies upon the CUBA Vegas numerical integrator [70] and use this for comparative purposes as well as for some of our counterterm calculations, as will be discussed in Chapter 9.2.1.

All of the trispectra listed in Chapter 9.1 contribute to the auto trispectrum $T_{\rm nnnn}$. However, we can also isolate individual counterterms by studying the partially non-linear trispectra:

$$T_{\rm n111} = T_{3111} + T_{5111} + T_{\tilde{3}111} \,, \tag{9.17}$$

$$T_{\rm n211} = T_{2211} + T_{4211} + T_{\tilde{2}211} \,, \tag{9.18}$$

$$T_{\rm n221} = T_{1221} + T_{3221} + T_{\tilde{1}221} \,, \tag{9.19}$$

$$T_{\rm n311} = T_{1311} + T_{3311} + T_{\tilde{1}311} \,, \tag{9.20}$$

where the subscript n represents a non-linear density field. This allows us to constrain each counterterm separately, potentially increasing the precision of our calculations compared to calibrating all parameters of the four counterterms simultaneously from the non-linear trispectrum $T_{\rm nnnn}$.

By convention, $T_{\rm n111}$ is referred to as the trispectrum propagator. In this paper, we expand upon this convention and refer to all correlators which feature only one non-linear field as propagators. It is these four propagator terms that we shall study in the analysis described below.

Four momentum-space configurations were studied for this initial analysis of the trispectrum*:

PPM $\langle \delta(k_i)\delta(k_{i+1})\delta(k_{i+1})\delta(k_{i-1})\rangle$

PMM $\langle \delta(k_i)\delta(k_{i+1})\delta(k_{i-1})\delta(k_{i-1})\rangle$

MMM $\langle \delta(k_i)\delta(k_{i-1})\delta(k_{i-1})\delta(k_{i-1})\rangle$

PPP $\langle \delta(k_i)\delta(k_{i+1})\delta(k_{i+1})\delta(k_{i+1})\rangle$

where k_i represents the ith momentum bin, such that in all configurations one of the density fields was used as a reference while the others were positioned in the k-bins immediately above or below the reference. Specifically, it is the non-linear density field in the propagator terms that is chosen to be in the reference bin. We did not use configurations in which all four of the fields had the same momenta as allowing the diagonal legs to vary in this configuration leads to the intrusive inclusion of disconnected trispectra, i.e. pairs of anti-parallel power spectra in the measurement of the trispectra.

In Fig. 9.3 we plot the measured T_{5111} from both the Direct Summation and Fast Fourier Transform routines, which we discussed in detail in Chapter 6. Due to the computational

*This terminology originated from the notion that, with respect to the reference momentum bin which the non-linear density field or its placeholder are found in and which we label k_i, the three remaining density fields are in various combinations of the 'plus one' or 'minus one' momentum bins, those being the momentum bins immediately higher or lower than the reference bin.

intensity of the direct summation method, we were only able to sample a small fraction of the overall space, resulting in fewer data points with larger errors. This clearly demonstrates the benefits of using the Fourier transform method, which we use throughout the remainder of the paper to the complete exclusion of the direct summation method.

9.1.1 | Cosmic Variance Cancellation

In the infinite-volume limit, terms which describe disconnected pairs of power spectra, such as T_{1111}, should not contribute to the measured off-diagonal connected trispectrum. Likewise, terms which contain an odd number of linear density fields such as T_{2111} and T_{4111}, should vanish in accordance with Wick's Theorem. However, although their mean values will be zero, in a finite sample size they will have a non-zero variance. Using gridPT, we were able to generate the correlators for these terms and found that they made a significant contribution to the measured non-linear trispectra. With them explicitly measured, we were able to subtract them from the residuals, giving a significant reduction in cosmic variance. We hereafter refer to terms with a vanishing mean and non-zero variance as mean zero terms.

When removing mean zero terms, we only remove those that have an highest order density field at most as high in order as the highest order density field in the corresponding one-loop contribution, such that we have

$$T_{\mathrm{n}111,\mathrm{grid}} \to T_{\mathrm{n}111,\mathrm{grid}} - T_{4111,\mathrm{grid}} - T_{2111,\mathrm{grid}} - T_{1111,\mathrm{grid}} \,, \tag{9.21}$$

$$T_{\mathrm{n}211,\mathrm{grid}} \to T_{\mathrm{n}211,\mathrm{grid}} - T_{3211,\mathrm{grid}} - T_{1211,\mathrm{grid}} \,, \tag{9.22}$$

$$T_{\mathrm{n}221,\mathrm{grid}} \to T_{\mathrm{n}221,\mathrm{grid}} - T_{2221,\mathrm{grid}} \,, \tag{9.23}$$

$$T_{\mathrm{n}311,\mathrm{grid}} \to T_{\mathrm{n}311,\mathrm{grid}} - T_{2311,\mathrm{grid}} \,. \tag{9.24}$$

In the left hand panel of Fig. 9.4 we plot the residual of $T_{\mathrm{n}111}$ with and without subtraction of the mean zero terms, which we refer to as a form of cosmic variance cancellation (CVC).

In studying the trispectrum we are interested in the kernels F_{n}. Any measurement of the trispectrum will include measurements of the included power spectra and these power spectra are the source of the majority of any measurement's variance. As such, we can significantly reduce the variance of our measurements by enacting cosmic variance cancellation on each of our trispectrum measurements by redefining

$$Q = \frac{\hat{T}}{\hat{P}^{n}_{11}} \tag{9.25}$$

for some product of linear power spectra P_{11}^n measured on the grid and corresponding to the power spectra found in the definitions of the trispectra. We perform this on a realisation by realisation basis, dividing by power spectra from the same realisation and grid as each measured trispectrum, before averaging our results. This isolates the kernels, effectively giving us a simulation measurement of the kernel itself, and in doing so removes all of the variance that came from the linear density fields.

In theory the most precise possible measurements of the counterterms would come from using $n = 3$ in Eq. (9.25) in order to fully remove the variance of the power spectrum from the measurements. However, many contributions to the trispectrum feature power spectra that are not simple functions of one of the external density fields' momenta but are instead an averaged sum of the momenta between different fields. This complicates the procedure and for the sake of convenience only power spectra of single density fields are removed from our measurements. As such, bearing in mind the momentum arguments of the power spectra in Eqs. (9.2) to (9.12), we have that

$$Q_{3111}(k_1,k_2,k_3,k_4,k_5,k_6) = \frac{T_{3111}(k_1,k_2,k_3,k_4,k_5,k_6)}{P_{11}(k_2)P_{11}(k_3)P_{11}(k_4)}\,, \tag{9.26}$$

$$Q_{5111}(k_1,k_2,k_3,k_4,k_5,k_6) = \frac{T_{5111}(k_1,k_2,k_3,k_4,k_5,k_6)}{P_{11}(k_2)P_{11}(k_3)P_{11}(k_4)}\,, \tag{9.27}$$

$$Q_{2211}(k_1,k_2,k_3,k_4,k_5,k_6) = \frac{T_{2211}(k_1,k_2,k_3,k_4,k_5,k_6)}{P_{11}(k_3)P_{11}(k_4)}\,, \tag{9.28}$$

$$Q_{4211}(k_1,k_2,k_3,k_4,k_5,k_6) = \frac{T_{4211}(k_1,k_2,k_3,k_4,k_5,k_6)}{P_{11}(k_3)P_{11}(k_4)}\,, \tag{9.29}$$

$$Q_{3221}(k_1,k_2,k_3,k_4,k_5,k_6) = \frac{T_{3221}(k_1,k_2,k_3,k_4,k_5,k_6)}{P_{11}(k_4)}\,, \tag{9.30}$$

$$Q_{3311}(k_1,k_2,k_3,k_4,k_5,k_6) = \frac{T_{3311}(k_1,k_2,k_3,k_4,k_5,k_6)}{P_{11}(k_3)P_{11}(k_4)}\,, \tag{9.31}$$

and T_{2222} is left as it is. Note that the power spectra in the denominators occupy the momentum bin of the linear density fields in the trispectra.

9.1.2 | Grid Measurements

Fig. 9.5 shows each of the contributions to the one-loop trispectrum in the four studied configurations with a cutoff of $\Lambda = 0.3h\,\mathrm{Mpc}^{-1}$ as measured both from the simulations and from perturbation theory. As can be seen, the grid perturbation theory agrees well with the analytic perturbation theory. This constitutes a highly non-trivial validation of both our CUBA and gridPT calculations of the trispectra.

9.1.3 | Theoretical Errors

Given that we are studying isolated counterterms in partially non-linear trispectra, we need only consider the tree level terms that are appropriate to the correlator under study. Specifically, for the four non-linear terms we are studying, we have that

$$\begin{aligned} \Delta T_{\mathrm{n}111,l} &= T_{3111}\left[\frac{k_{\mathrm{ext}}}{k_{\mathrm{n}}}\right]^{(3+n_{\mathrm{n}})l}, \quad \Delta T_{\mathrm{n}211,l} = T_{2211}\left[\frac{k_{\mathrm{ext}}}{k_{\mathrm{n}}}\right]^{(3+n_{\mathrm{n}})l}, \\ \Delta T_{\mathrm{n}221,l} &= T_{1221}\left[\frac{k_{\mathrm{ext}}}{k_{\mathrm{n}}}\right]^{(3+n_{\mathrm{n}})l}, \quad \Delta T_{\mathrm{n}311,l} = T_{1311}\left[\frac{k_{\mathrm{ext}}}{k_{\mathrm{n}}}\right]^{(3+n_{\mathrm{n}})l}, \end{aligned} \tag{9.32}$$

where the momentum in the denominator is $k_{\mathrm{ext}} = k_1$ because that is the momentum of the one-loop density field and we have chosen $n_{\mathrm{NL}} = -1.3$ to fit the magnitude of our one-loop theoretical errors to our measured one-loop contributions.

As shown in Fig. 9.6, the measured values of the one-loop ratios fall within the expected errors for most configurations; the notable exceptions being the MMM configuration for T_{3221} and the large scale values of the PPP configuration for the same trispectrum. While undesirable, this is in keeping with the general difficulty we have faced with these configurations. Also plotted are the expected magnitudes of the two and three loop contributions. To avoid attempting to use a one-loop analysis in a region heavily affected by higher loop terms, we will generally limit our analysis to $k_{\mathrm{max}} = 0.083h\ \mathrm{Mpc}^{-1}$.

9.2 | Parameter Calibration

In this subchapter we will calibrate the free parameters of our model. We make extensive use of the values of γ_1, γ_2, and $\varepsilon_{1,2,3}$ taken from the bispectra, as presented in Chapter 8; this not only allows us to produce estimators for partially non-linear trispectra without recourse to separate calibrations of the same parameters, but also provides a test of consistency between our results.

We apply a growth factor correction of $\Delta D_2 \approx 0.005$ inspired by our bispectrum measurements from Chapter 8 to account for time integration inaccuracies in the N-body results, but do not fit for growth factor correction parameters directly from trispectra; attempts at doing do produced unphysical results which we attribute to the fact that the trispectral calculations were less precise than those of the bispectra, such that incorporating new free parameters into the model which were not necessary at the levels of precision being obtained simply introduced new redundant degrees of freedom. As such, this subchapter concerns itself entirely with the calibration of the EFTofLSS counterterms.

9.2.1 | The $\tilde{F}_1$ and $\tilde{F}_2$ Kernels

InChapter 8 we defined a number of methods with which we constrained the parameters of $\tilde{F}_1$ and $\tilde{F}_2$ from the one-loop bispectrum. Here we will take from the calibrations presented in that chapter that $\gamma_2 = 2.332h^{-2}$ Mpc^2, a value obtained using what we referred to as method $B_{\rm nnn}$-1-S and which we refer to hereafter as $\gamma_{2,\rm B}$, leaving us with two parametrisations for the ε parameters of $\tilde{F}_2$ seen in Eq. 5.47; the UV inspired parametrisation in which we have $\varepsilon_1 = 0$, $\varepsilon_2 = -0.565$, and $\varepsilon_3 = -1.699$, and the symmetry inspired parametrisation in which we have $\varepsilon_1 = 0.618$, $\varepsilon_2 = 0.517$, and $\varepsilon_3 = 2.978$, together with the approximation $\gamma_1 = c_{\rm s}^2$, giving a value of $\gamma_1 = 2.27h^{-2}$ Mpc^2. We also take the UV approximations of the counterterms and of the components of $\tilde{F}_2$ calculated on the grid and fit them as counterterms, both with the values of γ_1 and γ_2 just mentioned and with independent fits to their respective residuals.

With these parameters, we use the following methods for estimating the trispectrum counterterms containing $\tilde{F}_1$ and $\tilde{F}_2$:

- We will use the chosen value of $\gamma_{2,\rm B}$ together with both corresponding parametrisations for the ε_i to calculate $T_{\tilde{2}211}$ perturbatively.
- We will use the chosen value of c_s^2 calibrated from the bispectrum to calculate $T_{\tilde{1}221}$ and $T_{\tilde{1}311}$ perturbatively.
- We will use the chosen value of c_s^2 as the amplitude of $\gamma_1 T_{\tilde{1}221,\rm grid}$ and $\gamma_1 T_{\tilde{1}311}$.
- We will use the chosen value of $\gamma_{2,\rm B}$ as the amplitude of $\gamma_2 T_{\tilde{2}211,\rm grid}$.
- We will use a values of $\gamma_{2,\rm B}$ and $\varepsilon_{1,2,3}$ as calibrated from the bispectrum as the amplitudes for the constituent functions of $\tilde{F}_2$ measured on the grid and sum these to estimate $T_{\tilde{2}211}$ with both symmetry and UV inspired parametrisations. We refer to the parameters from the symmetry inspired parametrisation with the subscript S and those with the UV inspired parametrisation with the subscript U.
- We will fit for the amplitude of $\gamma_1 T_{\tilde{1}221,\rm grid}$.
- We will fit for the amplitude of $\gamma_1 T_{\tilde{1}311,\rm grid}$.
- We will fit for the amplitude of $\gamma_2 T_{\tilde{2}211,\rm grid}$.

The counterterms calculated in this way for $T_{\tilde{2}211}$ are plotted alongside the residuals in Figs. 9.7 and 9.8 for the four considered configurations. We can see that the UV approximations produce far more accurate results in analytic perturbation theory than the symmetry inspired fits, with the UV inspired models successfully approximating the residual on all

scales for configurations PPM and PMM and on all but the largest scales for MMM. However, for PPP we found that we were unable to successfully regularise $T_{\mathrm{n}211}$ at any scale. These inaccuracies could be the result of simulation or analysis systematics which will be explored further in a future paper. We will also explore explicit trispectrum configurations without integrating over the diagonal legs in order to see if this averaging played a role in these errors. In addition, we find that the two-loop errors are much larger than might have been expected, encompassing many of the counterterm calculations, indicating that two-loop terms would need to be taken into account for an accurate and precise calibration of these terms.

The counterterms calculated in this way for $T_{\tilde{\mathrm{I}}221}$ are plotted alongside the residuals in Fig. 9.9 and 9.10 for the four considered configurations. We see that the regularisation using a number of methods works on very large scales but rapidly ceases to work beyond roughly $k \sim 0.04h$ Mpc^{-1}, perhaps indicating that two loop terms make a much larger contribution to the trispectrum than they do to the bispectrum, where they do not have a large effect until roughly $k \sim 0.08h$ Mpc^{-1}. Most noticeably, in the case of configuration MMM the fit only works for the UV parametrisations with $\gamma_1 = c_{\mathrm{s}}^2$ and even then only until $k \approx 0.04h$ Mpc^{-1}, beyond which these models do not even have the same sign or shape as the residual. The configuration dependence of our ability to regularise this trispectrum is noticeable; for configuration PPM we find that method 3 provides a very good regularisation up to about $k \sim 0.1h$ Mpc^{-1} and that the other two methods fail, while for configuration MMM we find that method 3 fails at all scales and that methods 1 and 2 provide good fits but only at very large scales. Furthermore, the theoretical error envelope that predicts the magnitude of the two loop terms encompasses most of our results, indicating that without taking two loop terms into account, our results are likely to be inaccurate.

The counterterms calculated in these ways for $T_{\tilde{\mathrm{I}}311}$ are plotted alongside the residuals in Figs. 9.11 and 9.12 for the four considered configurations. We see that the various methods produce similar results to one another and all provide an adequate approximation to the one-loop residual of $T_{\mathrm{n}311}$ at least until $k \sim 0.06h$ Mpc^{-1}. However, once again we see that the two loop theoretical error is very large and encompasses many of our calculations.

Overall, we see that this approach has a much higher rate of success in calculating the counterterms $T_{\tilde{2}211}$, $T_{\tilde{\mathrm{I}}221}$, and $T_{\tilde{\mathrm{I}}311}$ than the α-parametrisation, with some methods working better than others, but still failed to completely account for the corresponding one-loop residuals up to the desired momenta for all configurations. There are a number of possible explanations for this, including a larger than expected contribution from two-loop or higher order noise terms and problems with the simulation's time integration. Nonetheless, we have found that our methods are able to regularise all of the isolated trispectra considered at at least some momenta for most configurations sampled. However, the large theoretical errors

for the two-loop terms indicate that our one-loop counterterm calculations are likely to be rendered ineffective without two loop terms being accounted for; this is left for a future project.

9.2.2 | The $\tilde{F}_3$ Kernel

The counterkernel $\tilde{F}_3$ was not constrained in Chapter 8 and is the new interaction studied in this chapter. We propose two simple one-parameter models for the counterterm $T_{\tilde{3}111}$ by defining what we call the α and β parametrisations, as will be discussed in this section.

Our first and simplest one parameter ansatz is to define

$$\begin{aligned} T_{\mathrm{n}111}(k_1^i,k_2^i,k_3^i,k_4^i) =& T_{3111}(k_1^i,k_2^i,k_3^i,k_4^i) + T_{5111}(k_1^i,k_2^i,k_3^i,k_4^i,\Lambda) \\ &+ \alpha_{\mathrm{n}111}(\Lambda) k_1^2 P_{11}(k_2) P_{11}(k_3) P_{11}(k_4) \,. \end{aligned} \tag{9.33}$$

This simply acknowledges that the counterterm is expected to scale as $k^2 P_{11}^3$ and leaves a free parameter, $\alpha_{\mathrm{n}111}$, to fit that curve to the measured residual. By rearranging this equation and removing unphysical terms, we can estimate the α parameter as

$$\alpha_{\mathrm{n}111}(\Lambda) = \frac{T_{\mathrm{n}111}(k_1^i,k_2^i,k_3^i,k_4^i) - \sum_{i=1}^{5} T_{i111}(k_1^i,k_2^i,k_3^i,k_4^i)}{k_1^2 P_{11}(k_2) P_{11}(k_3) P_{11}(k_4)} \,. \tag{9.34}$$

In Fig. 9.13 we plot the calculated values of $\alpha_{\mathrm{n}111}$ for all four studied configurations, both as a function of k and as a χ^2 minimisation up to a k_{max}.

Secondly, we define the β parameters. By defining

$$T_{5111\mathrm{s},i-j} = T_{5111}(\Lambda_i) - T_{5111}(\Lambda_j) \,, \tag{9.35}$$

for T_{5111} with cutoffs of Λ_i and Λ_j, we have found a way of isolating and encapsulating the cutoff dependence of T_{5111}. We can then define the parameter β_{i-j}, which we call the amplitude of $T_{5111\mathrm{s},i-j}$, such that we can minimise

$$\begin{aligned} \chi^2_{\beta_{i-j}} = \sum_{k=k_{\mathrm{min}}}^{k_{\mathrm{max}}} & \frac{1}{\Delta T_{\mathrm{n}111}(k_1^i,k_2^i,k_3^i,k_4^i)^2} \left[T_{\mathrm{n}111}(k_1^i,k_2^i,k_3^i,k_4^i) - T_{\mathrm{SPT}}(k_1^i,k_2^i,k_3^i,k_4^i) \right. \\ & \left. - \beta_{i-j}(k_{\mathrm{max}}) T_{5111\mathrm{s},i-j}(k_1^i,k_2^i,k_3^i,k_4^i) \right]^2 \end{aligned} \tag{9.36}$$

for the amplitude and take $\beta_{i-j}(0.083h\ \mathrm{Mpc}^{-1}) T_{5111\mathrm{s},i-j}(k_1^i,k_2^i,k_3^i,k_4^i)$ as a counterterm estimator for the one-loop trispectrum propagator. Rather than simply fitting a curve with defined scaling to the residual as we did with the α parameter, the β parameters explicitly

account for the cutoff dependence of the one-loop terms; by capturing the difference between the measured terms with different cutoffs, they provide us with a curve that scales exactly as a counterterm should scale in order to capture any given term's cutoff dependence.

In Fig. 9.14 we plot the calculated $T_{3111} + T_{5111} + T_{\tilde{3}111}$ against the measured $T_{\mathrm{n}111} - T_{4111} - T_{2111} - T_{1111}$ using our calculated $T_{\tilde{3}111}$ with both the α and β parametrisations for the four configurations studied. We find that both parametrisations work reasonably well at the scales of interest, with the β parameters outperforming the α parameters in configurations PMM and PPP and the α parameters performing better for the configurations PPM and MMM. In both cases, at least one parametrisation was capable of providing a good fit to the measured residuals of $T_{\mathrm{n}111}$ up to $k \sim 0.07h$ Mpc^{-1}, where we would expect to see two loop effects strongly coming into effect.

9.3 | Summary

In this chapter we have described the perturbative one-loop trispectrum and calibrated its counterterms against the non-linear trispectra measured from fourteen GADGET-II simulations. We have shown, as we did for the bispectrum in Chapter 8, that the EdS approximation for the density field growth factors cannot be accounted for in the existing parametrisation and that it is therefore essential to use the correct ΛCDM growth factors if accurate calibrations of the counterterms are to be obtained. We have also demonstrated a number of ways of reducing cosmic variance, the systematic errors that consistently hinder attempts at measuring higher order correlators in cosmology. Taking these results into account, we have estimated the counterterms $T_{\tilde{2}211}$, $T_{\tilde{1}311}$, and $T_{\tilde{1}221}$ using the counterkernel parameter calibrations obtained from the bispectrum in Chapter 8 and have shown the more accurate bispectrum calibrations also lead to reasonably accurate trispectrum counterterm calibrations. For the remaining counterterm, $T_{\tilde{3}111}$, which contains a counterkernel that was not featured in the one-loop bispectrum, we developed a pair of estimators which we termed the α and β parametrisations of the counterterm and fitted them directly against partially non-linear trispectra, finding that both parametrisations provide good fits to the observered residuals on small momentum scales with the α parametrisation extending this fit to larger momenta than the β parametrisations.

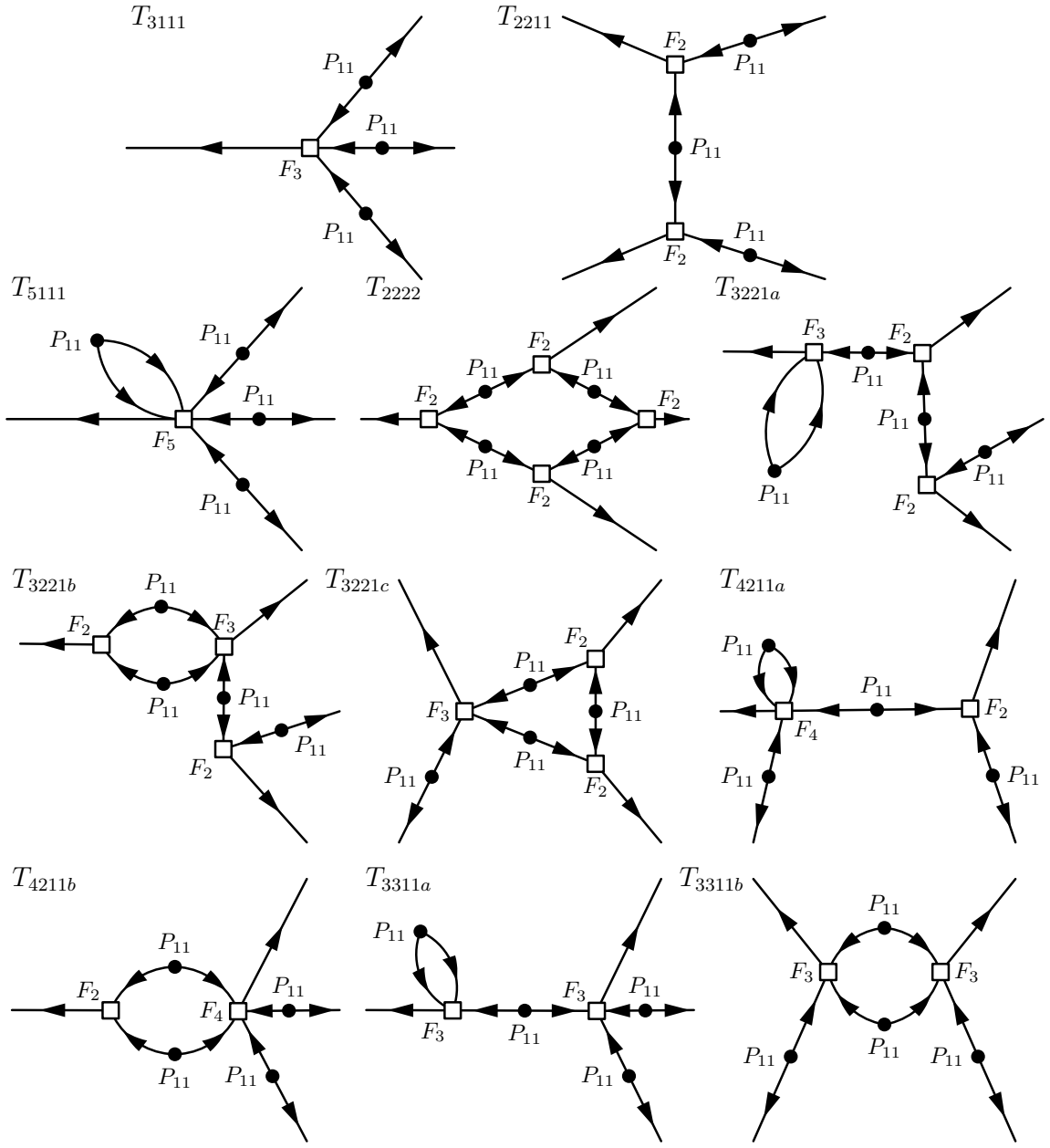

Figure 9.1: The tree-level (top row) and one-loop (other rows) contributions to the trispectrum. Note that T_{5111}, T_{3221a}, T_{4211a} and T_{3311a} contain free loops. This results in them constituting the leading UV-sensitive terms in the trispectrum. Most of them can be related to UV-sensitive interactions already encountered in the one-loop power spectrum and bispectrum, but T_{5111} constitutes a new UV-sensitive interaction.

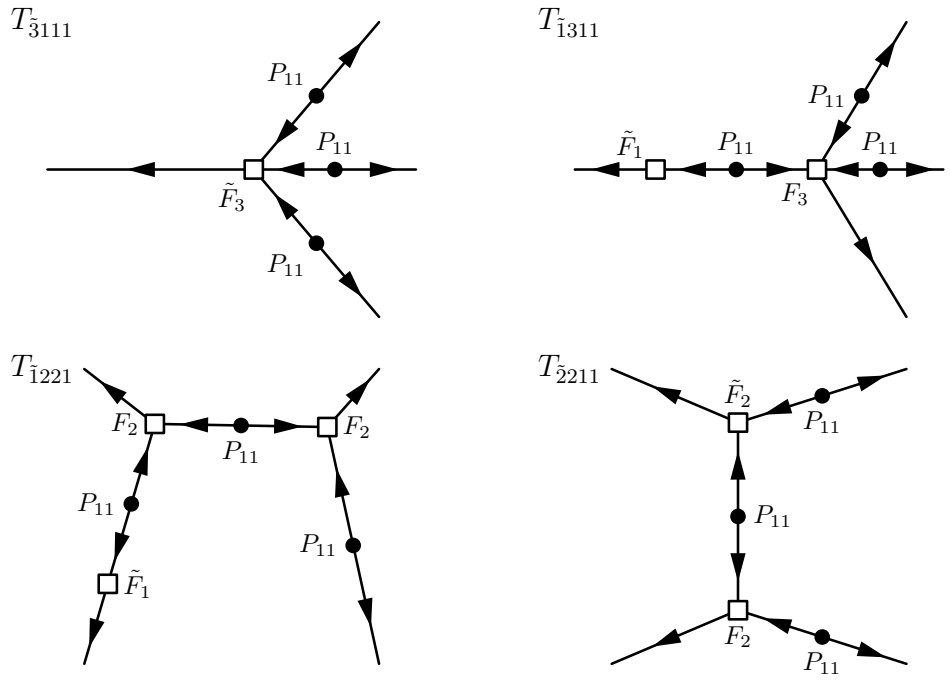

Figure 9.2: The leading counterterm diagrams for the one-loop trispectrum. Note that $T_{\tilde{2}211}$ contains the counterkernel $\tilde{F}_2$, which regularises the one-loop bispectrum and $T_{\tilde{1}221}$ and $T_{\tilde{1}311}$ contain the counterkernel $\tilde{F}_2$, which regularises the one-loop power spectrum (and some bispectrum terms). This leads to the opportunity of a consistency check by using counterterm amplitudes constrained in the power spectrum and bispectrum and assessing their ability to regularise the trispectrum.

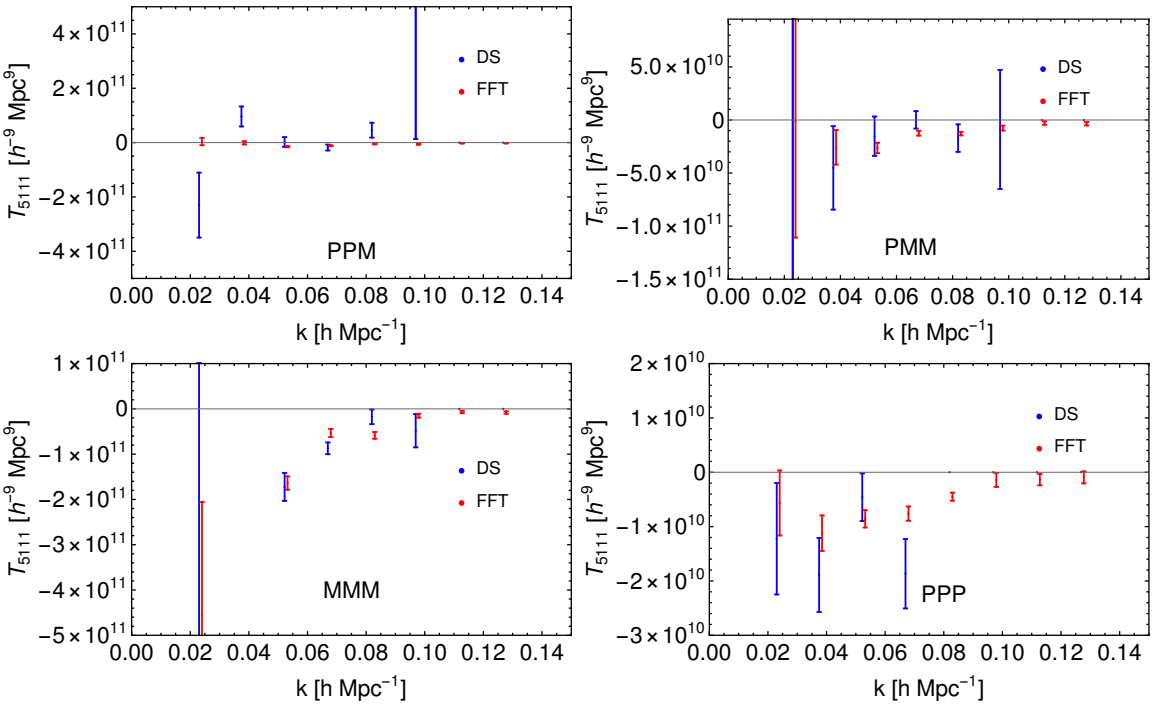

Figure 9.3: The measured T_{5111} in the four sampled configurations with both the direct summation (DS) routine and the Fourier transform routine (FFT). Notice that the DS routine only sampled a small fraction of the overall momentum space, resulting in it only measuring a few points for each configuration and each of those points being less precise than those measured by the FFT routine, which studied the entire grid.

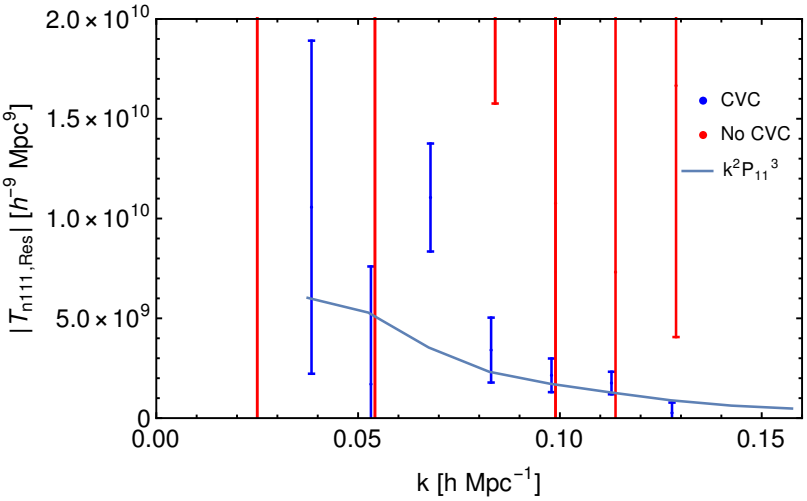

Figure 9.4: The measured residual of the trispectrum propagator $T_{\mathrm{n}111}$ in configuration PPM with and without subtracting off the mean zero terms, together with a curve which scales as the counterterm would be expected to, that being $k_1^2 P_{11}(k_2) P_{11}(k_3) P_{11}(k_4)$.

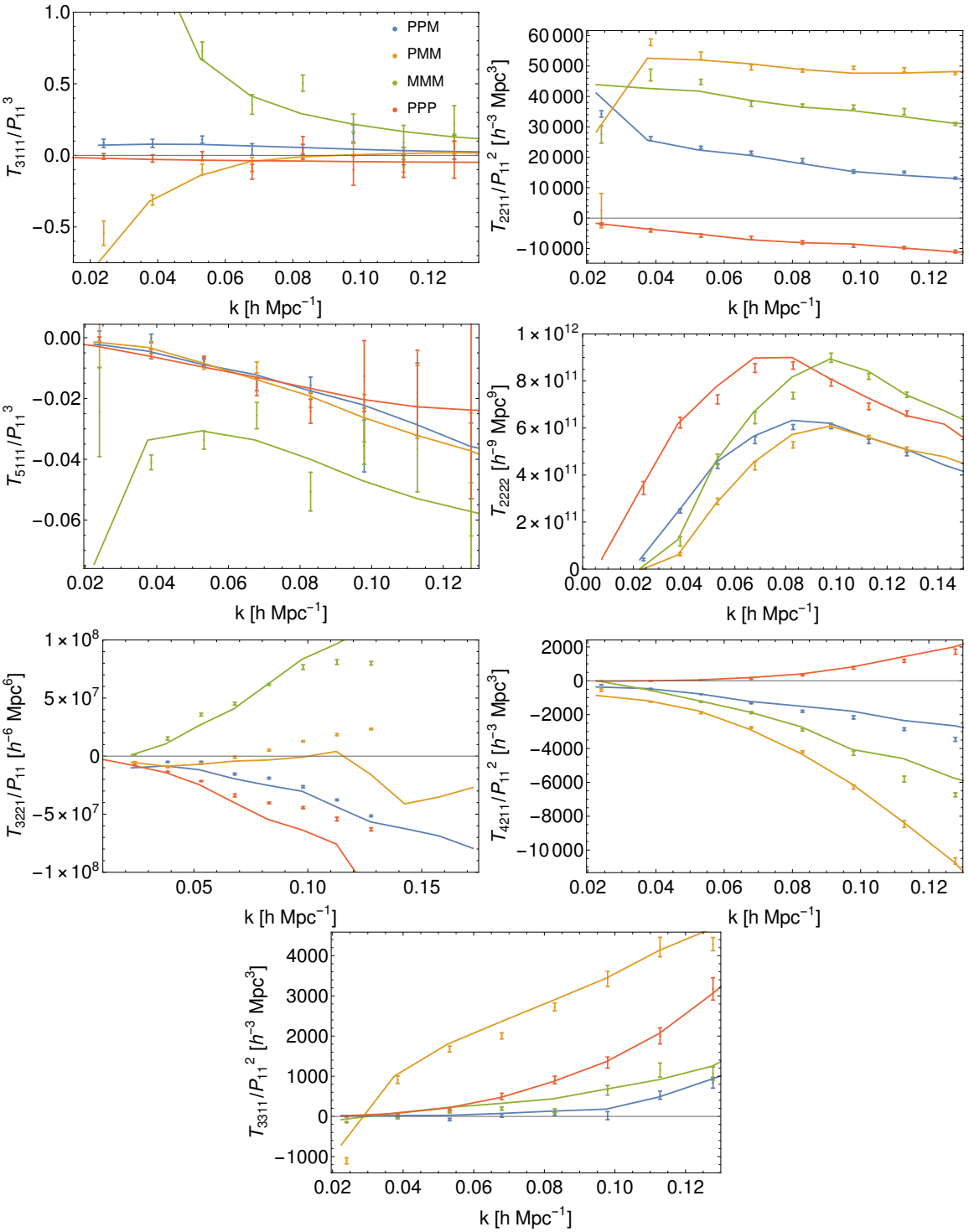

Figure 9.5: The contributions to the one-loop trispectrum after undergoing CVC through the removal of power spectra as measured in gridPT (points) against the calculations from standard perturbation theory (lines) with a cutoff of $\Lambda = 0.3h$ Mpc^{-1}. The blue line is configuration PPM, the yellow line is PMM, the green line is MMM and the red line is PPP.

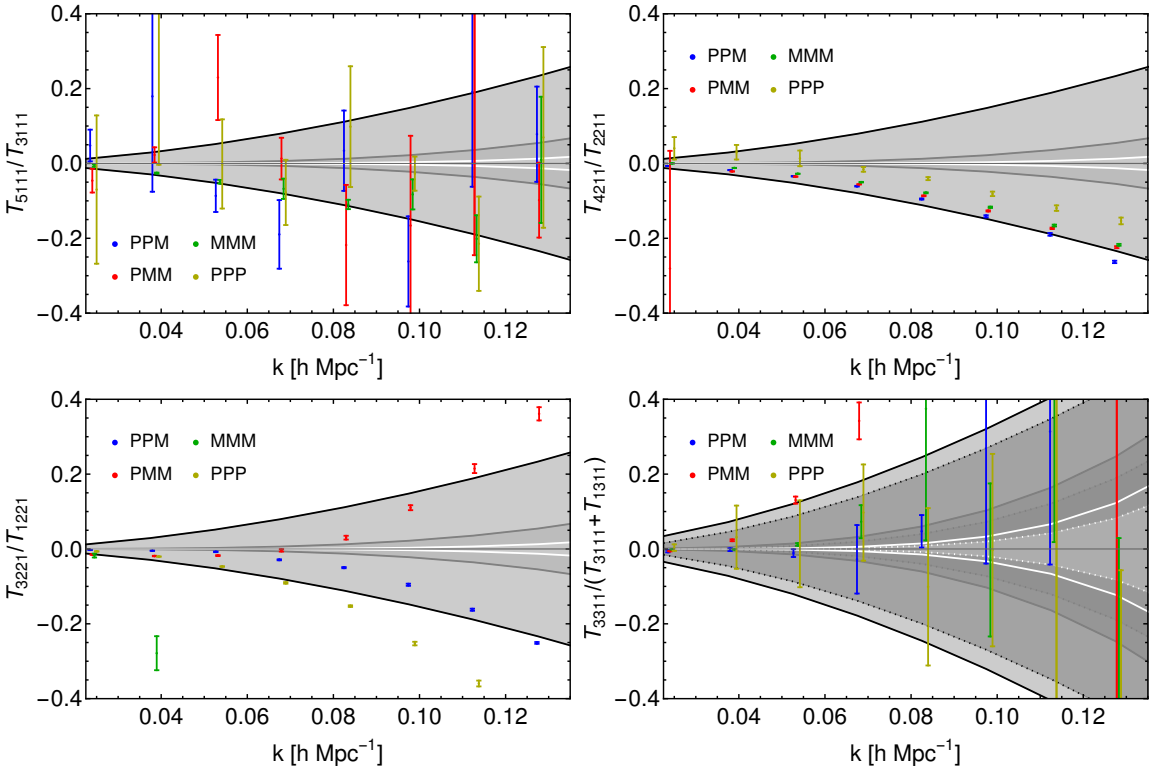

Figure 9.6: The theoretical errors at one (black), two (grey), and three (white) loops for the ratios one loop terms and their corresponding tree level terms in the four configurations considered. In the case of T_{3311}, the loop momentum is an average of k_1 and k_2 such that the configurations PPM, PMM, and PPP have the same theoretical errors while those of MMM differ; those for MMM are shown as dotted lines while those for the other configurations are shown as solid.

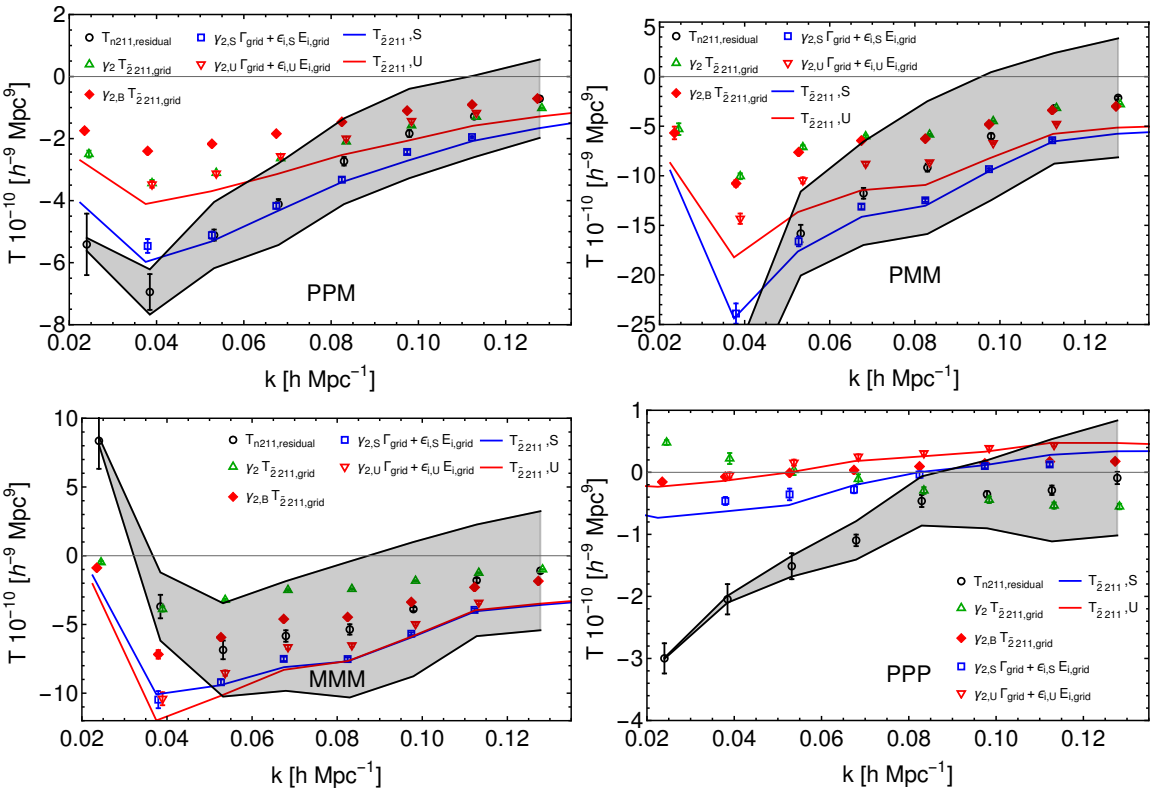

Figure 9.7: The calculated counterterms $T_{\tilde{2}211}$ with $\tilde{F}_2$ as calibrated from the bispectrum against the grid residual for configurations PPM (top left), PMM (top right), MMM (bottom left), PPP (bottom right). The grey shaded region shows the theoretical error induced by two-loop corrections. We apply a growth factor correction of $\Delta D_2 \approx 0.005$ inspired by our bispectrum measurements from Chapter 8 to account for time integration inaccuracies in the N-body results.

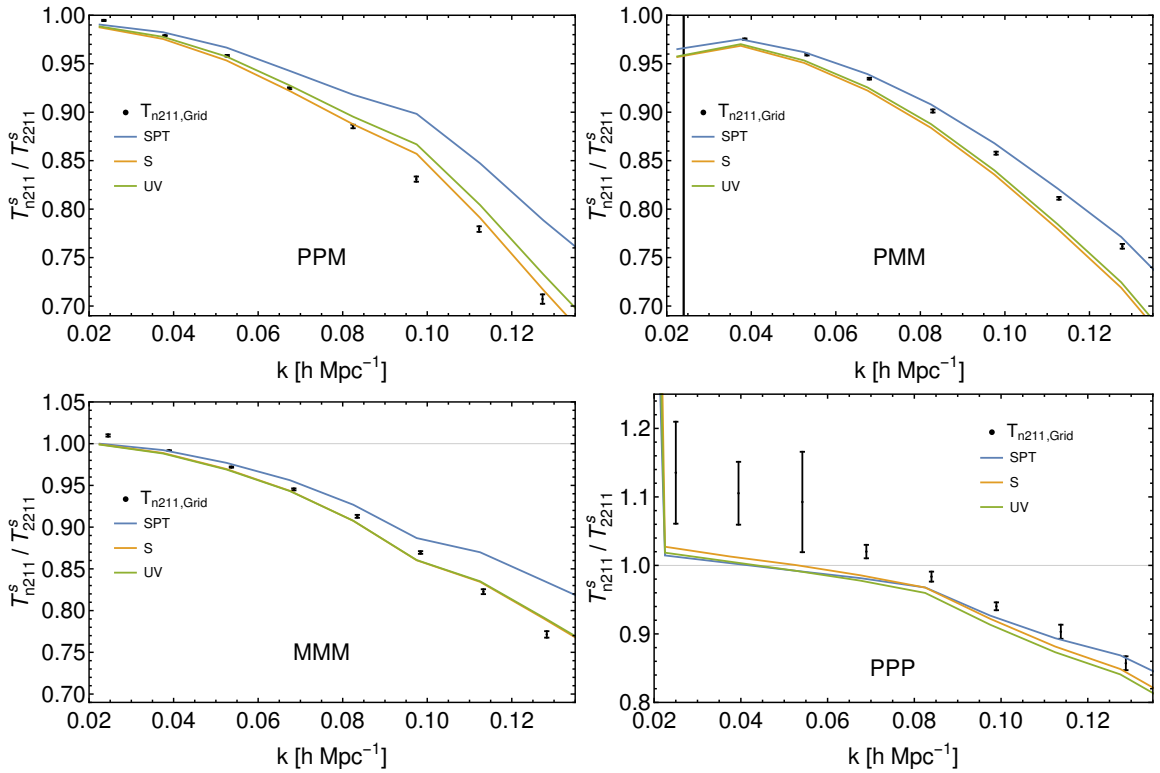

Figure 9.8: The calculated $T_{2211} + T_{4211} + T_{\tilde{2}211}$ with $\tilde{F}_2$ as calibrated from the bispectrum against the grid $T_{\mathrm{n}211} - T_{3211} - T_{1211}$ for the four configurations studied. For PPM and MMM, the corrections are significant. In the former case it is notable that the symmetry inspired fit works better than the UV inspired fit, a relation that was also seen in the study of the bispectra, while for MMM the two parametrisations of the counterkernel seem to work equally well. For PMM, the correction seems to be too large and is of debatable value, while for PPP the correction is extremely small. As this is a ratio over the tree-level terms, only studying perturbation theory up to tree level would have resulted in a constant line at one. Configurations PPM, PMM, and MMM can only be described by this at the largest scales, deviating from one already by $k \sim 0.03h$ Mpc^{-1}, while the measurements in configuration PPP do not agree with tree level predictions at any scale.

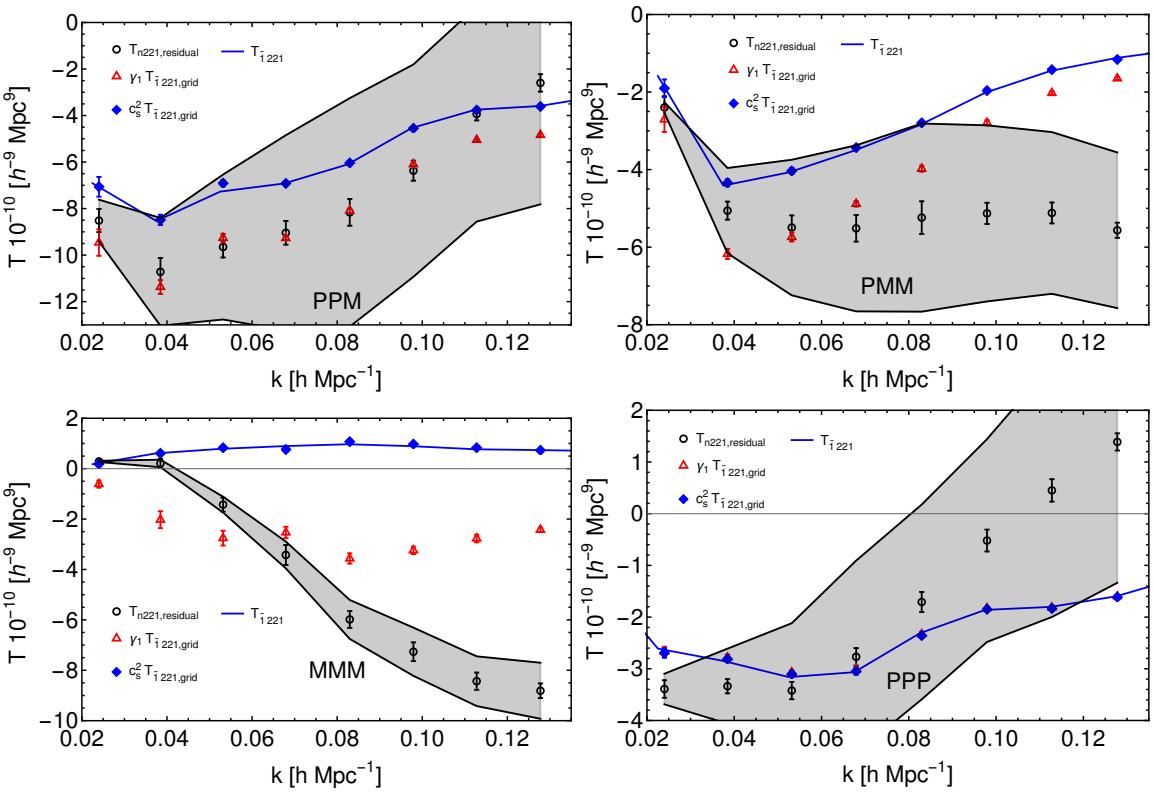

Figure 9.9: The calculated counterterms $T_{\tilde{1}221}$ with $\tilde{F}_1$ as calibrated from the bispectrum against the grid residual for configurations PPM (top left), PMM (top right), MMM (bottom left), PPP (bottom right). The grey shaded region shows the theoretical errors for the two loop contributions. We can see that the results work well for PPM, particularly with the amplitude fitted to the grid counterterm. However, for the other configurations, particularly MMM, the counterterms fitted less well with the measured residuals.

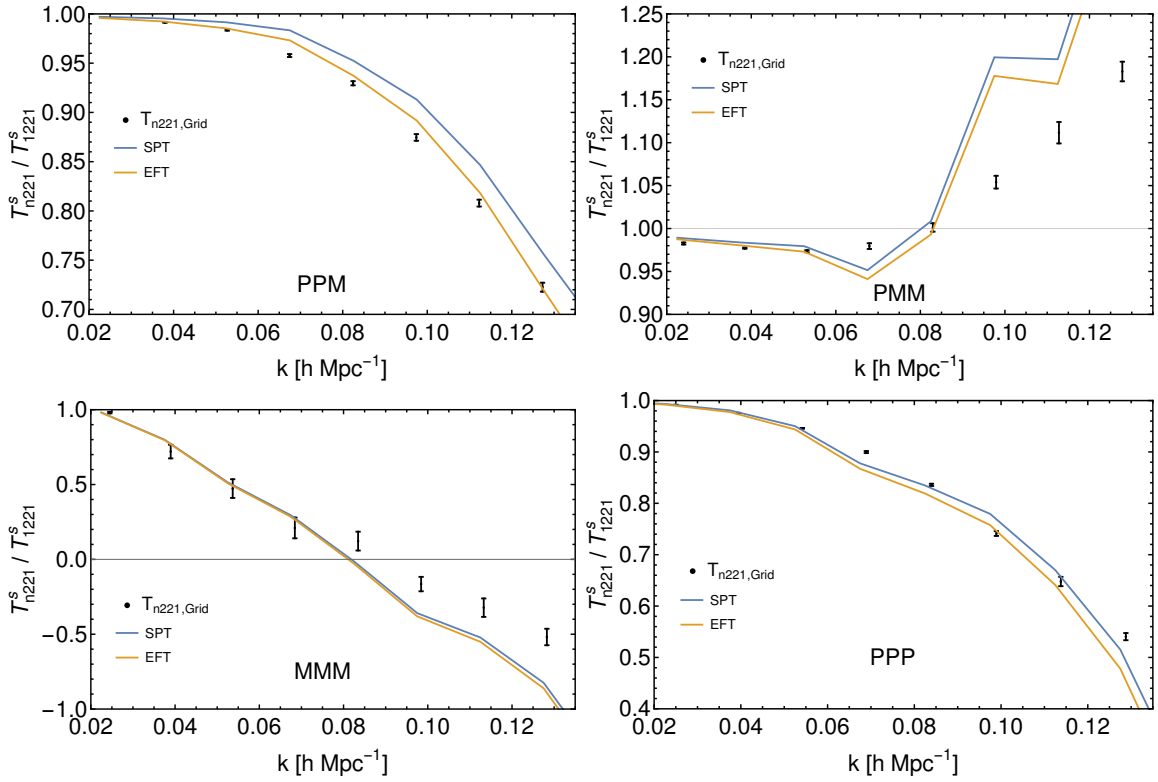

Figure 9.10: The calculated $T_{1221} + T_{3211} + T_{\tilde{1}221}$ with $\tilde{F}_1$ as calibrated from the bispectrum against the grid $T_{\mathrm{n221}} - T_{2221}$ for the four configurations studied. The tree-level trispectrum corresponds to a horizontal line at one. The measurements clearly deviate from that starting from the largest scales for configurations PPM and PMM, with PPM and PPP deviating from tree level beginning at least at $k \sim 0.03h$ Mpc^{-1}.

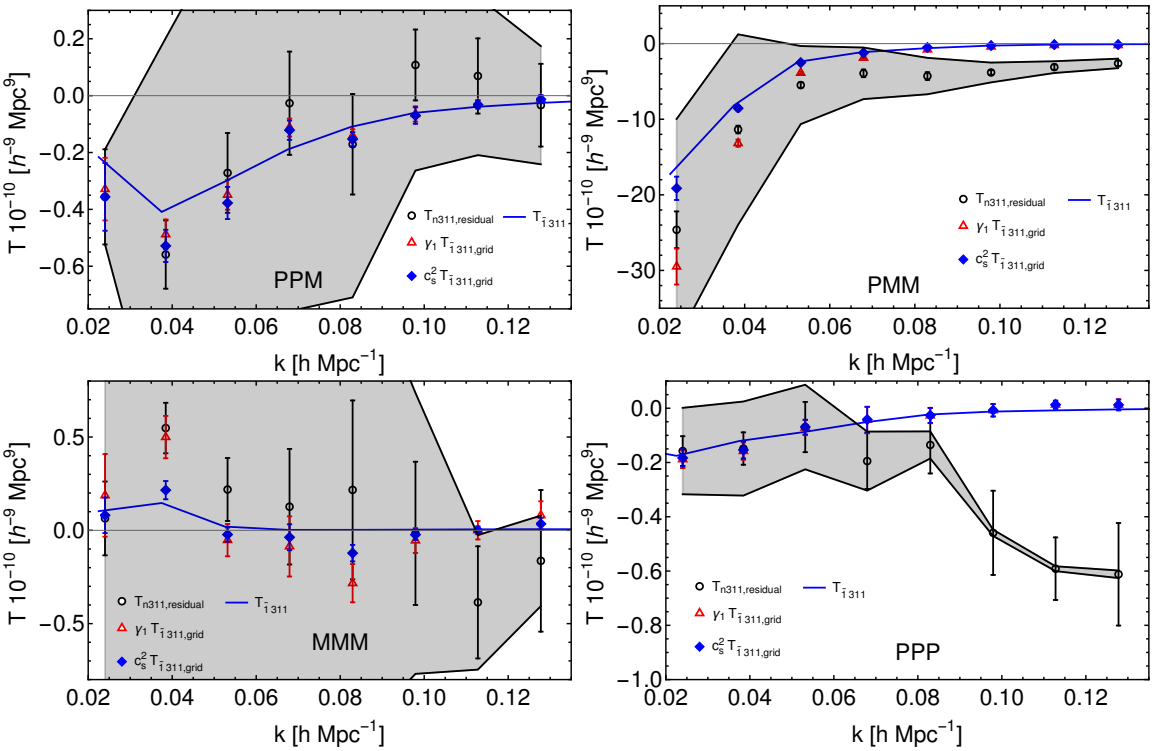

Figure 9.11: The theoretical counterterm $T_{\tilde{i}311}$ with $\tilde{F}_1$ as calibrated from the bispectrum against the grid residual for configurations PPM (top left), PMM (top right), MMM (bottom left), PPP (bottom right). The grey shaded region shows the theoretical error for the two loop contributions. For all configurations, we see that the grid counterterms, multiplied by some amplitude, fit well with the measured residuals at large scales. For all configurations except MMM, we see the same for the analytically estimated $T_{\tilde{i}311}$.

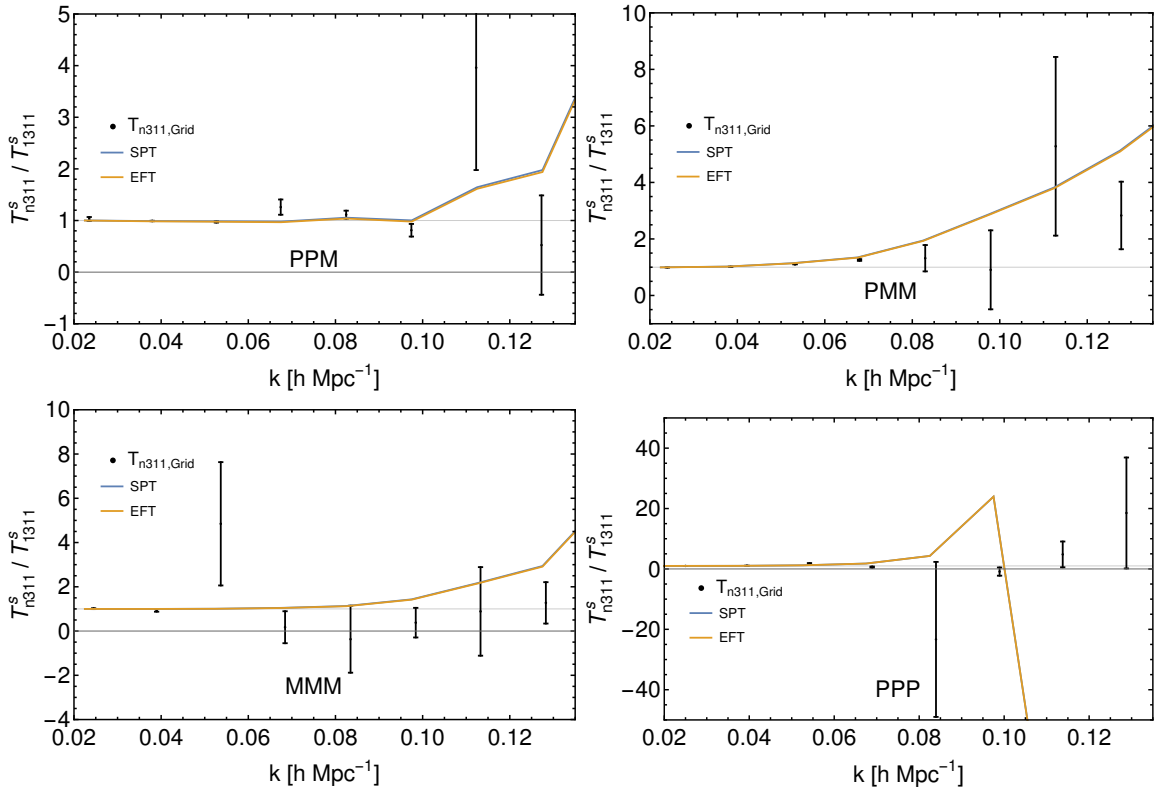

Figure 9.12: The calculated $T_{1311} + T_{3311} + T_{\tilde{1}311}$ with $\tilde{F}_1$ as calibrated from the bispectrum against the grid $T_{\mathrm{n}311} - T_{2311}$ for the four configurations studied. We see that the counterterm estimated here was extremely small and made a subleading correction, such that the EFTofLSS results are almost indistinguishable from the SPT results. Given the small sizes of the measured residuals for the four configurations studied, this could simply be because a larger correction was not required. Note that this is a ratio over the residual, so if we had only studied perturbation theory up to tree level we would have predicted a constant line at one. Unlike the other terms we have measured, $T_{\mathrm{n}311}$ does seem to be consistent with tree level up to about $k \sim 0.06h$ Mpc^{-1} for all studied configurations, which could explain the extremely small size of the EFTofLSS corrections.

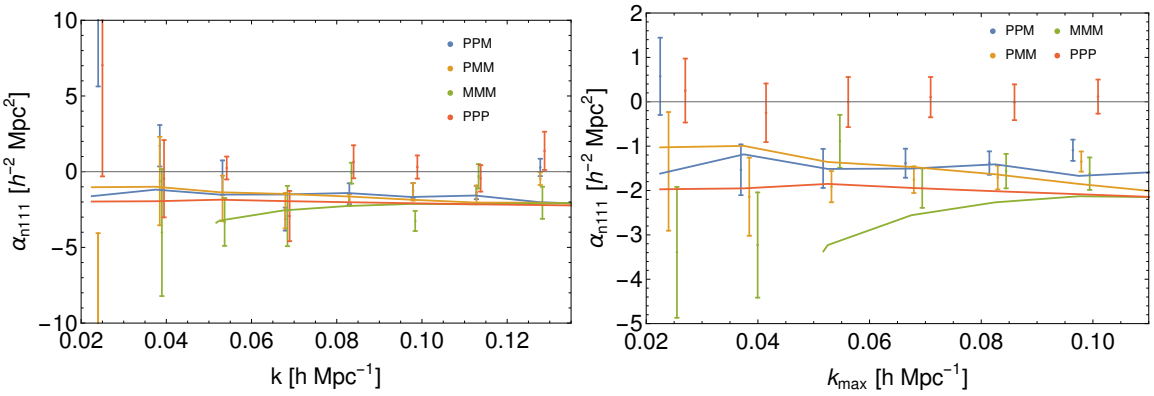

Figure 9.13: *Left hand panel:* α_{n111} calculated at each point in isolation. *Right hand panel:* The χ^2 minimisation up to k_{max} of the same. We can see that the counterterm parameter takes values of the expected order of magnitude for all configurations except PPP, in which it is consistent with zero.

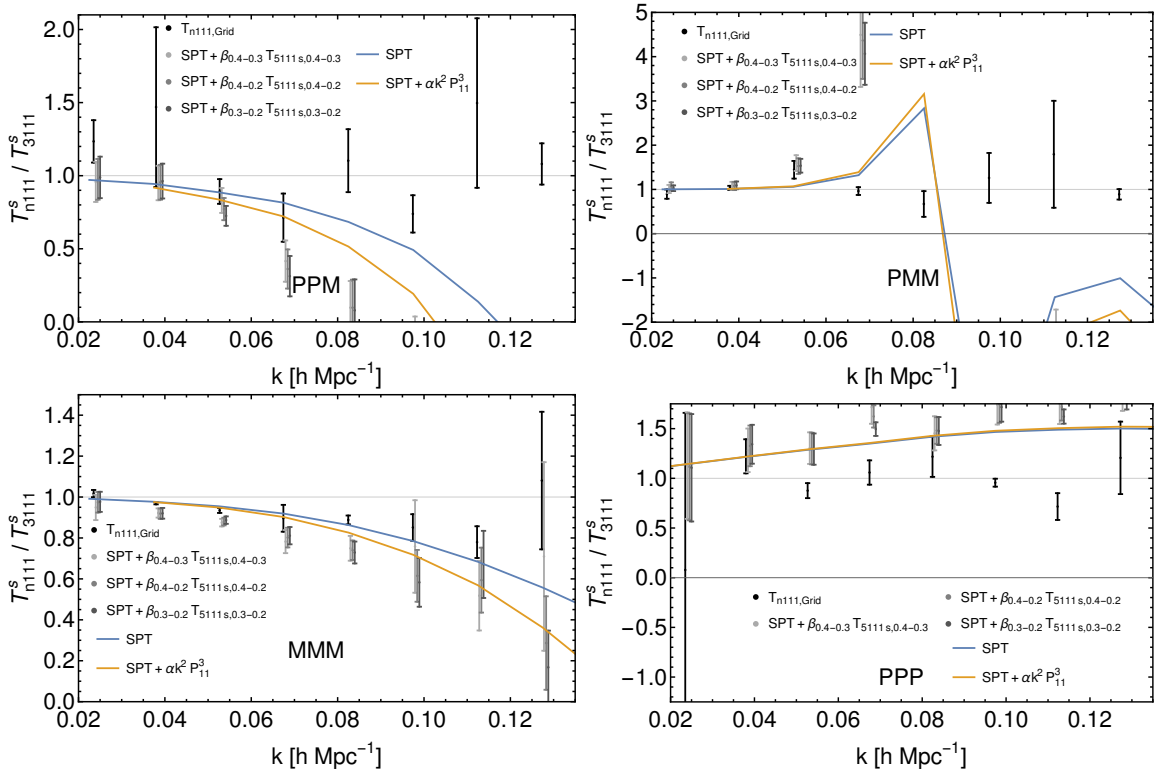

Figure 9.14: The calculated $T_{3111} + T_{5111} + T_{\tilde{3}111}$ with $\tilde{F}_3$ as calibrated from the bispectrum against the grid $T_{\mathrm{n}111} - T_{4111} - T_{2111} - T_{1111}$ for the four configurations studied. In all cases the measured trispectra had $\Lambda = 0.3h$ Mpc^{-1} except those used for calculating the β parameters which had the cutoffs represented in those parameters' subscripts. The parameters were taken as those with the values $k_{\mathrm{max}} = 0.08h$ Mpc^{-1}. Note that this is a ratio over the tree-level terms such that, had we only studied perturbation theory up to tree level, we would have a constant line at one. It is noticeable that this would not have given up an accurate estimator for $T_{\mathrm{n}111}$ in configurations PPM and MMM, but would have sufficed up to even $k \sim 0.1h$ Mpc^{-1} for PPM and PPP, perhaps explaining the smaller sizes of the EFTofLSS corrections in those configurations.

10

Concluding Remarks

10.1 | Discussion

In this thesis, we performed a precise calibration and test of the one-loop bispectrum and trispectrum and their counterterms in the framework of the EFTofLSS. This work was published in two papers [27, 28] and is presented here with a review of the relevant areas of physics.

The EFTofLSS provides the most accurate analytic model of large scale structure to date, but is still in its infancy; if the results of near future surveys such as LSST and SPHEREx are to be fully exploited, the model must be developed much further such that the limits of its precision approach the limits imposed by their data sets. Until our recent publications, research on the EFTofLSS had primarily relied upon the EdS approximation, in which all perturbative density fields are modelled as though they were growing in a matter only universe. While this is not an accurate model of our real cosmology, it has been taken to be a valid approximation, with the differences between EdS and ΛCDM cosmology in the case of the one-loop power spectrum being accounted for with a slight modification to the value of the counterterm $P_{\tilde{1}1}$. In [27], we showed that, while the EdS approximation is indeed valid up to one-loop order in studies of the power spectrum, it leads to significant deviations from the correct ΛCDM results in studies of the one-loop bispectrum, and in [28] we extended this to show that these deviations also show in studies of the one-loop trispectrum. As such, we have shown that it is essential to use the correct growth factors when defining perturbative density fields for correlators of higher order than two and have used such ΛCDM terms to provide the first accurate and precise calibration of the one-loop bispectrum and trispectrum counterterms.

Using the method of gridPT, we have been able to reduce the systematic imprecisions that affect most EFTofLSS calibrations by ensuring that all contributions to the perturbative

approximation of all non-linear correlators are divided into identical momentum bins, as well as allowing us to remove the non-zero measurements of odd correlators that occur in finite spaces. The combination of both effects leads to a sufficient reduction on the error bars to allow for the detection of the sub-leading corrections we are after. We have confirmed that this cosmic variance cancellation significantly reduces the magnitudes of the resultant error bars for the parameter constraints. This cosmic variance cancellation enables the estimation of EFTofLSS parameters from smaller simulation volumes. The realisation perturbation theory approach would thus be uniquely suited to constrain the EFTofLSS parametrisation of baryonic physics [71] from numerically demanding, small-volume hydrodynamic simulations.

GridPT also allowed us to study partially non-linear correlators, isolating individual counterterms and allowing their parameters to be calibrated separately; in theory, this should provide more robust results for each counterterm than a full calibration of the model from a fully non-linear correlator, as it ensures that the effects of any degeneracy between counterterms is minimised, as well as proviidng an alternative way of calibrating each counterterm for the purposes of cross-validation. Thus, for the first time, we have considered the bispectrum propagator terms $B_{\rm n11}$ and $B_{\rm n21}$ and the trispectrum propagator terms $T_{\rm n111}$, $T_{\rm n221}$, and $T_{\rm n311}$ in this context.

While studying the bispectrum, we found evidence for non-zero correction terms even at order k^0 in the EFT. These corrections are artifacts of the numerical integration of the N-body system, most likely round off and time stepping issues. Allowing for these bias-like terms leads to more consistent results for the actual EFTofLSS counterterms at order k^2 on large scales. While the k^0 terms are a nuisance parameter for our purposes, their detection on large scales can be used as a diagnostic for simulation accuracy. However, we did not find that these corrections assisted in providing more accurate trispectrum calibrations, a result which we attribute to the already imprecise nature of the trispectral calculations, which were not precise enough to warrant the incorporation of such new terms and were plagued with enough noise that they simply led to the model having additional degrees of freedom in which to accommodate noise.

In the case of the bispectrum, the reduced χ^2 clearly shows that the multiple parameter models tend to provide better fits to the measurements over a wider k-range than the UV inspired parametrisations. We take this to show that the single parameter approximation of the $\tilde{F}_2$ counterkernel is less effective at capturing the simulation residuals of the one-loop bispectrum than the symmetry inspired counterkernel with three free parameters. We found that the isolated counterterm calibrations (from $B_{\rm n11}$ and $B_{\rm n21}$) were less well fitted than the combined calibrations from the auto bispectrum $B_{\rm nnn}$. We take this to indicate that

the unsymmetrised $B_{\mathrm{n}11}$ and $B_{\mathrm{n}21}$ bispectra are more sensitive to contaminations than B_{nnn} where they are averaged out by symmetrisation. We find that the measurements of γ_2 are mostly compatible with the power spectrum value of $c^2_{\mathrm{s},\infty} = 1.2h^{-2}\,\mathrm{Mpc}^2$. Future work should investigate the impact of the full ΛCDM time dependence and full covariance matrix. We have considered the latter but found that our simulation suite is too small to get reliable estimates of the covariance matrix after cosmic variance cancellation. The leading non-Gaussian covariance of the bispectra without CVC could be estimated from perturbation theory on the grid [65], but after subtracting the perturbative orders, the remainder is dominated by high orders in perturbation theory and the stochastic contributions. The poor χ^2 obtained in our fits to the propagator terms suggests that IR-resummed operators, such as those motivated by Lagrangian perturbation theory [72, 73] might be beneficial to improve the agreement between theory and simulations.

In the case of the trispectrum, we have found that a simple single parameter approximation for the counterkernel $\tilde{F}_3$ was sufficient to regularise the one-loop residual of $T_{\mathrm{n}111}$. This counterterm for T_{5111} is a new interaction uniquely probed by the trispectrum but not by the power spectrum and bispectrum. Calibrations of $\tilde{F}_1$ and $\tilde{F}_2$ taken from the one-loop bispectrum were able to successfully regularise the one-loop residuals of $T_{\mathrm{n}211}$, $T_{\mathrm{n}221}$, and $T_{\mathrm{n}311}$. Even after finding methods that could regularise each term, we found that our ability to calculate the counterterms was heavily configuration dependent, with some configurations being much harder to regularise than others, and that our results often only worked on the largest physical scales. We have proposed a number of possible explanations for this, including the notion that higher order terms, both multi-loop and noise terms, could be having a larger impact on the one-loop trispectra than they have on the one-loop bi- and power spectra, or that there may be interference from numerical errors in the simulations. Nonetheless, our results offer the first successful regularisation of the one-loop trispectrum in the EFTofLSS and have been shown to be successful for most configurations up to a non-trivial maximum wavenumber k_{max}.

While our study of the trispectrum was being finalized, [74] presented a detailed measurement of the trispectrum from a suite of 5000 simulations and assessed the trispectrum's potential to improve constraints on primordial non-Gaussianity. Within their error bars the tree-level calculation suffices to describe the trispectrum. Our significantly smaller error bars however, allow us to show that loop corrections significantly improve the modelling of the trispectrum.

We leave it to a future paper to study the full configuration space of the trispectrum and to constrain the parameters of the stress tensor explicitly. We also leave it to a future paper to study the full trispectrum with all of its counterterms being constrained simultaneously

in a manner analogous to our $B_{\rm nnn}$ methods in [27]. In particular, we will be investigating whether or not using these new methods will allow us to overcome the problems encountered in this paper.

In conclusion, we have shown that using a series of novel techniques, including the use of the accurate ΛCDM growth factors for the perturbative density fields, the direct testing of UV approximations, and the use of the gridPT method to ensure identical binning for terms being compared to one another, the higher order correlators of the EFTofLSS can be used to place highly precise calibrations on the EFTofLSS counterterms and, by extension, can be used in conjunction with survey data to break degeneracies in studies of the power spectrum and place significant constraints on various fundamental physical parameters.

10.2 | Alternatives to the EFT

While a promising avenue of research that has been progressed by the research presented in this thesis, the EFTofLSS is far from the only accurate model of LSS being used in present day cosmology. In this subchapter we will briefly review some of the alternative models of LSS and how they compare to the EFT and conclude that all such methods are best used in conjunction with one another to cross-check results and break one another's degeneracies.

Viscous Perturbation Theory

Perturbation theory with viscous dark matter was first proposed in [75] and differs from the EFT in that the new terms it introduces to account for small scale phenomenon are viscosity and pressure terms, rather than an entire symmetry based stress-energy tensor. This results in an alternative formulation which contains no free parameters and is thus significantly simpler to formulate at higher loop orders.

Viscous perturbation theory is a viable alternative to the EFT on large scales and generates similarly accurate descriptions of LSS observations up to $k \sim 0.2h\text{Mpc}^{-1}$ at two loops. However, it remains to be tested which of the two models is able to be used on the smallest real space scales.

As an alternative formulation of the same mathematical framework and an alternative description of the same physics, I would primarily suggest that viscous perturbation theory be developed synchronously with the EFT and that there results be used to cross-check one another; given their similarities, such joint research could provide an intrinsic test of validity without requiring multiple entirely different formalisms to be generated and used simultaneously.

Time Sliced Perturbation Theory

Time Sliced Perturbation Theory (TSPT) was first suggested in [76] as an alternative way of analytically estimating cosmological correlation functions which is entirely different in formulation from SPT and its developments.

TSPT begins with a time-dependent probability distribution function which serves to estimate correlators. This function can be expanded in a manner that permits a perturbative formulation. This method is free of the infrared divergences which must be explicitly corrected for in the EFT and was developed to provide a suggested method for solving these problems. However, it also constitutes an alternative model of LSS in its own right and has the potential to be used alongside the EFT such that they may be used to cross check one another's results.

Counts-in-Cells

The Counts-in-Cells (CIC) [77] approach is an alternative method of analysing LSS data which does not concern itself with correlators but rather divides space into equally sized cells and estimates the number of tracers that are to be found in each cell.

This method has been shown to be able to cross check the results of correlator studies as well as being able to break their degeneracies, as was demonstrated by a recent study of cosmic shear [78].

The CIC method is a model of LSS which is different enough from the EFT that it could be used to provide highly robust cross checks as well as a potentially significant breaking of degeneracies. I would suggest that in future, it be used to study the same survey data as the EFT and that the results provided by the two methods be compared, as this may yield not only a robust confirmation of each method's results, but also a chance for a significant increase in the precision of their parameter inferences.

10.3 | Summary

In this final chapter we have reviewed the nature, results, and conclusions of the research presented in this thesis and have discussed alternative models and how they can be used in conjunction with the EFTofLSS for optimal results. The conclusions from our research ultimately constituted a development of the ability of the EFTofLSS to describe correlators beyond the one-loop power spectrum with sufficient precision to be used for meaningful constraints when compared with current and near future survey data, such as the forthcoming results of the LSST and SPHEREx missions.

The results presented in this thesis constitute the first high precision calibration of the counterterm parameters for higher order correlators than the power spectrum in the EFTofLSS. Furthermore, as these calibrations were being made, a number of assumptions, approximations, and solutions to systematic errors were proposed and tested which will be of use in future studies of correlators of all orders. This research therefore significantly enhances the existing analytic framework that is used to analyse LSS surveys, as its results not only allow a new cosmological observable to be predicted with enough precision to potentially break degeneracies that arise when studying the power spectrum, but also because it demonstrated that a number of common assumptions used in analytic studies of LSS, such as the notion that the EdS approximation of density field growth is sufficient in a ΛCDM universe beyond the one-loop power spectrum or that the UV limit of loop terms can consistently be used as an estimator for the corresponding counterterms, are only valid in certain circumstances and has included a detailed analysis of how to improve upon these approximations in others.

Thus, the research presented in this thesis constitutes a non-trivial progression in our understanding of how to analytically describe the large scale structure of the Universe and will be useful both directly and indirectly in future research papers, both those which seek to further the analytical models examined herein and those which seek to apply these findings to the analysis of observed cosmological data.

A

Cosmological Horizons

One of the immediate consequences of introducing the notion of an expanding Universe is that this expansion will interfere with signal propagation; namely, it will take light longer to travel between two points if the distance between them is expanding than if it were not. Indeed, the rate of expansion between sufficiently distantly spaced objects exceeds the speed of light, such that the regions in question are out of causal contact with one another. There are two distances which we label horizons in cosmology: the particle horizon, $r_{\rm p}$, which is the maximum distance light could have travelled by time t if it were emitted at the dawn of the Universe:

$$r_{\rm p} = \int_0^t \frac{dt'}{a(t')} \,, \tag{A.1}$$

and the event horizon, $r_{\rm e}$, which is the greatest distance light that is emitted now will be able to travel before any hypothesised end of the universe event, labelled with time $t_{\rm end}$:

$$r_{\rm e} = \int_t^{t_{\rm end}} \frac{dt'}{a(t')} \,. \tag{A.2}$$

While the event horizon is useful primarily in studies of late time effects, such as dark energy and modified gravity theories, as it provides an important example of a physical parameter they will affect, the particle horizon plays an important role in past and present time cosmology. The fact that light can only have propagated a finite distance between the beginning of the Universe and the present time means that there is a maximum distance out to which we can see; any events which occur beyond this distance are out of causal contact with any events of our past events and the transition of large scale dynamical fields from superhorizon scales, those being scales greater than $r_{\rm p}$, to subhorizon scales, which are those less than $r_{\rm p}$ and which therefore described objects and events in causal contact with one another, plays an important role in the evolution of the structure of the Universe.

B

Parameter Inference

The EFT models used in this study are linear in the parameters. In this Appendix we will briefly review the derivation of the Fisher matrix for a generic linear model before showing how it can be used to calculate the cross-correlation of any two parameters from that model and the error bars of any given parameter. We will consider a measurement $\boldsymbol{B}_{\rm meas}$ with a diagonal covariance matrix and variance $\boldsymbol{\Delta B}^2_{\rm meas}$ and a generic theory model that is linear in the parameters such that $\boldsymbol{B}_{\rm model} = \sum_i \alpha_i \boldsymbol{B}_{{\rm model},i}$. Assuming Gaussian errors, we thus have

$$\chi^2 = \sum_{k_s=k_{\rm min}}^{k_{\rm max}} \frac{\left[B_{{\rm meas},s} - \sum_i \alpha_i B_{{\rm model},i,s}\right]^2}{\Delta B^2_{{\rm meas},s}} \,. \tag{B.1}$$

Taking the first derivative of Eq. (B.1) with respect to any given parameter α_i gives us

$$\frac{{\rm d}\chi^2}{{\rm d}\alpha_i} = 2 \sum_{k_s=k_{\rm min}}^{k_{\rm max}} B_{{\rm model},i,s} \frac{B_{{\rm meas},s} - \sum_j \alpha_j B_{{\rm model},j,s}}{\Delta B^2_{{\rm meas},s}} \,. \tag{B.2}$$

Setting this first derivative to zero gives us the linear system

$$\sum_{k_s=k_{\rm min}}^{k_{\rm max}} \frac{B_{{\rm model},i,s} B_{{\rm meas},s}}{\Delta B^2_{{\rm meas},s}} = \sum_j \alpha_j \sum_{k_s=k_{\rm min}}^{k_{\rm max}} \frac{B_{{\rm model},i,s} B_{{\rm model},j,s}}{\Delta B^2_{{\rm meas},s}} \,. \tag{B.3}$$

Taking the second derivative of which for any given parameters α_i and α_j gives us

$$\frac{{\rm d}^2\chi^2}{{\rm d}\alpha_i {\rm d}\alpha_j} = 2 \sum_{k_s=k_{\rm min}}^{k_{\rm max}} \frac{B_{{\rm model},i,s} B_{{\rm model},j,s}}{\Delta B^2_{{\rm meas},s}} \equiv \mathscr{F}_{ij} \,, \tag{B.4}$$

where $\mathscr{F}$ is the Fisher matrix of the model in question.

We can now calculate the cross-correlation of any two parameters by looking at the ratio between the product of their isolated elements in the inverse Fisher matrix and their combined element, as given by

$$C_{ij} = \frac{\mathscr{F}_{ij}^{-1}}{\sqrt{\mathscr{F}_{ii}^{-1}\mathscr{F}_{jj}^{-1}}} \,. \tag{B.5}$$

A strong cross-correlation, that being $C_{ij} \approx 1$ or $C_{ij} \approx -1$, means that the parameters α_i and α_j are degenerate; they correlate so strongly with one another that only one of the two is needed to determine the value of them both and allowing them both to vary freely will result in results for the individual parameters that differ markedly from those of non-degenerate parametrisations of the same functions as the model is effectively being allowed to vary one parameter in two different ways simultaneously. However, it is important to note that while degenerate parameters may give differing results for their parameters, they can still give accurate fits for the overall model.

We can also calculate the error bars for any given parameter as

$$\sigma_i = \sqrt{\mathscr{F}_{ii}^{-1}} \tag{B.6}$$

and it is this definition that we use for the error bars in the figures for $\gamma_{1,2}$ and $\varepsilon_{1,2,3}$ in Chapter 8.

C

Fitting Procedure Validation

To validate our fitting and modelling procedure, we use the B_{411} measurement for two different cutoffs as a reference propagator measurement for which we know the exact values of the counterterm amplitude. By applying our fitting procedure to this artificial data set, we can check that our templates are correctly normalised and assess the expected error bars.

We generate our benchmark density field by calculating the difference between the fourth order density fields generated from linear density fields with two different wavenumber cutoffs Λ_1 and Λ_2

$$\delta_{4,\mathrm{S}}(k_1,k_2,k_3;\Lambda_1,\Lambda_2) = \delta_4(k_1,k_2,k_3;\Lambda_1) - \delta_4(k_1,k_2,k_3;\Lambda_2)\,. \tag{C.1}$$

Since we are calculating a 411 correlator, this is equivalent to calculating the difference between the respective bispectra

$$B_{411,\mathrm{S}}(k_1,k_2,k_3;\Lambda_1,\Lambda_2) = B_{411}(k_1,k_2,k_3;\Lambda_1) - B_{411}(k_1,k_2,k_3;\Lambda_2)\,. \tag{C.2}$$

Replacing the residual in the numerator of Eq. (8.28) with $B_{411,S}$ gives us

$$\chi^2_{\mathrm{n11,test}}(k_{\mathrm{max}}) = \sum_{k_{1,2,3}=k_{\mathrm{min}}}^{k_{\mathrm{max}}} \frac{\left[B_{411,\mathrm{S}}(k_1,k_2,k_3;\Lambda_1,\Lambda_2) - B_{\tilde{2}11}(k_1,k_2,k_3;\gamma_2,\varepsilon_i)\right]^2}{\Delta B^2_{\mathrm{n11}}(k_1,k_2,k_3)}. \tag{C.3}$$

There is no need for the ΔD_1 and ΔD_2 corrections in this case. From Eqs. (8.21) and (8.23) we can see that the results of the minimisation of Eq. (C.3) will give values of

$$\gamma_2 \approx \frac{61}{210}\left[\sigma^2_{\mathrm{d}}(\Lambda_1) - \sigma^2_{\mathrm{d}}(\Lambda_2)\right]\,, \tag{C.4}$$

with the ε_i parameters being defined as in Eq. (8.24).

The comparison of this analytic calculation with the numerical minimisation can be used as a test of the counterterm implementation and of the minimisation infrastructure. A calculation with $\Lambda_1 = 0.3h$ Mpc^{-1} and $\Lambda_2 = 0.2h$ Mpc^{-1} shows that they do indeed produce the correct results of γ_2 at the $k_{\max}$ values of interest.

If our trispectrum routines are properly calibrated, we should expect the scale dependent $T_{5111,\mathrm{S},i-j}$ to scale as $k^2P_{11}^3$. As shown in Fig. C.1, we find that for the three possible combinations of trispectra with $\Lambda\varepsilon\{0.2, 0.3, 0.4\}h$ Mpc^{-1}, we have that

$$T_{5111}(\Lambda_2) - T_{5111}(\Lambda_1) \approx -0.5k^2P^3 \ . \tag{C.5}$$

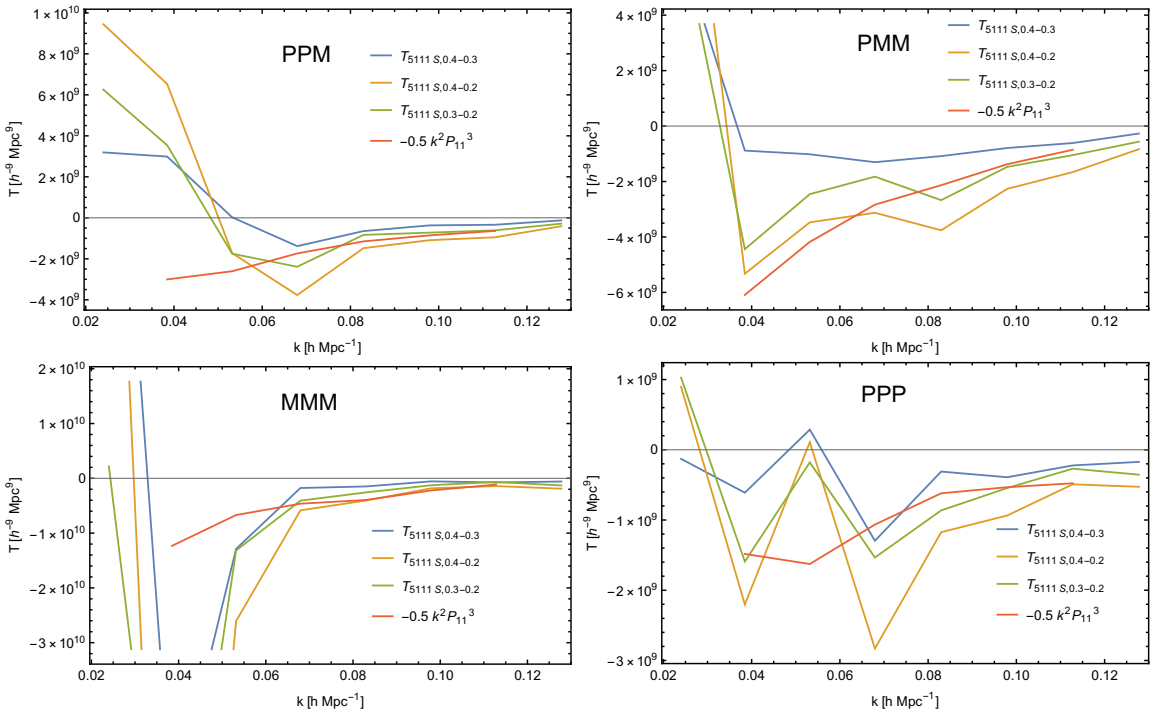

Figure C.1: The measured $T_{5111\mathrm{s},i-j}$ for three combinations of cutoffs against $-0.5k^2P_{11}^3$, showing the similar scaling. This constitutes a validation of the calibration of our measurements and calculations, showing that the terms scale as they would be expected to.

D

Generalised Trispectrum Estimators

While Eq. (6.10) integrates over the four external legs and allows the diagonals to vary, which is what we do for the four configurations we are going to focus on, we also developed equivalent algorithms for other forms of configuration. Eq. (D.1) allows us to measure a trispectrum configuration which has one diagonal leg fixed and is only allowing the other to vary, giving only one unspecified degree of freedom,

$$\begin{aligned}
\hat{T} &= \frac{1}{\mathscr{N}} \int \frac{\mathrm{d}^3 k_1^i}{(2\pi)^3} \int \frac{\mathrm{d}^3 k_2^i}{(2\pi)^3} \int \frac{\mathrm{d}^3 k_3^i}{(2\pi)^3} \int \frac{\mathrm{d}^3 k_4^i}{(2\pi)^3} \int \frac{\mathrm{d}^3 k_5^i}{(2\pi)^3} \, (2\pi)^6 \\
&\quad \times \delta^{(\mathrm{D})}(k_1^i + k_2^i - k_5^i) \delta^{(\mathrm{D})}(k_3^i + k_4^i + k_5^i) \delta(k_1^i) \delta(k_2^i) \delta(k_3^i) \delta(k_4^i) \\
&= \frac{1}{\mathscr{N}} \int \mathrm{d}^3 x^i \int \mathrm{d}^3 x^j \int \frac{d^3 k_1^i}{(2\pi)^3} \int \frac{\mathrm{d}^3 k_2^i}{(2\pi)^3} \int \frac{\mathrm{d}^3 k_3^i}{(2\pi)^3} \int \frac{\mathrm{d}^3 k_4^i}{(2\pi)^3} \int \frac{\mathrm{d}^3 k_5^i}{(2\pi)^3} \\
&\quad \times e^{ix^i(k_1^i + k_2^i)} e^{-ik_5^i x^i} e^{ix^j(k_3^i + k_4^i)} e^{ik_5^i x^j} \delta(k_1^i) \delta(k_2^i) \delta(k_3^i) \delta(k_4^i) \\
&\equiv \frac{1}{\mathscr{N}} \int \mathrm{d}^3 x^i \int \mathrm{d}^3 x^j \int \frac{\mathrm{d}^3 k_5^i}{(2\pi)^3} \, f_1(x^i) f_2(x^i) f_3(x^j) f_4(x^j) e^{-ik_5^i x^i} e^{ik_5^i x^j} \\
&= \frac{1}{\mathscr{N}} \int \frac{\mathrm{d}^3 k_5^i}{(2\pi)^3} \int \mathrm{d}^3 x^i \, f_1(x^i) f_2(x^i) e^{-ik_5^i x^i} \int \mathrm{d}^3 x^j f_3(x^j) f_4(x^j) e^{ik_5^i x^j} \\
&\equiv \frac{1}{\mathscr{N}} \int \frac{\mathrm{d}^3 k_5^i}{(2\pi)^3} \, f_{12}(k_5^i) f_{34}(k_5^i) \, ,
\end{aligned} \tag{D.1}$$

where k_5^i can trivially be replaced by k_6^i with the appropriate changes in the Dirac functions, while Eq. (D.2) allows us to measure a trispectrum in which all six legs are specified, limiting

us to a single configuration [63]:

$$
\begin{aligned}
\hat{T} = & \frac{1}{\mathscr{N}} \int \frac{\mathrm{d}^3 k_1^i}{(2\pi)^3} \int \frac{\mathrm{d}^3 k_2^i}{(2\pi)^3} \int \frac{\mathrm{d}^3 k_3^i}{(2\pi)^3} \int \frac{\mathrm{d}^3 k_4^i}{(2\pi)^3} \int \frac{\mathrm{d}^3 k_5^i}{(2\pi)^3} \int \frac{\mathrm{d}^3 k_6^i}{(2\pi)^3} \, (2\pi)^{12} \\
& \times \delta^{(\mathrm{D})}(k_1^i + k_2^i - k_5^i) \delta^{(\mathrm{D})}(k_3^i + k_4^i + k_5^i) \times \delta^{(\mathrm{D})}(k_1^i + k_4^i + k_6^i) \\
& \times \delta(k_1^i) \delta(k_2^i) \delta(k_3^i) \delta(k_4^i) \\
= & \frac{1}{\mathscr{N}} \int \mathrm{d}^3 x^i \int \mathrm{d}^3 x^j \int \mathrm{d}^3 x^l \\
& \times \int \frac{\mathrm{d}^3 k_1^i}{(2\pi)^3} \int \frac{\mathrm{d}^3 k_2^i}{(2\pi)^3} \int \frac{\mathrm{d}^3 k_3^i}{(2\pi)^3} \int \frac{\mathrm{d}^3 k_4^i}{(2\pi)^3} \int \frac{\mathrm{d}^3 k_5^i}{(2\pi)^3} \int \frac{\mathrm{d}^3 k_6^i}{(2\pi)^3} \\
& \times e^{i x^i (k_{1,i} + k_{2,i})} e^{-i k_5^i x_i} e^{i x^j (k_{3,j} + k_{4,j})} e^{i k_5^j x_j} e^{i x^l (k_{1,l} + k_{4,l})} e^{i k_6^l x_l} \\
& \times \delta(k_1^i) \delta(k_2^i) \delta(k_3^i) \delta(k_4^i) \\
= & \frac{1}{\mathscr{N}} \int \frac{\mathrm{d}^3 k_6^i}{(2\pi)^3} \int \mathrm{d}^3 x^l e^{\mathrm{i} k_6^l x^l} \int \frac{\mathrm{d}^3 k_5^i}{(2\pi)^3} \int \mathrm{d}^3 x^i e^{-\mathrm{i} k_5^i x_i} f_1(x^i + x^l) f_2(x^i) \\
& \times \int \mathrm{d}^3 x^j e^{\mathrm{i} k_5^j x_j} f_3(x^j) f_4(x^j + x^l) \\
= & \frac{1}{\mathscr{N}} \int \frac{\mathrm{d}^3 k_6^i}{(2\pi)^3} \int \mathrm{d}^3 x^l e^{\mathrm{i} k_6^l x^l} \int \frac{\mathrm{d}^3 k_5^i}{(2\pi)^3} f_{12}(k_5^i, x^l) f_{34}(k_5^i, x^l) \\
= & \frac{1}{\mathscr{N}} \int \frac{\mathrm{d}^3 k_6^i}{(2\pi)^3} \int \mathrm{d}^3 x^l e^{\mathrm{i} k_6^l x^l} f_{1234}(x^l) \\
= & \frac{1}{\mathscr{N}} \int \frac{\mathrm{d}^3 k_6^i}{(2\pi)^3} f_{1234}(k_6^i) \\
= & \frac{1}{\mathscr{N}} f_{1234}(k_6) \; .
\end{aligned}
\tag{D.2}
$$

The formalism that allows to fix both diagonals is numerically more demanding than the algorithms marginalizing over one or both diagonals. Fixing both diagonals requires Fourier transforms of $f_1(x^i + x^l) f_2(x^i)$ and $f_3(x^j) f_4(x^j + x^l)$ for all x^l in the third line. This is similar to the method suggested in Eq. (13) of [79], which begins with a different set of Dirac functions but accomplishes a similar effect.

Bibliography

[1] R. Laureijs et al. Euclid Definition Study Report. *arXiv e-prints*, page arXiv:1110.3193, October 2011.

[2] Olivier Doré et al. Cosmology with the SPHEREX All-Sky Spectral Survey. 12 2014.

[3] Željko Ivezić et al. LSST: From Science Drivers to Reference Design and Anticipated Data Products. *The Astrophysical Journal*, 873(2):111, March 2019.

[4] Roy Maartens, Filipe B. Abdalla, Matt Jarvis, and Mario G. Santos. Overview of Cosmology with the SKA. *PoS*, AASKA14:016, 2015.

[5] M. H. Goroff, Benjamin Grinstein, S. J. Rey, and Mark B. Wise. Coupling of Modes of Cosmological Mass Density Fluctuations. *Astrophys. J.*, 311:6–14, 1986.

[6] Bhuvnesh Jain and Edmund Bertschinger. Second-order power spectrum and nonlinear evolution at high redshift. *The Astrophysical Journal*, 431:495, Aug 1994.

[7] F. Bernardeau, S. Colombi, E. Gaztanaga, and R. Scoccimarro. Large scale structure of the universe and cosmological perturbation theory. *Phys. Rept.*, 367:1–248, 2002.

[8] Daniel Baumann, Alberto Nicolis, Leonardo Senatore, and Matias Zaldarriaga. Cosmological Non-Linearities as an Effective Fluid. *JCAP*, 07:051, 2012.

[9] John Joseph M. Carrasco, Mark P. Hertzberg, and Leonardo Senatore. The Effective Field Theory of Cosmological Large Scale Structures. *JHEP*, 09:082, 2012.

[10] John Joseph M. Carrasco, Simon Foreman, Daniel Green, and Leonardo Senatore. The Effective Field Theory of Large Scale Structures at Two Loops. *JCAP*, 07:057, 2014.

[11] Enrico Pajer and Matias Zaldarriaga. On the Renormalization of the Effective Field Theory of Large Scale Structures. *JCAP*, 08:037, 2013.

[12] Tobias Baldauf, Lorenzo Mercolli, and Matias Zaldarriaga. Effective field theory of large scale structure at two loops: The apparent scale dependence of the speed of sound. *Phys. Rev. D*, 92(12):123007, 2015.

[13] Raul E. Angulo, Simon Foreman, Marcel Schmittfull, and Leonardo Senatore. The One-Loop Matter Bispectrum in the Effective Field Theory of Large Scale Structures. *JCAP*, 10:039, 2015.

[14] Tobias Baldauf, Lorenzo Mercolli, Mehrdad Mirbabayi, and Enrico Pajer. The Bispectrum in the Effective Field Theory of Large Scale Structure. *JCAP*, 05:007, 2015.

[15] Daniele Bertolini, Katelin Schutz, Mikhail P. Solon, Jonathan R. Walsh, and Kathryn M. Zurek. Non-Gaussian Covariance of the Matter Power Spectrum in the Effective Field Theory of Large Scale Structure. *Phys. Rev. D*, 93(12):123505, 2016.

[16] Daniele Bertolini, Katelin Schutz, Mikhail P. Solon, and Kathryn M. Zurek. The Trispectrum in the Effective Field Theory of Large Scale Structure. *JCAP*, 06:052, 2016.

[17] Andrei Lazanu, Tommaso Giannantonio, Marcel Schmittfull, and E.P.S. Shellard. Matter bispectrum of large-scale structure: Three-dimensional comparison between theoretical models and numerical simulations. *Phys. Rev. D*, 93(8):083517, 2016.

[18] Andrei Lazanu and Michele Liguori. The two and three-loop matter bispectrum in perturbation theories. *JCAP*, 04:055, 2018.

[19] Ryuichi Takahashi. Third Order Density Perturbation and One-loop Power Spectrum in a Dark Energy Dominated Universe. *Prog. Theor. Phys.*, 120:549–559, 2008.

[20] Atsushi Taruya, Takahiro Nishimichi, and Donghui Jeong. Grid-based calculation for perturbation theory of large-scale structure. *Phys. Rev. D*, 98(10):103532, 2018.

[21] Vincent Desjacques, Donghui Jeong, and Fabian Schmidt. Large-Scale Galaxy Bias. *Phys. Rept.*, 733:1–193, 2018.

[22] Takahiro Nishimichi, Guido D'Amico, Mikhail M. Ivanov, Leonardo Senatore, Marko Simonović, Masahiro Takada, Matias Zaldarriaga, and Pierre Zhang. Blinded challenge for precision cosmology with large-scale structure: results from effective field theory for the redshift-space galaxy power spectrum. 3 2020.

[23] Mikhail M. Ivanov, Marko Simonović, and Matias Zaldarriaga. Cosmological Parameters from the BOSS Galaxy Power Spectrum. *JCAP*, 05:042, 2020.

[24] Guido D'Amico, Jérôme Gleyzes, Nickolas Kokron, Katarina Markovic, Leonardo Senatore, Pierre Zhang, Florian Beutler, and Héctor Gil-Marín. The Cosmological Analysis of the SDSS/BOSS data from the Effective Field Theory of Large-Scale Structure. *JCAP*, 05:005, 2020.

[25] M. Crocce, S. Pueblas, and R. Scoccimarro. Transients from Initial Conditions in Cosmological Simulations. *Mon. Not. Roy. Astron. Soc.*, 373:369–381, 2006.

[26] Volker Springel. The Cosmological simulation code GADGET-2. *Mon. Not. Roy. Astron. Soc.*, 364:1105–1134, 2005.

[27] Theodore Steele and Tobias Baldauf. Precise calibration of the one-loop bispectrum in the effective field theory of large scale structure. *Phys. Rev. D*, 103:023520, Jan 2021.

[28] Theodore Steele and Tobias Baldauf. Precise calibration of the one-loop trispectrum in the effective field theory of large scale structure. *Phys. Rev. D*, 103:103518, May 2021.

[29] Albert Einstein. On the electrodynamics of moving bodies. *Annalen Phys.*, 17:891–921, 1905.

[30] Albert Einstein. The Field Equations of Gravitation. *Sitzungsber. Preuss. Akad. Wiss. Berlin (Math. Phys.)*, 1915:844–847, 1915.

[31] Albert Einstein. Cosmological Considerations in the General Theory of Relativity. *Sitzungsber. Preuss. Akad. Wiss. Berlin (Math. Phys.)*, 1917:142–152, 1917.

[32] Edwin P Hubble. Extragalactic nebulae. *The Astrophysical Journal*, 64, 1926.

[33] Georges Lemaître. Un univers homogène de masse constante et de rayon croissant rendant compte de la vitesse radiale des nébuleuses extra-galactiques. In *Annales de la Société scientifique de Bruxelles*, volume 47, pages 49–59, 1927.

[34] A. Friedman. On the Curvature of space. *Z. Phys.*, 10:377–386, 1922.

[35] Alan H. Guth. Inflationary universe: A possible solution to the horizon and flatness problems. *Physical Review D*, 23(2):347–356, January 1981.

[36] A.D. Linde. A new inflationary universe scenario: A possible solution of the horizon, flatness, homogeneity, isotropy and primordial monopole problems. *Physics Letters B*, 108(6):389–393, 1982.

[37] Andreas Albrecht, Paul J. Steinhardt, Michael S. Turner, and Frank Wilczek. Reheating an inflationary universe. *Phys. Rev. Lett.*, 48(20):1437–1440, May 1982.

[38] Alexander Vilenkin. Quantum Fluctuations in the New Inflationary Universe. *Nucl. Phys. B*, 226:527–546, 1983.

[39] E. Komatsu, K. M. Smith, J. Dunkley, C. L. Bennett, B. Gold, G. Hinshaw, N. Jarosik, D. Larson, M. R. Nolta, and L. et al. Page. Seven-year wilkinson microwave anisotropy probe (wmap) observations: Cosmological interpretation. *The Astrophysical Journal Supplement Series*, 192(2):18, Jan 2011.

[40] N. Aghanim, Y. Akrami, M. Ashdown, J. Aumont, C. Baccigalupi, M. Ballardini, A. J. Banday, R. B. Barreiro, and N. et al. Bartolo. Planck 2018 results. *Astronomy and Astrophysics*, 641, Sep 2020.

[41] N. Aghanim et al. Planck 2018 results. VI. Cosmological parameters. *Astron. Astrophys.*, 641:A6, 2020. [Erratum: Astron.Astrophys. 652, C4 (2021)].

[42] Lorenzo Mercolli and Enrico Pajer. On the velocity in the Effective Field Theory of Large Scale Structures. *JCAP*, 03:006, 2014.

[43] D. J. Heath. The growth of density perturbations in zero pressure Friedmann-Lemaître universes. *MNRAS*, 179:351–358, May 1977.

[44] Sean M. Carroll, William H. Press, and Edwin L. Turner. The cosmological constant. *Annual Review of Astronomy and Astrophysics*, 30(1):499–542, 1992.

[45] P. J. E. Peebles. *The Large-Scale Structure of the Universe*. Princeton University Press, 1980.

[46] J. N. Fry. The Galaxy correlation hierarchy in perturbation theory. *Astrophysical Journal*, 279:499–510, April 1984.

[47] Alexander Eggemeier, Roman Scoccimarro, and Robert E. Smith. Bias Loop Corrections to the Galaxy Bispectrum. *Phys. Rev. D*, 99(12):123514, 2019.

[48] Valentin Assassi, Daniel Baumann, Daniel Green, and Matias Zaldarriaga. Renormalized Halo Bias. *JCAP*, 08:056, 2014.

[49] Andrea Pezzotta, Martin Crocce, Alexander Eggemeier, Ariel G. Sánchez, and Román Scoccimarro. Testing one-loop galaxy bias: cosmological constraints from the power spectrum. 2 2021.

[50] A. F. Heavens, S. Matarrese, and Licia Verde. The Nonlinear redshift-space power spectrum of galaxies. *Mon. Not. Roy. Astron. Soc.*, 301:797–808, 1998.

[51] Leonardo Senatore and Matias Zaldarriaga. Redshift Space Distortions in the Effective Field Theory of Large Scale Structures. 9 2014.

[52] Vincent Desjacques, Donghui Jeong, and Fabian Schmidt. The Galaxy Power Spectrum and Bispectrum in Redshift Space. *JCAP*, 12:035, 2018.

[53] Tobias Baldauf, Mehrdad Mirbabayi, Marko Simonović, and Matias Zaldarriaga. LSS constraints with controlled theoretical uncertainties. 2 2016.

[54] Roger W Hockney and James W Eastwood. *Computer simulation using particles*. crc Press, 2021.

[55] Eric Tittley and HMP Couchman. The effect of substructure on the final state of matter in an x-ray cluster. In *Computational Astrophysics; 12th Kingston Meeting on Theoretical Astrophysics*, volume 123, page 369, 1997.

[56] Toshiyuki Fukushige and Junichiro Makino. On the origin of cusps in dark matter halos. *The Astrophysical Journal*, 477(1):L9–L12, March 1997.

[57] John K. Salmon and Michael S. Warren. Fast parallel tree codes for gravitational and fluid dynamical n-body problems. *The International Journal of Supercomputer Applications and High Performance Computing*, 8(2):129–142, 1994.

[58] A. Doroshkevich, E. Kotok, A. Poliudov, Sergei Shandarin, Iu Sigov, and I. Novikov. Two-dimensional simulation of the gravitational system dynamics and formation of the large-scale structure of the universe. *Monthly Notices of the Royal Astronomical Society*, 192:321–337, 07 1980.

[59] Charles K. Birdsall and Dieter Fuss. Clouds-in-clouds, clouds-in-cells physics for many-body plasma simulation. *Journal of Computational Physics*, 3(4):494–511, January 1969.

[60] George Efstathiou, Marc Davis, SDM White, and CS Frenk. Numerical techniques for large cosmological n-body simulations. *The Astrophysical Journal Supplement Series*, 57:241–260, 1985.

[61] J. S. Bagla. Treepm: A code for cosmological n-body simulations. *Journal of Astrophysics and Astronomy*, 23(3-4):185–196, Dec 2002.

[62] Roman Scoccimarro, Stephane Colombi, James N. Fry, Joshua A. Frieman, Eric Hivon, and Adrian Melott. Nonlinear evolution of the bispectrum of cosmological perturbations. *Astrophys. J.*, 496:586, 1998.

[63] Emiliano Sefusatti and Román Scoccimarro. Galaxy bias and halo-occupation numbers from large-scale clustering. *Phys. Rev. D*, 71:063001, Mar 2005.

[64] Nina Roth and Cristiano Porciani. Testing standard perturbation theory and the Eulerian local biasing scheme against N-body simulations. *MNRAS*, 415(1):829–844, July 2011.

[65] Atsushi Taruya, Takahiro Nishimichi, and Donghui Jeong. The covariance of the matter power spectrum including the survey window function effect: N-body simulations vs. fifth-order perturbation theory on grid. 7 2020.

[66] John Joseph M. Carrasco, Simon Foreman, Daniel Green, and Leonardo Senatore. The 2-loop matter power spectrum and the IR-safe integrand. *JCAP*, 07:056, 2014.

[67] Matthew Lewandowski and Leonardo Senatore. IR-safe and UV-safe integrands in the EFTofLSS with exact time dependence. *JCAP*, 08:037, 2017.

[68] Muntazir Mehdi Abidi and Tobias Baldauf. Cubic Halo Bias in Eulerian and Lagrangian Space. *JCAP*, 07:029, 2018.

[69] Aurel Schneider, Romain Teyssier, Doug Potter, Joachim Stadel, Julian Onions, Darren S. Reed, Robert E. Smith, Volker Springel, Frazer R. Pearce, and Roman Scoccimarro. Matter power spectrum and the challenge of percent accuracy. *JCAP*, 04:047, 2016.

[70] T. Hahn. CUBA: A Library for multidimensional numerical integration. *Comput. Phys. Commun.*, 168:78–95, 2005.

[71] Matthew Lewandowski, Ashley Perko, and Leonardo Senatore. Analytic Prediction of Baryonic Effects from the EFT of Large Scale Structures. *JCAP*, 05:019, 2015.

[72] Tobias Baldauf, Emmanuel Schaan, and Matias Zaldarriaga. On the reach of perturbative descriptions for dark matter displacement fields. *JCAP*, 03:017, 2016.

[73] Marcel Schmittfull, Marko Simonović, Valentin Assassi, and Matias Zaldarriaga. Modeling Biased Tracers at the Field Level. *Phys. Rev. D*, 100(4):043514, 2019.

[74] Davide Gualdi, Sergi Novell, Héctor Gil-Marín, and Licia Verde. Matter trispectrum: theoretical modelling and comparison to N-body simulations. *JCAP*, 01:015, 2021.

[75] Diego Blas, Stefan Floerchinger, Mathias Garny, Nikolaos Tetradis, and Urs Achim Wiedemann. Large scale structure from viscous dark matter. *JCAP*, 11:049, 2015.

[76] Diego Blas, Mathias Garny, Mikhail M. Ivanov, and Sergey Sibiryakov. Time-Sliced Perturbation Theory for Large Scale Structure I: General Formalism. *JCAP*, 07:052, 2016.

[77] Marcos Lima and Wayne Hu. Self-calibration of cluster dark energy studies: Counts in cells. *Phys. Rev. D*, 70:043504, Aug 2004.

[78] Joachim Harnois-Déraps, Nicolas Martinet, Tiago Castro, Klaus Dolag, Benjamin Giblin, Catherine Heymans, Hendrik Hildebrandt, and Qianli Xia. Cosmic Shear Cosmology Beyond 2-Point Statistics: A Combined Peak Count and Correlation Function Analysis of DES-Y1. 12 2020.

[79] Joseph Tomlinson, Donghui Jeong, and Juhan Kim. Efficient parallel algorithm for estimating higher-order polyspectra. *Astron. J.*, 158(3):116, 2019.